Fine Particle Transport and Separation Using Electrostatic Travelling Wave Methods

Yue Yu
Resource Geophysics Academy
Department of Earth Science and Engineering
Imperial College London

Supervisor: Prof. Kathryn Hadler
Prof. Jan Cilliers
Prof. Yanghua Wang
Advisor: Stanley Starr

Submitted in partial fulfilment of the requirements
for the degree of Doctor of Philosophy in Engineering and
the Diploma of Imperial College London

London, Feb. 2024

Abstract

An electrostatic travelling wave (ETW) field can be produced by a set of electrodes, insulated from each other and connected to AC poly-phase voltage sources. ETW techniques have been previously applied to transport particles, but the separation of particles by size has not been considered, and this is the focus of this thesis. The use of ETW to separate particles by size requires understanding of the forces acting on particles. This is done using models for the electrostatic field, single particle motion and for multiple particles.

The accuracy of the calculation of the electric field distribution was improved by using advanced numerical methods and included in a more rigorous particle motion simulation model. The simulations explore how different parameter combinations affect the transition of particle motion modes, the particle moving velocity and levitation height.

The experimental research verified the simulation model and clarified basic mechanisms. The recording of particle trajectory clearly identified the three typical motion modes. The analysis comparing dielectrophoresis (DEP) and Coulomb force explains the reason for the backward motion of poorly charged particles.

In the multiple particle experiments, the fraction of particles transported in forward and backward directions exhibited frequency-dependence. At lower frequencies, most particles moved forward, but as the frequency increased, the fraction of particles being transported backward increased. A crossover frequency was identified and defined, at which a particle is equally likely to move forward or backward. This critical frequency decreases as the particle size increases. The crossover frequency can be used to select the appropriate frequencies to separate particles by size by making the fine particles mostly move forward and coarse particles mostly move backward. A mixture of 30 to 50 μm and 75 to 110 μm particles was tested and the results showed good separation performance.

Acknowledgement

During my doctoral studies, I embarked on a truly meaningful journey of exploration in my life, embracing unknown challenges with no knowledge of the journey's end. I am delighted to have reached the milestone of completing a doctoral dissertation. I am grateful for every moment of this period, for the people around me who provided me with help and support.

I would like to express my sincerest gratitude to my supervisors: Prof. Jan Cilliers, Prof. Kathryn Hadler, Stan, and Prof. Yanghua Wang.

I am very grateful to Prof. Yanghua for accepting me as his student, providing funding support from Sinopec, introducing me to Prof. Jan's group, and for his care, guidance, and advice throughout my doctoral studies.

I want to thank Prof. Jan the most. He always prioritizes his students, never missing a discussion with them, and he is the most generous and insightful supervisor. I appreciate his constant attention to my progress, every suggestion he provided for my experiments and simulations, his edits and comments for every manuscript I wanted to publish, and the multiple revisions he made to my doctoral dissertation.

I am extremely grateful to Prof. Kathryn. She is very kind and considerate towards her students. I always remember her as the organizer of Space Resources Week, who, despite her busy schedule, took the time to encourage me and help alleviate the pressure of my presentation. Her meticulous attention to detail and overall grasp of my experimental research and the structure of my papers and thesis have been enlightening for me.

I am very grateful to Stan. He always provides timely feedback and communicates with me patiently, offering problem-solving insights during our discussions. I learned from him a rigorous scientific attitude, as well as curiosity and a thirst for knowledge. His sharing of life experiences and attitudes have also been very helpful.

I want to express my gratitude to my supervisors again. They always demonstrate such excellence that I feel rejuvenated after every meeting with them, filled with hope and motivation throughout my research journey, which ultimately enabled me to successfully complete my thesis.

I also want to thank Prof. Eric deeply, who as my examiner for the Early Stage Assessment and Late Stage Review, provided invaluable advice and assistance with software and experimental equipment and has been consistently supportive.

I would like to express my gratitude to Prof. Yao. He led me onto the path of scientific research during my undergraduate studies. He has always been there to help me understand various scientific concepts by answering my questions and providing invaluable assistance with electric field calculations. Thanks to my master's supervisor, Prof. Xinxin Wang. I have learned from him the purest pursuit of science.

I would like to thank my friends and colleagues, Dr. Joshua, Dr. Cruise, Arjun, Luka, Kosuke, etc., in the group of Mineral Processing, Dr. Jiashun, Cao Chai, Haosen Zhang, Xinyu Dong, Ke Lu, Shengjuan Cai, Xiaowei Yang, etc., in the Resource Geophysics Academy, and Dr. Jianglin in Sinopec. Thanks Dr. David at Hackspace for his extensive assistance with the board design.

Last but not least, the person I am most grateful to is my mother in my life, Honghua He. It is her selfless love, encouragement, and guidance that have helped me grow and reach where I am today. I also love her very much. I appreciate the ongoing support and life advice of my father, Xuezheng Yu, and the enduring patience of my girlfriend, Min Zhou.

Copyright

Declaration of Originality

I hereby declare that all of the work presented in this thesis – except that which is appropriately acknowledged and referenced as such – is my own, and that it has not been submitted in fulfilment of the requirements of any other degree at Imperial College London or elsewhere.

Yue Yu

Feb. 2024

Contents

Chapter 5 Single-particle Experiments 99

List of Tables

List of Figures

List of Abbreviations

BEM	Boundary element method
BVP	Boundary value problem
CICR	Cleaning Index Change Rate
CNT	Carbon Nanotube
CSM	Charge simulation method
DBDs	Dielectric barrier discharges
DEM	Discrete element method
DEP	Dielectrophoresis
DRE	Dust removal efficiency
EDS	Electrodynamic screen
ETDP	Exploration Technology and Development Program
ETW	Electrostatic travelling wave
FEM	Finite Element Method
FR4	Flame Retardant 4
HASL	Hot air solder levelling
ISRU	In-Situ Resource Utilization
MOXIE	Mars Oxygen ISRU experiment
PCB	printed circuit board
PMMA	Poly (Methyl Methacrylate)
PTFE	Polytetrafluoroethylene
PVC	Polyvinyl Chloride
Q/M	Charge to mass ratio
RMS	Root-mean-square
SPIcDER	Space suit Integrated Carbon nanotube Dust Ejection/Removal
twDEP	Travelling wave dielectrophoresis
WFM	Work function matching

Nomenclature

The main nomenclatures are listed as follows. In the thesis, different chapters may have varying definitions for a few nomenclatures. Please refer to the respective chapter for the correct definition.

A_h	Hamaker constant, J	K_1	Clausius-Mossotti factor
a_n	Fourier coefficient	K_n	Generalized polarization coefficients
c_i and l_i	Coefficients of polynomial function	l	Electrode length, mm
D	Width of electrode, mm	m	Mass, kg
$\boldsymbol{E}$	Electric field, V/m	$\boldsymbol{n}$	Vertical normal vector
E_c	Dielectric strength of air, V/m	$\boldsymbol{n}_T$	Horizontal norm vector
E_d	Normal electric field, V/m	p	Pitch of parallel electrodes, mm
E_rms	Amplitude of electric field, V/m	q	Percent of saturation charge
f	Frequency, Hz	q	Total charge of particle, C
$\boldsymbol{F}_\mathrm{C}$	Coulomb force, N	q_m	Saturation charge, C
$\boldsymbol{F}_\mathrm{DEP}$	Dielectrophoretic force, N	R_b	Forward recovery rate
$\boldsymbol{F}_\mathrm{Drag}$	Air drag force, N	R_f	Forward recovery rate
$\boldsymbol{F}_\mathrm{I}$	Image force, N	T	Period, s
$\boldsymbol{F}_\mathrm{f}$	Friction force, N	U_p	Positive potential , V
$\boldsymbol{F}_\mathrm{G}$	Gravitational force, N	U_n	Negative potential, V
$F_{total,y}$	Net force in vertical direction, N	V_A	Amplitude of applied voltage, V
$\boldsymbol{F}_\mathrm{vdW}$	van der Waals force, N	$\boldsymbol{v}_\mathrm{p}$	Velocity, m/s
g	Gravitational constant, 9.8 m/s^2	v_{x0}, v_{y0}	Initial velocity, m/s
H_0	Minimum separation, m	x_0, y_0	Initial position, m
$\boldsymbol{i}$	Imaginary unit	X_0	Initial position in x direction, m
j	Order of polynomial function	Y_0	Levitation height, m
k	$2\pi/\lambda$	y_p	Height of particle, m

Greek letter

α_n	Fourier term, 2nπ/λ
δ_{yr}	Kronecker delta
ε_0	Vacuum permittivity, F/m
ε_m	Dielectric permittivity of the medium, F/m
ε_m^*	Complex dielectric permittivity (medium)
ε_p	Relative dielectric permittivity (particle)
ε_p^*	Complex dielectric permittivity (Particle)
η	Viscosity of air, kg/(m·s)
λ	Wavelength, m
λ_d	Average distance between asperities, m
μ	Friction coefficient
ρ	Density of particle, kg/m^3
σ	Conductivity, S/m
φ_1, φ_2	Phase differences
ϕ	Potential of electric field, V
ω	Angular frequency, s^{-1}

Chapter 1 Introduction

1.1 Research Context

The controlled movement of dry particles using non-mechanical means is desirable in a number of different applications, including mineral processing, the handling and beneficiation of regolith (extra-terrestrial soils) for In-Situ Resource Utilization (ISRU), dust mitigation of solar panels and in other space devices.

ISRU is the harnessing of local natural resources in space. Instead of taking all needed supplies from Earth, the production of oxygen, hydrogen and metal on the Moon or Mars enables longer duration and lower cost space missions [1-3]. ISRU has gained increasing focus in recent years, such as in the Exploration Technology and Development Program (ETDP) led by NASA in 2005 [4] through to the more recent Mars Oxygen ISRU Experiment (MOXIE) [5]. Analogous to terrestrial mining process, mineral processing, also known as beneficiation of the fine dusty mineral particles that cover the Moon and Mars, is a key part in the flowsheet of ISRU. Beneficiation results in regolith feedstock that is enriched in the appropriate material for the subsequent process steps. Fluid-free mineral processing or particle manipulation is necessary in the beneficiation process of ISRU because fluid-based processes are impractical in the hard vacuum of the Moon or the very low pressure on Mars [3]. As a result, electric and magnetic methods have been investigated and researched for ISRU beneficiation [6-9].

Deposition of dust on the surface of solar panels disrupts the absorption of solar energy and significantly reduces the efficiency of energy output, also known as soiling loss [10, 11]. Low-maintenance operation of solar devices requires protection of dust loading in arid regions, energy grids near highways, and space environments [12-14]. On the Moon, the accumulation of dust in mechanical devices can impair their function. Dust adhering to spacesuit ends up in the habitat, resulting in astronaut exposure, leading to undesirable effects on the skin, eyes and airways [15-17]. Dust mitigation techniques are needed to tackle these issues in space exploration.

An electrostatic travelling wave (ETW) field can be produced by a set of electrodes, insulated from each other and connected to AC poly-phase voltage sources. Neutral or charged fine particles brought into the ETW field will move with a trajectory determined by the electrical forces, gravitational and drag forces, and other forces dependent on their physical properties. The ETW, in large part, depends on dielectrophoresis (DEP), first defined by Pohl as the interaction between non-uniform electric fields with polarized particles and liquids [18, 19]. Due to the advantages of a simple structure, fluid-free and low energy operation, ETW methods have grown in popularity for applications in dry mineral processing, space technology and dust mitigation.

1.2 Objectives

The earliest concept of ETW, the method of 'electric curtain' was first applied by Masuda and coworkers in the connection with charged aerosol clouds transportation [20-22]. They also conducted experiments and developed simulation models on the movement of blood cell and separation of particles in liquids [23, 24]. In their theory, the wave field was simplified to the combination of two harmonic waves propagating in different directions. If particles with different properties carried by different waves and move in different directions, the transport and separation of particles could be achieved simultaneously.

Subsequently, more efforts were made to understand the experiment phenomenon quantitatively and to design improved devices [25-27]. Machowski and coworkers [28] performed the separation experiments on sand and pulverised alumina powders by testing different shapes of electrodes, such as cylinder and stripe. They found sand was transported along the travelling wave while alumina was transported oppositely at lower frequencies. And at higher frequencies, both the motion directions of sand and alumina reversed due to the transition of motion mode.

Recent advances have been made in developing theories of particle motion for ETW methods [29-31]. Kawamoto and coworkers [9] adopted a 3-D modified hard-sphere DEM model to predict the particle motion in the lunar environment. By adjusting the balance of the gravitation force and Coulomb force on different sizes of particles, the particles smaller than 20 μm flew higher above the conveyor board and could be separated in a vacuum chamber. Zouaghi and coworkers [32-35] have also made systematic investigations on the particle motion mechanisms, especially on the explanation of backward motion. They have revealed the important effect of particle size and operating frequency.

The research on the design of dust mitigation and the toner transport technologies using ETW methods have advanced much more than that of particle separation [13, 36-41]. This is because dust mitigation or toner transport does not require the strict control of particle trajectories as does particle separation. Particle separation systems design must precisely consider the relevant properties of the particles to be separated. Currently, particle separation systems are poorly understood because the underlying theory of particle motion is poorly understood.

Particle motion in an electrostatic field is affected by a complex combination of factors. However, most conclusions in the literature are qualitative and the basic relationships between particle transport characteristics, conveyor parameters and applied voltage remain unclear. This makes experimentally observed phenomena difficult to explain and presents challenges in optimising equipment design. Simulation research methods allow a deeper understanding of the mechanism of particle transport in an ETW field. A more comprehensive investigation using simulation based on the combination of different parameters is needed. In addition, experimental verification needs to be carried out both to validate simulations but also allow the reliable specification of system parameters.

The objective of this research is to develop and demonstrate an ETW system that can successfully transport, or transport with separation, fine particles.

This was achieved through the following steps:

1. Review the prior research of ETW methods on particle transport and separation to identify the gaps and development needs for such applications.

2. Calculate the accurate distribution of electric fields and analysis of the DEP.

3. Explore the particle motion mechanisms in ETW fields by performing simulations: the effect of operating and system parameters on particle motion modes, moving direction, speed and levitation height.

4. Build an ETW system and develop test procedures for experiments and analyses.

5. Verify the simulation model and conclusions from simulations through single particle transport experiments.

6. Perform multi-particle transport and separation experiments using the conclusions from simulation model as a guide.

This thesis describes these steps and results in detail and concludes with the current state of the art and comments on potential future work.

1.3 Thesis Structure

This thesis comprises seven chapters, including this introduction, five main chapters and the conclusions chapter. Five main chapters are adapted from four peer-reviewed published journal articles. The structure of the thesis and the content of each chapter are organized according to the following logic shown in Fig. 1.1. These arrows in the schematic show how the contents of these chapters flow.

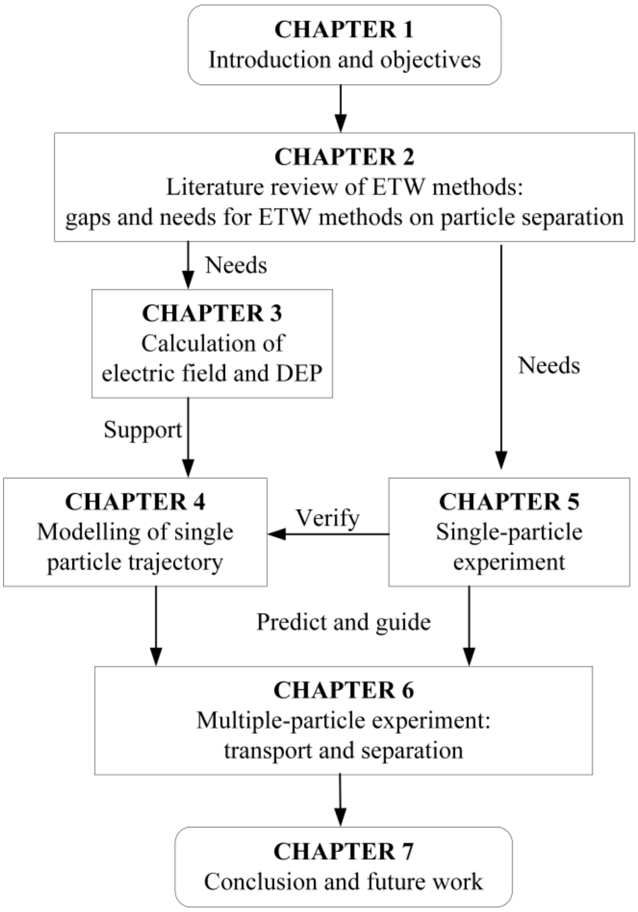

Fig. 1.1 Schematic structure of the thesis.

Chapter 1 briefly introduces the potential application areas of ETW methods, presents the main objectives of this research, and outlines the thesis structure.

Chapter 2 provides a comprehensive literature review of ETW methods. The review covers the different development stages of ETW methods, exploring particle movement mechanisms, hardware diversity, and applications in dust mitigation, ISRU processes and other areas. It includes experimental evaluations, discusses theoretical simulations, and provides insights for improving ETW device effectiveness by addressing existing limitations. This chapter is based on the published paper: Yu, Y., Cilliers, J., Hadler, K., Starr, S. and Wang, Y., 2022. A review of particle transport and separation by electrostatic travelling wave methods. Journal of Electrostatics, 119, 103735.

Chapter 3 presents the numerical results of the distribution of electric field of an ETW system using charge simulation method (CSM) and boundary element method (BEM). The optimised CSM and BEM show higher accuracy and calculation efficiency. Analyses are provided of the electric field and DEP components. This chapter is based on the published paper: Yu, Y., Luo, Y., Cilliers, J., Hadler, K., Starr, S. and Wang, Y., 2023. Numerical solution of the electric field and dielectrophoresis force of electrostatic travelling wave system. Micromachines, 14, (7), 1347.

Chapter 4 develops a single particle simulation model with the aim of exploiting differences in motion and velocity to separate particles by size. It includes simulation results of particle trajectories showing the effects of frequency, wavelength, particle size and charge, and initial conditions on the properties of particle motion, such as moving velocity, levitation height and motion modes. These results are compared and verified by experimental observations using a high-speed camera. This chapter is based on the published paper: Yu, Y., Cilliers, J., Hadler, K., Starr, S. and Wang, Y., 2023. The motion of small particles in electrostatic travelling waves for transport and separation. Powder Technology, 425, 118587.

Chapter 5 focuses on the single-particle experiments. It introduces the methodology of experiments including the selection of particle material, experimental procedure, data collection and analysis methods. The experimental results reveal the effects of frequency and DEP on the backward motion of particles, which also verify the simulation model and provide guidance for the design of the separation system. The limitations of the experiment are also outlined.

Chapter 6 addresses the multi-particle experiments. It verifies the transport ability of the system for large quantities of particles. The relationship between particle transport direction with particle size and frequency is explored and revealed. Finally, this research experimentally demonstrates that ETW can be used to separate particles by size. This chapter is based on the published paper: Yu, Y., Cilliers, J., Hadler, K., Starr, S. and Wang, Y., 2024. Dry particle size separation using electrostatic travelling wave methods. Separation and Purification Technology,126275.

Chapter 7 summarises the achievements in this thesis and makes recommendations for future work.

1.4 Conference Presentation

The main conferences I attended are listed as follows:

- Yu, Y., Cilliers, J., Hadler, K., Starr, S. and Wang, Y., Particle transport and separation using an electrostatic travelling wave. XXXI IMPC-International Mineral Processing Congress. Held Sept. 29 – Oct. 3. 2024, Washington, DC, USA. (Poster)
- Yu, Y., Cilliers, J., Hadler, K., Starr, S. and Wang, Y., Dielectrophoresis affects particle motion in electrostatic travelling waves: A potential application for lunar soil beneficiation. XXIII Space Resources Roundtable. Held 6 – 9 June. 2023. Colorado School of Mines in Golden, CO, USA. (Oral Presentation)
- Yu, Y., Cilliers, J., Hadler, K., Starr, S. and Wang, Y., The motion of small particles in electrostatic travelling waves for transport and separation. 2023 CRG Annual meeting. Held 2nd June, RGA, London, UK. (Oral Presentation)

- Yu, Y., Cilliers, J., Hadler, K., Starr, S. and Wang, Y., Theory for particle motion in electrostatic travelling wave fields. Space Resources Week 2023. Held 18 – 21 Apr. Luxembourg. (Oral Presentation)
- Yu, Y., Cilliers, J., Hadler, K., Starr, S. and Wang, Y., Modelling the motion of dust particles in electrostatic travelling wave fields. 9th World Congress on Particle technology. Held 18 – 22 Sep. Madrid, Spain. (Oral Presentation)
- Yu, Y., Luo, Y., Cilliers, J., Hadler, K., Starr, S. and Wang, Y., The electric field of a parallel electrode array calculated using the charge simulation and boundary element methods. 2022 CRG Annual meeting. Held 16th Aug., RGA, London, UK. (Oral Presentation)

Chapter 2 Literature Review

An ETW field can be produced by parallel electrodes and a suitable multiphase voltage source. Neutral or charged fine particles brought into such a field will move with different trajectories due to the action of the electric forces, gravitational force, and other forces related to their different physical properties. Some particles may be charged further by contact with the dielectric layer covering the electrodes (tribocharging). ETW systems with appropriately designed parameters, such as electrode configuration and voltage characteristics, can be used to transport and separate particles, which is desirable in a number of different applications, including solar panel dust mitigation, toner particle motion and in the handling and beneficiation of fine dusty particles, for example lunar dust. This literature review brings together the research carried out on these applications using ETW methods.

This review chapter is divided into four sections. The first section introduces the different terminologies used for ETW methods in different development stages and application areas. And it introduces the basic transport mechanisms for particles in an ETW field and the classification of particle motion modes. The literatures reviewed in this chapter are also classified into different categories according to the application areas and conditions. The second section details the development of ETW equipment designs in the areas of dust mitigation, particle transport and ISRU processes, along with their performance at laboratory and industrial scales. The third section focuses on theory and simulation research, including the comparison of electric field calculation methods and particle trajectory simulation methods. The review of particle simulation research are divided into two categories: single-particle simulations and multi-particle simulations. The methods and conclusions of two type of simulations are summarized and compared. Finally, this chapter provides a guide for possible improvement of the effectiveness of ETW devices, by outlining the limitations in application, theoretical understanding and potential research aspects. It also provides insights where the research begins on the design of system for particle transport and separation.

2.1 Introduction

2.1.1 Terminology

The earliest concept using electrostatic travelling forces to remove charged particles on a plate was put forward by NASA [42] in a report of various means of clearing dust from thermal radiator panels on the Moon. The test platform is shown in Fig. 2.1. The structure of the electric curtain is very similar to the mechanical brush design (Fig. 2.1 *a*), involving a worm gear drive system that pushes the brush frame forward and back. Specially for electrostatic design, a charged conducting rod isolated by an insulation layer is inserted, shown in (Fig. 2.1 b). According to the report ([42], section 3.5.6) time and funding limitations did not allow testing of the electric brush. Instead, basalt particles were charged and dropped onto the plate or the plate was charged. Both tests were conducted in the laboratory atmosphere. The removal of dust was not effective and only some of fine particles could fly away [42]. The report provides insufficient data and detail to analyse its lack of performance. More serious research using ETW methods on the electric curtain was later begun by Masuda and coworkers, such as the transport of aerosol particles and separation of biological cells [20, 23]. After that, a series of scientific investigations on understanding the mechanisms of particle motion and different designs of the electrode configurations have been performed, the content of which is expanded in section 2.2.1.

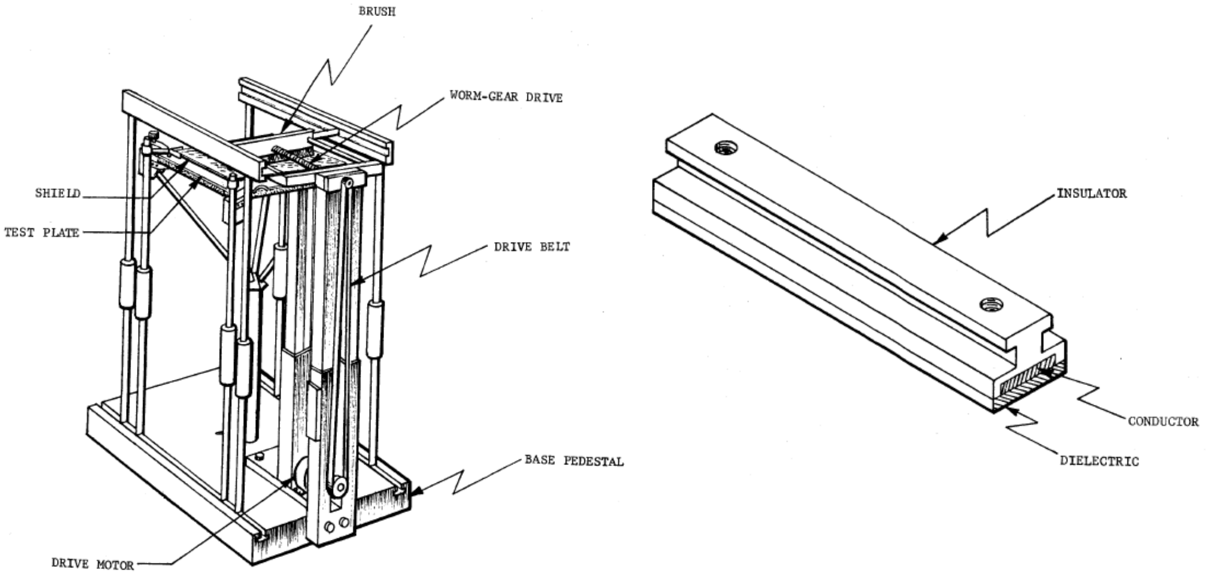

(*a*) Structure of mechanical brush design. (b) Electric insert of the brush frame with insulator.

Fig. 2.1 Final design of electrostatic concept of dust removal test platform — combination of (*a*) and (b) [42].

Compared with the type of single electrode structure proposed by NASA, the design of parallel cylindrical electrodes was first introduced by Masuda and coworkers, shown in Fig. 2.2 [22]. Single phase and multiple phase voltages were applied to electrodes, and charged particles entering into this field could move effectively under the action of the electric and other forces.

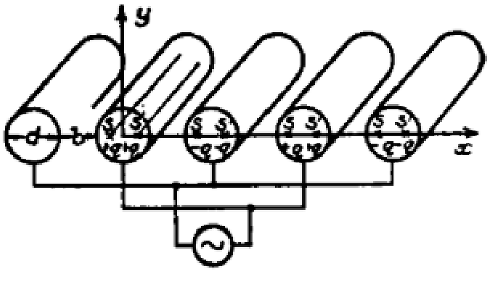

Fig. 2.2 Design of electric curtain composed of parallel cylinder electrodes applied with multiple phase voltages from Mauda, et al. [22].

Using the similar configuration of electrodes and voltage source, the technology named as electrodynamic screen (EDS) is used for dust mitigation on solar panels, as shown in Fig. 2.3 [12]. The material selected for this case is transparent. While ensuring cleaning efficiency, the spacing between the electrodes should be sufficient to allow the photosensitive components on the surface to receive more solar energy. The detailed development and research of EDS are introduced in section 2.2.2.

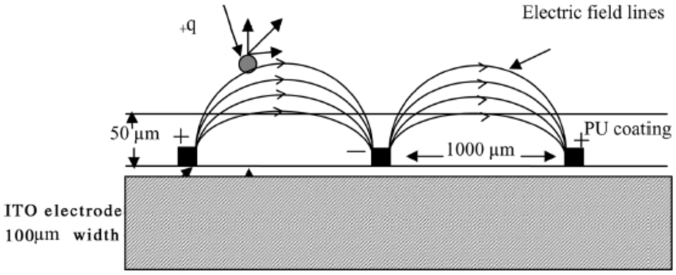

Fig. 2.3 Cross profile of an electrodynamic screen made of indium tin oxide electrodes embedded in a transparent polyurethane film [12].

The current ETW systems consist of a flat insulating surface with embedded linear electrodes. The voltage applied to these electrodes generates an electric field. If a single phase or two-phase time-varying voltage is applied to the electrodes, a standing wave is generated. When using multi-phase voltages, a travelling wave can be produced. Fig. 2.4 shows a schematic of the ETW hardware and the conceptual view of the electric field.

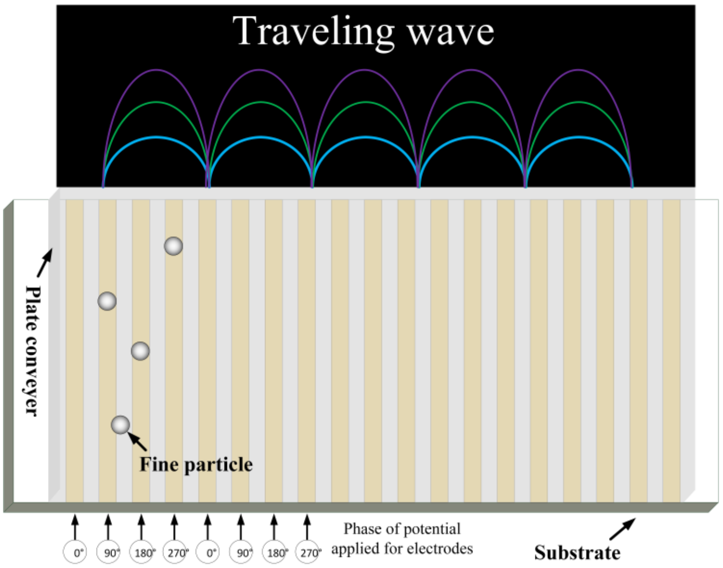

Fig. 2.4 Schematic of particle movement platform with an ETW field, a plan view of the electrodes and an elevation view of a conceptual electrostatic wave.

2.1.2 Particle Transport Mechanisms

When a neutral particle enters into a non-uniform electric field (e.g. circular electrodes), electric charges will be redistributed at the surface of the particle such that positive and negative charge will accumulate on opposite sides of the particle, producing dipole polarity. This results in a dielectrophoretic force and particle movement [43].

The triboelectric effect produces electrostatic charge exchanges on particles through rubbing, both between particles and between particles and the surface of the dielectric layer. The exchange of charge depends on the work functions and surface physical properties of the materials in contact. Particles will accumulate charges on them via tribocharging as they move along the surface of the dielectric layer covering the electrodes [44]. Particles with a net charge due to this effect are affected by Coulomb forces which are typically stronger than DEP.

The basic charge transfer between two dielectric materials and mechanism of tribocharging is poorly understood [45, 46], because the actual charge transfer behaviour depends on multiple factors, including the nature of contact, environmental conditions such as temperature and humidity, and any surface processing history [47, 48]. Basic concepts and theories of charge transfer, as well as experimental and simulation methods, can be found in review papers, such as [49, 50], and will not be discussed further here.

2.1.3 Particle Motion Modes

The classification of particle motion modes is an effective technique to analyse particle motion. Because of the symmetry of the electrode systems, particle motion is assumed to be two-dimensional. Particles moving in the same direction as the travelling wave are termed forward motion, while those moving against it are termed backward motion.

The motion mode of particle in ETW field depends on the experimental conditions. The moving trajectories of particles can be classified into different modes. By changing frequencies of applied voltage (varied from 10^{-1} to 10 Hz), Masuda observed five motion modes, shown in Fig. 2.5 [23]. At the lowest frequency, particles will drop onto the surface and bounce alternatively, shown as (a) in Fig. 2.5, called stepwise motion. As the frequency rises, the particle will not drop, but moves with a constant velocity, Fig. 2.5 (b), called forward motion with constant velocity, as the electric forces and resistance on the particle are in balance. If the frequency rises further, the particle move in a circular motion (c), and the direction may be forward or backward. Particle motion (d) has a smaller average velocity, because it has a higher circular frequency than (c). At the even higher frequency, the particle will spin (e) with a very small average horizontal velocity. This vibration mode was also observed in Kawamoto's experiments [51].

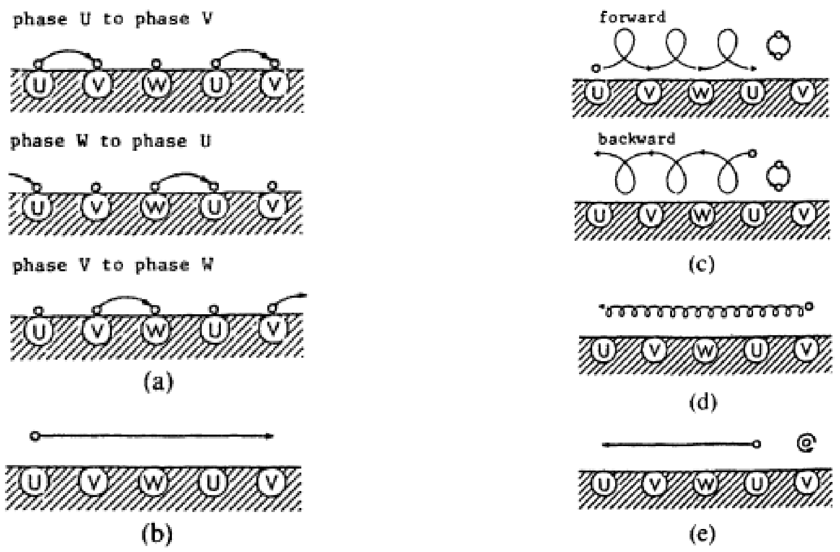

Fig. 2.5 Observed particle trajectories showing different motion modes under different frequencies of voltage [23].

Melcher at al. [52] used a dimensionless model to solve the particle average moving speed analytically and compared it with numerical results under single-phase perfect travelling sinusoidal wave. The particle motion was classified into two modes depending on the average velocity of the particle: synchronous mode and asynchronous mode. In synchronous mode, particles have similar average velocities to that of the travelling wave, while in asynchronous mode, particles have much smaller average velocities than the travelling wave. Melcher at al. [52] studied particle motion analytically, and simulated similar motion to Fig. 2.5 (a), which they termed hopping mode, a synchronous mode. Melcher at al. further proved that particles in cyclic motion (Fig. 2.5 (c) and (d)) could only have low velocities, called curtain mode, an asynchronous mode, and that it is likely when the frequency is greater than the key frequency $f = \sqrt{gk}/\pi$, where g is the gravitational constant and $k = 2\pi/wavelength$. Wavelength equals the product of the phase number and electrode pitch.

Further to Masuda and Melcher's work, Schmidlin [27] put forward another motion mode, called surfing mode, in which particles slide or roll along the conveyor surface. Surfing mode is desirable in the transport of toner particles for electrophotography. Schmidlin suggested that a large particle adhesion force may transfer motion from hopping mode to surfing mode.

By summarizing and unifying the usage of different terminologies, the particle motion in an ETW field can be classified into four different modes:

1) Curtain mode: Particle moves in a cyclic motion with small average velocity;

2) Hopping mode: Particle drops onto the surface and bounces forward or backward;

3) Surfing mode: Particle slides or rolls along the conveyor surface;

4) Vibration mode: Particle spins with a small displacement.

Note that particles can move forward or backward. For example, a particle may move backward and the particle velocity can be changed instantaneously in hopping mode. The explanation of backward motion has been attributed to the second harmonic wave of the ETW field [23, 24]. Particles in vibration mode spin in a certain area with nearly zero displacement, which appears with relative high frequency electric fields.

This chapter later provides a comprehensive review of particle movement in ETW fields, introduces the development and application of ETW methods and identifies research gaps. The experimental platforms of the electric curtain, EDS and ETW are very similar. Further, as will be shown, these technologies use the same theory, similar electric field calculation methods, and simulation methods on particle trajectory. The electric curtain and EDS are therefore included in this review. In the following sections, ETW will refer to the basic theory and be used as a general term for the physical methods, while electric curtain and EDS will refer specifically to their industrial applications.

A schematic (Fig. 2.6) summarises the applications of the electric curtain, EDS and the controlled movement of particles using ETW.

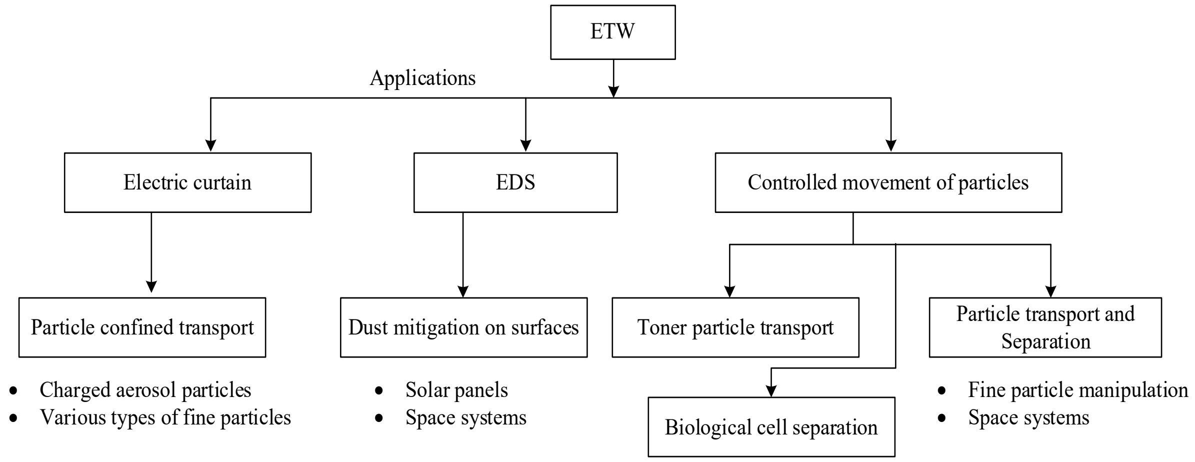

Fig. 2.6 Schematic of application areas using ETW methods and specific terminologies.

2.1.4 Literature Classification

Previous research applications can be divided into three categories: dust mitigation, particle transport and particle separation, shown in Table 2-1. Within the three categories, this review further classifies dust mitigation systems according to usage conditions and environments, and further classifies particle transport and separation according to particle type. This makes explicit links between different research areas that use the similar ETW methods and research directions.

Table 2-1 References classified by different applications and objectives

Application		Objective of study	Reference
Dust mitigation	Solar panels on Earth	Comprehensive research on mechanism and performance analysis of dust mitigation	[12, 32, 36, 37, 41, 44, 53-66]
		Particle trajectory simulation on solar panels	[11, 33, 67-70]
		Effect of particle size on dust mitigation	[38, 71-73]
		Effect of humidity on dust mitigation	[74]
		Force analysis on dust mitigation processes	[35, 43]
	Mars conditions	Experimental research	[75-80]
	Moon conditions	Experimental research and simulation	[81-87]
	Mars and Moon	Exploration of dust mitigation	[13, 14, 55, 77]
Particle transport	Fine particles	Mechanism of particle transport, experimentally and by simulation	[20, 27, 31, 34, 39, 51, 52, 88-96]
	Toner particles	Demonstrate controlled motion of toner particles, experimentally and by simulation	[25, 26, 97-103]
	Lunar soil	Experimental research and simulation	[104, 105]
	Sample of asteroid soil	Experimental research	[106-108]
	Metal pieces （copper, bronze and steel）	Experimental research	[109, 110]
Particle separation	Biological cell separation	Calculation of electric field and DEP analysis	[23, 111-116]
		Cell movement research: experiments and simulations	[23, 24]
	Fine particle separation	Platform design for particle separation	[28, 30, 117-119]
	Lunar particle separation	Demonstrate lunar particle separation experimentally and by simulation	[9, 120]

Considering the complexity of particle motion analysis in an ETW field and the diverse applications of ETW methods, direct comparison between the effect of experimental parameters and conclusion of results of different research groups are scarce. There remains many fundamental theoretical aspects of ETW that are unexplored, rendering further development and implementation challenging.

2.2 ETW Systems Development

This section describes the development of ETW equipment designs and their performance at laboratory and industrial scale.

2.2.1 Electric Curtain

The early work of Tatom et al. [42] and Masuda at al. [20-22] was developed further [20, 23, 26], with a focus on practical applications, systematic theory and experimental methods. The first application aimed to transport charged aerosols in a spatially periodic, non-uniform field [20]. Charged aerosol particles moved mainly by gravitation, and the electric forces was used to confine their trajectories. The research investigated electrode types (Fig. 2.7) and voltage phases and demonstrated flexibility in handling charged particles. Using a non-uniform travelling wave field, Masuda at al. [24] explored biological applications by moving cells in a fluid. Different electrode types and configurations were tested to protect cells from damage during transport and separation, and to improve the efficacy [23, 24]. In the lower area near the electrodes, harmonic components of the travelling wave field become more dominant. Due to the action of harmonic waves, heavier or less charged cells near the electrodes moved backward, which could be utilized for cell separation. Two types of two-wave component systems were developed to research the effects of harmonic waves [24]. One type was constructed by superposing two different waves, three-phase and six-phase waves, on the electrodes simultaneously, and the other type was constructed by two electrode arrays paralleled with a space. The results showed that the moving direction of cells was related to the distance between cells and electrodes, where the proportion of harmonic component was different. This proved the effect of harmonic waves on moving direction of cells.

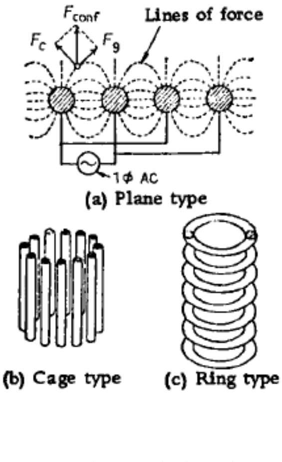

Fig. 2.7 Three types of different constructions of electric curtain: plane, cage and ring [20].

Subsequent efforts were made to understand the observations quantitatively and to design improved test devices for charged particles. First, Yen and Hendricks designed a double electric curtain composed of two parallel series of electrodes to trap specific particles from air flow with either gravity or air drag, as shown in Fig. 2.8 [25]. Then, Schmidlin [26] developed a new vertical toner transport system for digital printing technology. Melcher et al. [88, 89] combined a numerical model and dimensionless analysis to explore the theory of particle movement in an ETW field applied with six-phase voltage. It was found that the frequency of applied voltage was the predominant factor determining the particle motion mode [89].

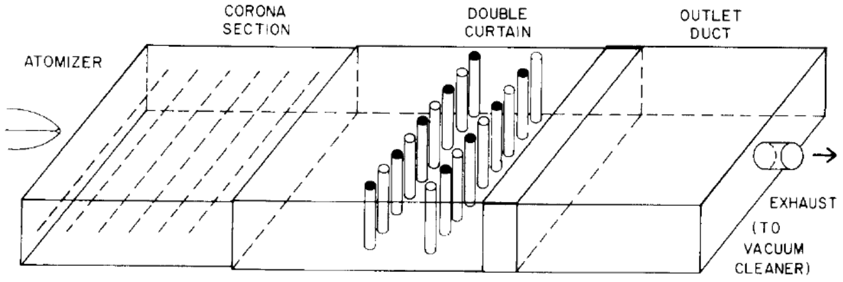

Fig. 2.8 Particle trap double curtain system. Bars with different coloured ends have opposite polarities [25].

Comprehensive analyses of the effects of viscous drag, particle mass, gravity- and electric fields [52], and numerical simulations were used to improve the performance of a charged toner transport device [88]. Schmidlin [26] subsequently developed a new xerographic system that can transport toner particles vertically. It was found that these particles may ‘flock’ together and move along with the travelling wave.

The phenomenon that particles move backward under certain conditions has been utilized to separate biological cells [23, 24] and agricultural seed by-products [121]. These papers explained that the backward motion was due to the harmonic waves in the field. Schmidlin [27] revisited the particle motion modes using numerical analysis, claiming that the reason for backward motion may be more likely due to the space charge and collision between particles with conveyer surface than the effect of harmonic waves. Backward transport in simulations using single pure wave may be an artifact of large incremental time steps. Therefore, the backward movement of a single particle in a fluid observed experimentally [23] still could not be explained thoroughly [27]. Recently, Zouaghi and Zouzou [32, 33] have analysed the effect of harmonic waves using numerical results of simulations, which suggested the backward motions were due to the harmonic waves. However, the backward trajectories shown in their papers were in hopping mode and included contacting with the conveyer, so the effect of collision between particles and conveyer may also contribute to the backward motion.

The oscillatory behaviour of lycopodium particles in plane type electric curtains has been researched in detail by Dudzicz [122-125]. Particles entering the electric curtain were observed to move in four ways: 1) oscillate near electrodes steadily; 2) oscillate above and below the curtain; 3) slow down near electrodes or leave the curtain; 4) travel from one electrode to another. The space above the electrodes was classified into two regions according to the angle of vibration path related to the centre of electrodes: designated separation region and saddle region. In the separation region, the oscillation path of the particle changed significantly with small change of charge. While in the saddle region, particles moved more stably and were more easily confined [122]. Using the region of separation, particles with different charges could be separated according to their different trajectories [123]. The frequency of the applied voltage had a large influence on the position of two regions. The range of frequency 20 to 80 Hz was found as the best for dust precipitation and particle separation [124]. A DC voltage has been added to the electrodes to create hybrid-type electric curtain, which provides more options to control particle trajectory [125].

2.2.2 Dust Mitigation (EDS)

EDS, using AC electric fields, has been widely studied for dust mitigation systems, particularly on solar panels. Experimental platform and typical configurations are shown in Fig. 2.9 and Fig. 2.10.

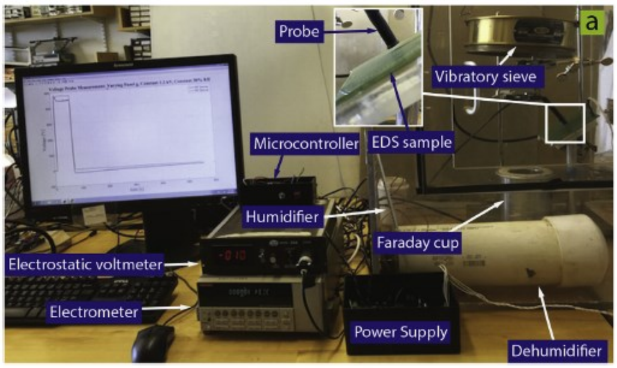

Fig. 2.9 Experimental platform for the measurement of the ratio of charge to mass with environmentally controlled conditions [64].

Fig. 2.10 Field test of EDS system from CleanFIZZ at KAUST near Jeddah in Saudi Arabia [62].

Experimental investigations and numerical simulations of dust mitigation used on Earth or in space have received increasing attention and have been conducted by many researchers, notably the group of Calle at the NASA Kennedy Space Center [13, 14, 55, 56, 77, 78, 85], the group of Mazumder in the University of Arkansas at Little Rock [12, 36-38, 44, 57, 59, 65], the group in Qian Xuesen laboratory of space Technology, China Academy of Space Technology [39, 91, 126], the group of Kawamoto in the University of Waseda [53, 76, 81-83], the group of Noureddine in the University of Poitiers [32-35], the group of Guo in Texas A&M University [11, 41, 63, 66, 74], and the group of Amar in Djillali Liabes University of Sidi-Bel-Abbes [73, 110], and recent researches [40, 127-129]. Their research and findings are classified into the following sections.

2.2.2.1 Terrestrial Conditions

1) Effect of particle size and electrode configuration

Johnson at al. [72] and Biris at al. [54] researched the effect of particle size and charge on dust removal efficiency (DRE), which was defined as the percentage of dust removed from the initial amount of dust on the screen. The electrode voltage was set as a 5 Hz square wave with amplitude ranging from 6 to 7 kV. Two JSC Mars-1 dust simulants were tested. The DRE for the coarser dust (5.8 µm median size, 14 to 20 µm more abundant) was significantly higher than for the finer dust (5.2 µm median size, 0 to 5 µm particles more abundant). Increasing the electrodes spacing from 1.26 mm to 2.54 mm reduced the DRE. However, pre-tribocharged particles were removed more efficiently with 1.26-mm than 2.54-mm electrode spacing. The combined effect of voltage frequency cannot be omitted. The experimental results by Ahmed and coworkers [73] showed that for Polyvinyl Chloride (PVC) particles: 1) if the particle size was 90 µm, the frequency of voltage at 33 Hz and spacing at 0.5 mm was the optimal design; 2) if the particle size was 125 µm, the frequency of voltage at 15 Hz and spacing at 1.0 mm was the optimal design. They used MODDE 05 program to estimate that if the particle size was 250 µm, the frequency of voltage at 10 Hz, and the spacing at 0.8825 mm, it would result in the optimal design.

Sayyah et al. [38] included the effect of particle size distribution on the loss of energy from sunlight. Electrode width was 80 µm and interelectrode spacing varied from 400 µm to 800 µm, by 100 µm increments. The duty cycle of the applied voltage was 50%, with a voltage amplitude of either 1 or 1.5 kV, and a frequency of 5 Hz. The particle size distribution on the screen showed that higher voltages removed more and smaller particles. In addition, increasing the screen tilt angle improved dust removal performance. If the angle was larger than or equal to 40°, interelectrode spacing had little effect on dust removal. Through analysing forces on different sizes of particles, Zouaghi and coworkers [35] found that the efficiency of EDS decreased with the increase of particle size due to the larger gravitational force on them.

Research on the movement mechanisms for different sizes of particles is reviewed in section 2.3, which is helpful for the design of EDS.

2) Effect of charge to mass ratio and humidity

The particle charge state affects the performance of the system. In most terrestrial applications, particles are initially neutral and the forces exerted by ETW fields are due to DEP force. As the particles contact the dielectric layer and each other, they may become tribocharged. In the lunar environment with high vacuum, ultraviolet radiation, solar wind and zero humidity, particles are likely to have an initial charge [130]. Unfortunately, few studies of ETW systems have measured or reported the charge state of particles.

Kawamoto et al. [51] measured the charge of initially neutral particles (density about 3.5 kg/m^3 and size from 30 μm to 110 μm) transported on an ETW conveyor, covered with acetate rayon film (3M, 810-18D), using a Faraday cage and free-fall methods. They found that particles were charged to −0.01 to −0.03 μC/g by contacting with the surface of the dielectric layer. The charge distribution evolved over time into two peaks, explained by tribocharging between particles. They further compared the charge density as a function of particle size and found that the surface charge density on small particles, especially smaller than 40 μm, was higher than on large particles due to the ratio of superficial area to mass [9].

Sayyah et al. [64] investigated how electrode width, spacing, voltage type and relative humidity affect the Q/M (charge to mass ratio) of particles in an EDS system. Particles used in the experiments were JSC Mars-1A simulant dust and sieved by an 88 μm vibratory sieve. Electrodes were covered with a two stacked layer, optically clear adhesive film and borosilicate glass with relative permittivity of 5.14 and 5.5, respectively. Their measurements showed that a decrease in voltage and an increase in electrode width and spacing decreased the magnitude of electric field on the surface of screen, thus decreasing the Q/M of the particles.

Zouaghi and Zouzou [32] measured the charge of 50 to 300 μm spherical Poly (Methyl Methacrylate) (PMMA) particles after moving on an ETW conveyor made of epoxy resin reinforced with fiberglass (relative permittivity: 4.3). The results showed that the particles were mainly charged positively with a Q/M of several 0.01 μC/g.

Javed and Guo considered the effect of relative humidity on EDS performance, which showed that the performance decreased significantly with the increasing humidity [74].

In general, a larger Q/M led to higher clearing factor. However, measurements of Q/M indicated that the Q/M of Mars dust simulant, which had the highest clearing factor, was the smallest while the Q/M of lactose widely used in the pharmaceutical industry was the highest [54]. This demonstrates that other particle characteristics will affect their movement on the screen. The effect of material properties remains to be studied in greater detail.

3) Effect of dust deposition modes

Guo et al. [11] studied EDS performance under aerosol- and sieve deposition modes and various operational cycles. Aerosol deposition of dust is more realistic than sieve deposition [53]. The median diameter of the airborne dust was about 20 μm with a mean density of 78 mg/cm^3. A single square wave with frequency of 1 Hz and peak-to-peak value of 6 kV was applied to electrodes with width of 0.3 mm and pitch of 7 mm, covered by a 55 μm dielectric layer. Sieve deposited dust was easier to remove than aerosol deposited. Under single operation mode, a low rate of dust loading led to a decrease in DRE. Moreover, in cyclic-operation, with new dust loaded on the surface after each single operation, a certain amount of dust tended to remain on the screen after each cycle in aerosol deposition mode, which led to a continuous decrease of DRE with more cycles, while dust removal efficiency of sieve deposition mode was less affected by the number of cycles.

4) Effect of characteristics of travelling wave

The experimental system by Biris at al. [54] had 0.762 mm thick electrodes with a 1.524 mm gap between electrodes and the applied voltage was 10 kV at a frequency of 300 Hz. It was found that DRE increased linearly with an increase in voltage and varied little with frequency, which only affected the speed of removal. In addition, DRE decreased from pulse- to square- to sinusoidal applied waveforms. And tests of DRE of three dust types found that the Mars dust simulant was the easiest to clear, followed by acrylic powder, and finally lactose. Similar conclusions were obtained in [53, 119] that square wave was more effective than sinusoidal and triangular wave, because square wave has a higher root-mean-square (RMS) amplitude than the other two waves with the same peak value.

Since EDS can be regarded as a capacitance load, the charging time to peak wave can be adjusted by input current, resistance and the load of capacitance, which was proved to have an effect on the efficiency of EDS by Guo and coworkers [66]. They found that the efficiency of EDS in the condition of low rise time of voltage (100 ms to 6 kV_{pp}) dropped by 50% compared with fast rise time in cyclic operation mode [11]. The decreasing effect on EDS efficiency of rise time was also inferred by deposition mode and dust loading level in single operation mode.

5) Evaluation of energy cost

Sharma et al. [80] researched the energy cost of EDS relative to DRE. It was estimated that the average power for an EDS system was 0.017 mW/cm^2 to 0.049 mW/cm^2. If the width and spacing between electrodes was set to 127 μm and 508 μm respectively, DRE could remain above 90% and dust accumulated on the surface of screen would not exceed 0.64 mg/cm^2. However, adding an electrode layer on the solar panels led to a 15% power output drop.

6) Outdoor field test

EDS outdoor field testing has been conducted by Faes at al. [62] in Saudi Arabia and by Guo at al. [41] at Doha, Qatar, which revealed a difference between indoor and outdoor tests. Faes and coworkers [62] have found that different dust deposition rates had a significant effect on the capability of the EDS system. The highest DRE could reach 95%, however, the DRE may drop to 10% at relative higher dust loading density. Future designs of EDS need to consider local environmental conditions.

Guo and coworker [41] developed metrics of cleaning index, Cleaning Index Change Rate (CICR) and soiling loss to better evaluate DRE for the outdoor test of EDS. Three photovoltaic modules, active EDS, inactive EDS and reference model without EDS electrodes, were tested in the same conditions to make comparison. The electrodes of EDS were designed to 0.3 mm width and 7 mm pitch, and to which were applied a two-phase square wave, which was a lower cost compared with three- or four-phase waves. They found that this type of EDS could reduce loss by 16%-33% with the activation voltage of EDS at 9 kV_{pp}, while at 6 kV_{pp}, the efficiency of EDS was zero. The weather conditions like wind and rainfall were shown to have a significant effect on EDS efficiency.

Sayyah, et al. [58] compared the restoration of reflectivity of solar panels after cleaning by different methods: EDS, natural cleaning by rain and snowfall and manual cleaning by water and detergent. It showed that: the cleaning effect of natural rainfall on solar panels was related to the angle of inclination and surface glazing material. This report [65] showed that manual water washing cleaning could restore 98% of the original reflectivity, while EDS restored more than 90% reflectivity.

Guo and coworker [63] have also performed four-day short term field tests of EDS using outdoor soiling microscopy (OSM) method. The micrograph image of dust on EDS surface were used to quantify particles and their behaviour. It revealed that particles close to electrodes could be removed more successfully in the beginning stage of field test, and this position dependent phenomenon weakened with the increase of test time. In addition, particles that stayed longer on the surface were harder to remove, which may due to the increasing adhesion force. The proportion of dust mass removed by EDS decreased from 40% to 14% in the four-day test on average.

2.2.2.2 Martian and Lunar Conditions

1) Test of Martian condition

Calle, et al. [13, 78] researched the performance of an electrodynamic dust shield system under simulated Martian atmosphere conditions of 0.93 kPa CO_2. Concerning the electrical breakdown at low atmospheric pressure, the amplitude of voltage applied to electrodes was lower than 800 V [78]. Despite the relatively low electric field strength during the test, the EDS performed exceptionally well even after running for an extended period, because the lower atmospheric pressure and dry conditions decreased the required electrostatic forces for particle movement. Experiments of dust clearing performance of thermal radiators on spacecraft have been conducted under similar experimental conditions and the results indicated that DRE can reach up to 99% with 50 mg of 50 – 100 μm sized JSC-1A dust delivered to each 10 cm × 16.7 cm dust shield [13].

Atten and coworker [79] tested the performance of dust removal in air and CO_2 atmosphere with different level of pressure, respectively, using a standing wave field. Certain applied voltages on electrodes could generate dielectric barrier discharges (DBDs) in the gas, which was found to be helpful to charge particles and improve particle removal efficiency. Under low pressure conditions, the design of the electric curtain should have a high ratio of the applied voltage for DBD to the distance between electrodes. This generates a larger electric field to overcome the influence of strong adhering force.

2) Effect of electrode configuration

In Calle et al. [13], the experiments were conducted under three electrode width and spacing configurations: width and spacing between electrodes set to a) 0.6 mm and 2.0 mm; b) 0.5 mm and 1.5 mm; c) 0.3 mm and 1.0 mm, respectively. The effect of electrode configuration is complex, as increasing the width enlarges the magnitude of the electric field, while increasing the spacing has the opposite effect. The minimum voltage amplitude required for particle transport decreased linearly as the frequency decreased and it was the lowest in the configuration of b, followed by a, and the highest in c.

Detailed research about the effect of electrodes configuration was also conducted by Calle et al. [77]. They showed that increasing the spacing between electrodes decreased the clearing factor, and this effect was the most obvious in the Martian atmosphere at 0.4 kV. When electrode width varied from 0.3 to 0.4 mm, the four types of electrode pitch (sum of width and space between electrodes), set at 0.48 mm, 0.55 mm, 0.6 mm, 0.67 mm, respectively, could recover the output voltage of solar panels to above 90% after activating the system in lunar conditions at high vacuum [14, 85].

3) Effect of wave type and frequency

Dust simulant of Mars JSC-1, lunar JSC-1a, and Minnesota simulant were tested under Martian and lunar conditions [77]. Operating frequency had no effect on DRE at 1.5 kV and little effect at 0.4 kV. In addition, it was shown that a sinusoidal travelling wave contributed more to the rolling of particles and a square wave contributed more to the lift of particles.

4) Dust removal for spacesuit

Kavya and coworkers [86] researched the possibility of dust removal from lunar spacesuits using EDS. Yarns made of Carbon Nanotube (CNT) flexible fibres were used to make electrodes for EDS, which has exceptional mechanical and conductive properties suitable for spacesuit conditions. CNT fibres were embedded into “orthofabric” material to test its performance. CNT fibres diameters were 200 to 215 μm with two types of spacing between electrodes, 1 mm and 1.6 mm. The results showed that EDS could efficiently repel nearly 90% of dust dropped to surface and 80% to 95% of dust deposited on the surface in advance. In addition, the work function matching (WFM) coating created by ion beam sputter deposition with a similar work function as the lunar simulant was added to the surface to test DRE. This showed very similar performance compared with uncoated EDS. The advantage of WFM was that it could be used as passive precipitation technology by reducing electrostatic adhesive force on dust particles. A more complete Space suit Integrated Carbon nanotube Dust Ejection/Removal (SPIcDER) system was developed on the knee part of spacesuit [87]. In the scaled test, only 4 to 16% of area remained uncleaned and the increase of voltage showed increased cleaning efficiency. A safety risk analysis in the operation of this system addressed four risk areas: 1) human exposure to CNT material; 2) hazardous electric fields; 3) electric arcing; 4) oxygen rich atmosphere.

2.2.3 More Controlled Particle Movement

Machowski and coworkers [28] performed experimental and simulation research to separate particles using three-phase travelling waves. The travelling wave field was composed of harmonic waves. If the second harmonic wave was large enough, it could transport particles in the opposite direction of the basic travelling wave. Different types of particles could be separated by moving in different directions. Cylindrical and stripe electrodes with different widths and pitches were tested, while triangle electrodes were not suitable due to low second harmonic wave strength. Sand and pulverised alumina powders with mean diameters of 192 μm and 40 μm were used. The results showed that particles could be separated in two frequency bands. At lower frequency, sand particles were transported following the direction of travelling wave, while alumina particles were transported in the opposite direction, with both of them in the hopping mode. At higher frequency, their movement direction reversed. Small particle alumina powder flew higher in curtain mode in the direction of travelling wave and sand moved slowly in the opposite direction in hopping mode. In addition, conveyers with higher ratio of electrode width to pitch had a higher separation efficiency.

This same group studied the transport of cohesive lactose powder (150 mesh) [118], which were successfully transported if the applied voltage exceeded 3.5 kV_{pp} with the frequency between 40 to 130 Hz.

2.2.4 Application to In-situ Resource Utilization

The electrostatic travelling wave methods have received significant attention in the area of ISRU, which refers to the use of natural resources from space, such as the Moon and Mars [131]. ISRU can produce fuel and consumables to reduce terrestrial launch mass and dependency in deep space missions [132].

Successful implementation of ISRU mining technology requires a complete process with stages of excavation, beneficiation, and extraction [133]. Beneficiation reduces the raw regolith to a feedstock enriched in the appropriate material for the subsequent process steps. The first beneficiation stage could be achieved by the separation of particles by size. It has been shown that ETW methods can be used for lunar mineral beneficiation through size separation of regolith particles [104]. The group of Kawamoto at Waseda University, Japan, have made significant contributions to the application and theory development of particle separation and transport with ETW by doing both experimental and simulation research [51, 82, 92, 104, 106-108, 117, 134]. Their experimental research is introduced in this section and their simulation method will be introduced in section 2.3.

To simulate the Moon, experiments were conducted on the system in vacuum as shown in Fig. 2.11[9]. In this experimental platform, the conveyor was composed of parallel copper electrodes (thickness is 18 µm, width is 0.3 mm and interspace is 1.0 mm) and a polyimide cover (thickness 0.1 mm, width 128 mm, and length 490 mm). The applied voltage was a four-phase square wave and its amplitude was 1 kV. Different sizes of lunar regolith simulant FJS-1 particles (diameter 10 to 100 µm) were fed onto the conveyor. Particles floated and moved along the conveyor at different altitudes and could be collected at different heights above the conveyor. The charge density on small particles was larger and they moved higher. Particle separation was not successful under Earth ambient conditions due to the air drag force [117]. However, in vacuum, particles with diameters smaller than 20 µm could be separated effectively. Moreover, simulation results indicated that particles would lift higher under vacuum conditions. Therefore, the collection boxes needed to be set higher than under the same conditions on Earth. The yield of specific particles was not given [9, 104], and needs to be verified in future studies.

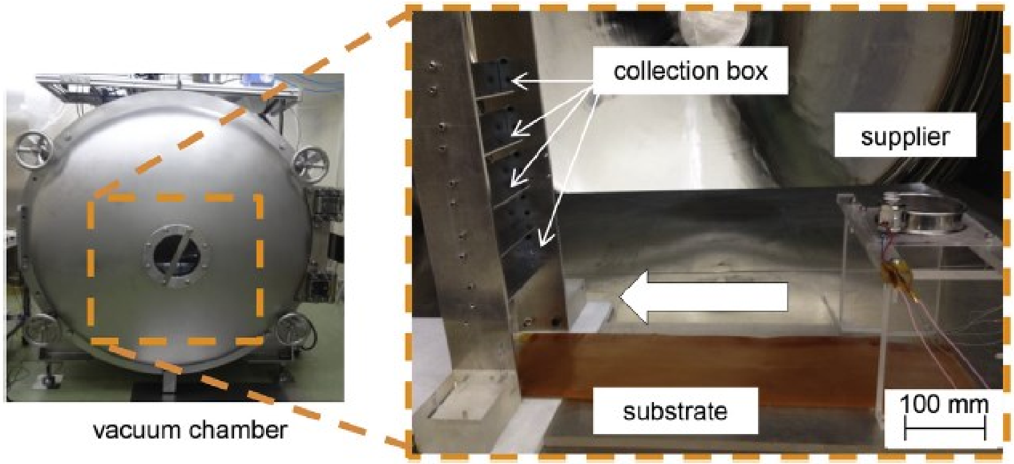

Fig. 2.11 Photographs of experimental set up for lunar particle separation in a vacuum chamber [9].

Vertical transport for lunar regolith and ice particles have been researched with the application of mining lunar icy regolith [105]. The schematic view and experimental photograph are shown in Fig. 2.12. A four-phase square wave was applied to ring electrodes around the tube. Effects of the pitch of the electrodes, the distance between the end of tube and the sample surface, the tube diameter, voltage amplitude and voltage frequency on particle transport rate were researched. The threshold for insulation breakdown was 4.6 kVpp, so 4 kVpp was selected. The test results showed that the optimal frequency was 30 Hz, and the optimal pitch and inner diameter of tube was 5 mm and 10 mm, respectively. The transport rate of 100 mg/min could be achieved in a 1-meter-long tube. Numerical simulation under lunar conditions using discrete element method (DEM) indicated this system could have an even higher performance due to low gravity and the absence of air drag. A similar vertical transport system [120] could be used to separate particles less than 10 µm with a lower applied voltage, like 1.0 kVpp. In this system, gravitational force on larger particles predominated, causing them to settle towards the bottom. The average size of collected particles was 12 μm and 30% of them were smaller than 10 μm in the box placed at higher platform using a four-phase 10 Hz square wave and a vibrated particle supplier,.

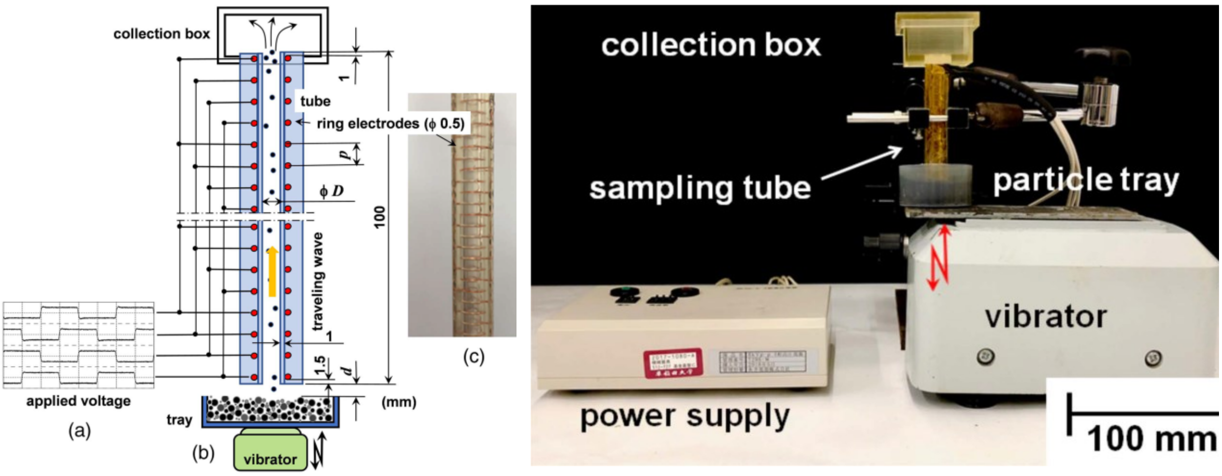

(a) Schematic view (b) Realistic experiment platform

Fig. 2.12 Experiment platform for the vertical transport of lunar regolith and ice particles [105].

2.3 Theory and Modelling

Development of ETW methods has evolved mostly along a “trial and error” approach in choosing operating parameters such as voltage type, electrode configuration and the insulating layer. The ETW methods have been applied in a wide range of fields including toner transport in electrophotography [26], dust mitigation on solar panels [44], space devices [13], and lunar soil particle transport and separation [9, 42]. A theoretical analysis of forces on particles [35, 43] and how particles move in an ETW field will allow for the selection of critical parameters and optimal design in these conveyor systems, particularly for manipulating the behaviour of particles of different sizes and composition.

2.3.1 Electric Field Calculation

2.3.1.1 Analytical method

Detailed knowledge of the potential distribution of the electric field in ETW systems is required to predict particle trajectories. Calculations assume a static electric field. Table 2-2 summarises the calculation methods applied in the literature to calculate the electric field for parallel electrodes where the DEP is the predominant force in the manipulation of particles.

The diagram for the calculation model is shown in Fig. 2.13. Generally, the length of the electrode is much larger than the width and pitch, so the variation of the gradient of electric field in the y direction is treated as zero. In addition, the height of particle transport is also much smaller compared with the size of the electrode array. Therefore, the electric field in the y direction is thought to be uniform and the electric field potential distribution can be converted to a two-dimensional problem.

Table 2-2 Review of electric field calculations (twDEP (travelling wave dielectrophoresis))

Electrode type/configuration	Field wave	Dielectric Layer on top	Force analysis	Calculation	Comparing Method	Reference
Cylindrical	Travelling	No	No	Substitute charge method	Travelling plane charge Approximation	[21]
Line (neglecting thickness)	Travelling	No	DEP	Green' theorem	Charge density method	[111]
Bar (neglecting thickness)	Standing And travelling	No	DEP twDEP	Fourier series	Experiment	[112]
Bar (neglecting thickness)	Standing And travelling	No	DEP twDEP	FEM Solver FlexPDE	Fourier series	[113]
Bar (neglecting thickness) With lid	Standing And travelling	No	DEP twDEP	Schwarz-Christoffel mapping	Fourier series FEM (COMSOL)	[115]
Top and bottom electrodes	Standing	No	DEP	Fourier series	FEM (COMSOL)	[116]

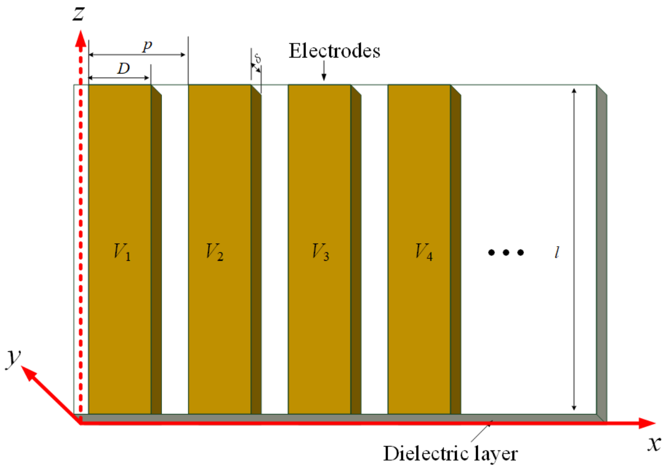

Fig. 2.13 Diagram showing the typical application system, consisting of the interdigitated electrode array. D is the electrode width, p is the electrode pitch, and δ is the electrode thickness, l is the electrode length. V_1, V_2, V_3, etc. represents the surface potential of each electrode.

The basic form for this two-dimensional electrostatic problem is expressed as Laplace's equation with boundary conditions (2.1):

$$\begin{cases} \dfrac{\partial^2 \phi(x,y)}{\partial x^2} + \dfrac{\partial^2 \phi(x,y)}{\partial y^2} = 0 \\ \phi(x,y) = V_1 \quad \text{on the surface of electrode} \\ \phi(x,y) = V_2 \quad \text{on the surface of electrode} \\ \phi(x,y) = V_3 \quad \text{on the surface of electrode} \\ \phi(x,y) = V_4 \quad \text{on the surface of electrode} \\ \cdots \end{cases} \tag{2.1}$$

V_1, V_2, V_3, etc. represent the surface potential of each electrode. ϕ is the applied voltage, which usually cycles with a fixed phase difference. Additional boundary conditions are provided by the potential falling to zero at infinity in x and y directions. The electric field is obtained by calculating the gradient of potential: $\boldsymbol{E} = -\nabla\phi$.

An example of the distribution of potential and electric field intensity above the electrodes are shown in Fig. 2.14 and Fig. 2.15. Fig. 2.14 is a contour plot of potential above the electrodes and Fig. 2.15 is a stream plot of the electric field above the electrodes. This electric field is calculated with four electrodes by the CSM and the potentials on the four electrodes are 800 V, 800 V, −800 V, −800 V, respectively. The black bars on the bottom of the two figures indicate the positions of four electrodes.

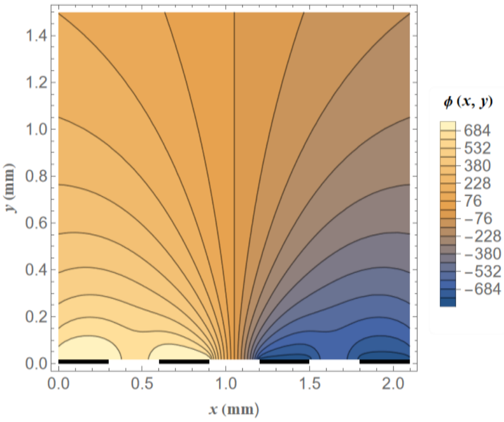

Fig. 2.14 Contour plot of potential above four electrodes with different polarities of voltage.

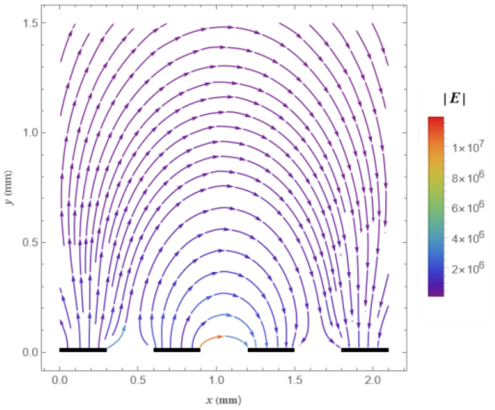

Fig. 2.15 Stream plot of electric field above four electrodes with different polarities of voltage.

Masuda and Kamimura [21] modelled the ETW field by introducing two first-order approximation methods and a more accurate approximation, the substitute-charge method, and compared the results. Then, they expanded the results using a Fourier series approach and found that the first and second modes played the predominant role. Finally, they compared the results of the three methods and showed that the application of two kinds of the first-order approximation methods became justifiable in the region X/λ ≥ 0.5 to 1.0 (X: height of calculation space, λ :wave length of the travelling wave).

In a later study, Wang et al. [111] used Green's theorem to calculate the electric field for two-dimensional electrode arrays, which can be used for the sorting and separation of biological cells. The Green's theorem approach to the solution of Laplace's equation can be stated in integral form using Green's second identity, as follows:

$$\int_V dV\left(\phi\nabla^2\psi-\psi\nabla^2\phi\right)=\oint_A dA\left(\phi\frac{\partial\psi}{\partial n}-\psi\frac{\partial\phi}{\partial n}\right) \tag{2.2}$$

Here ϕ and ψ represent any two continuous scalar functions; n represents the unit normal vector; dV and dA represent an infinitesimal volume and infinitesimal area respectively. ϕ can be set as the potential function that needs to be solved. In order to choose a suitable Green's function, they ignored the thickness of electrodes and assumed an infinite number of infinitely long electrodes were arranged in a horizontal plane. In addition, they made the approximation that the potential varied linearly with distance across the electrode gap. In this way, the function of ψ could be deduced by a mirror-image method.

$$\psi=\frac{q}{\left|r-r_0\right|}+\frac{-q}{\left|r-r_0'\right|} \tag{2.3}$$

where q represents a point charge, and $\left|r-r_0\right|$ represents the distance between the calculating point and the point charge, and $\left|r-r_0'\right|$ represents the distance between the calculating point and the mirror position of the point charge. The potential function related to r could be calculated as:

$$\phi\left(r_0\right)=-\frac{1}{4\pi q}\oint_A \phi\frac{\partial\psi}{\partial n}dA \tag{2.4}$$

They also provided a method to eliminate the approximation of linear potential variation between electrodes by assuming a homogenous dielectric material with a zero normal field component in the electrode gaps. With this boundary condition, they calculated the polynomial coefficients of the Taylor expansions of electric potential in the electrode gaps. The relative RMS error for the electrical potentials were 1.1% at the calculation height, the same quantity with electrode width and 3.6% at the surface of electrodes for the third-order polynomial. They compared their results for the potential distribution at a height y = 10 μm with the charge density method and the difference was mostly immediately above the electrode, as can be expected [111].

Morgan et al. [112, 113] developed two methods for calculating DEP force in electrostatic travelling fields. They first used the Fourier series of the potential function, equation (2.5), to meet the boundary conditions. The potential between the electrodes was assumed to vary linearly, as in [111].

$$\phi(x,y)=\sum_{n=1}^{\infty}A_n\cos(k_n x)e^{-k_n y} \qquad y>0 \tag{2.5}$$

where A_n represents Fourier coefficients and $k_n = 2\pi n/\lambda$, n is an integer, and λ is the wavelength. The A_n can be solved using the condition, $y = 0$ at the electrode plane. Note that equation (2.5) is the general solution to Laplace's equation for the space above the electrode plane. Morgan, et al. [112] compared the results of levitation height between their equation and experiments, finding deviations between 2.5% to 15%. Green et al. [113] specified the boundary conditions of the real and imaginary parts (ϕ_R *and* ϕ_I) of the potential function at the centre vertical boundary line of electrodes, equation (2.6), and the boundary conditions cycled within the whole domain. They used a Finite Element Solver to get a numerical solution. They found a deviation between the FEM and Fourier series methods of as much as 13%. By changing the FEM boundary condition to that of [112], the differences were reduced to 0.013%.

$$\begin{cases}\phi_R=0\\ \dfrac{\partial\phi_I}{\partial n}=0\end{cases},\quad \begin{cases}\phi_I=0\\ \dfrac{\partial\phi_R}{\partial n}=0\end{cases},\quad \cdots \tag{2.6}$$

Sun et al. [115] provided an analytical solution for these parallel electrode arrays and boundary conditions. The Schwarz-Christoffel Mapping Method was used to tackle the equations in the complex plane and they obtained the final expression in terms of Jacobian elliptic functions. However, in their calculation, they ignored the thickness of electrodes.

Gauthier et al. [116] developed a Fourier series method to calculate DEP force with two facing electrode arrays. However, they could only calculate the electric field with a given potential on the electrodes and the errors tended to be about 20% compared with FEM.

2.3.1.2 Finite Element Method

The COMSOL Multiphysics software has been used widely to analyse the potential and electric field distributions under complicated ETW structures using the FEM [68, 84, 135]. The advantage of FEM is that designers can change parameters at will. Through analysing the electric field of ETW systems with different parameters, such as electrode configurations and types of dielectric layer, they can qualitatively analyse how these parameters affect particles moving in such a system. However, the calculation accuracy of the FEM is closely related to the scale of mesh divisions, so proper mesh patterns need to be designed. For instance, at the edge of the electrodes and the dielectric layer where the potential changes rapidly, the size needs to be divided extremely finely, while further away from the electrodes it can be coarser [59]. The finite element results are, however, difficult to apply to predict the trajectory of a particle in motion.

2.3.2 Particle Movement Research

A theoretical understanding of the electric field distribution and how particles are transported in an ETW system will help to select relevant parameters in future applications such as a lunar regolith transport system. The forces affecting particle motion including the Coulomb force ($\boldsymbol{F}_{\mathrm{C}}$), dielectrophoretic force ($\boldsymbol{F}_{\mathrm{dep}}$), gravitational force ($\boldsymbol{F}_{\mathrm{g}}$), friction force, image force ($\boldsymbol{F}_{\mathrm{image}}$) and air drag force ($\boldsymbol{F}_{\mathrm{drag}}$) and any other forces which may be relevant in the particular case (Fig. 2.16).

The Coulomb force experienced by a particle will consist of the sum of the electric field intensity $\boldsymbol{E}_0$ generated by electrodes and $\boldsymbol{E}_q$ created by other charged particles [51]. Therefore, the electric field $\boldsymbol{E}$ at certain point can be obtained by:

$$\boldsymbol{E} = \boldsymbol{E}_0 + \boldsymbol{E}_q = -\nabla\phi + \frac{1}{4\pi\varepsilon_0}\sum_{n\neq i}^{N} q_N \frac{\boldsymbol{r}}{|\boldsymbol{r}|^3} \tag{2.7}$$

where ε_0 is the vacuum permittivity, N is the total number of particles in the field, q_{N} is the charge on a particular particle and r represents the distance between calculating point with n^th^ particle: $\boldsymbol{r} = \left(x_i - x_n, y_i - y_n, z_i - z_n\right)$. The Coulomb force on a particle is given by:

$$\boldsymbol{F}_C = \boldsymbol{E}\cdot q \tag{2.8}$$

The air drag on a spherical particle can be calculated as follows [33]:

$$\boldsymbol{F}_{\mathrm{drag}} = 6\pi\eta R\cdot\left(\boldsymbol{U}_g - \boldsymbol{v}_p\right)\cdot\frac{1}{C_U\left(R,\lambda_g\right)} \tag{2.9}$$

where η is the viscosity of air, R is the particle radius, $\boldsymbol{U}_{\mathrm{g}}$ is the flow velocity, $\boldsymbol{v}_p$ is the velocity of the particle, Cunningham factor C_U is related to the radius of particle and mean free path of the gas molecules, λ_{g}. Since the research referenced here takes place in air at atmospheric pressure, C_U can be assumed to equal 1, because R is several orders of magnitude larger than λ_{g}.

The DEP force on a single particle generated by the non-uniform electric field acts on the induced dipole moment of particles and can be expressed as [136]:

$$\boldsymbol{F}_{\mathrm{dep}} = 4\pi R^3\varepsilon_0\varepsilon_m\frac{\varepsilon_p - \varepsilon_m}{\varepsilon_p + 2\varepsilon_m}\boldsymbol{E}_0\cdot\nabla\boldsymbol{E}_0 \tag{2.10}$$

where ε_{p} and ε_{m} are the relative permittivity of the particle and medium.

Particles also experience a force from the image charge induced at the surface of the dielectric layer, at a certain height (y_p) above the surface, can be calculated as follows:

$$\boldsymbol{F}_{\text{image}} = -\frac{q^2}{4\pi\varepsilon_0 (2y_p)^2}\boldsymbol{n} \tag{2.11}$$

where $\boldsymbol{n}$ is a normal vector pointing up perpendicular to the surface.

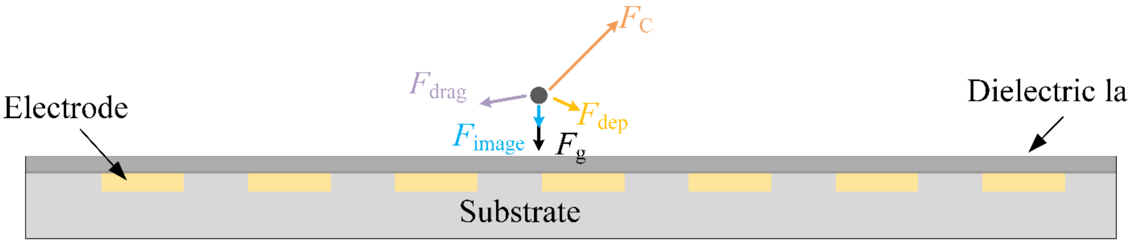

Fig. 2.16 Force diagram on single particle.

Particle motion on the transport system depends on the particle's physical properties and the imposed electric field. Experimentally, the total weight of particles can be measured by an electronic balance and the total charge of particles can be measured by an electrometer or Faraday cup. The electric field calculation methods have been discussed and methods of simulating particle trajectories in that field are introduced in this section.

The simulation of particle motion in an ETW field can be divided into two categories: single particle simulation and multiple particle simulation. Single particle simulation is easier to implement and can qualitatively evaluate the effect of the forces acting on particles and the effect of different electric fields on particle motion modes. Multiple particle simulations that also consider particle collisions are closer to physical reality and therefore more useful for equipment design and operation quantitatively.

2.3.2.1 Single Particle Simulation

To simulate single particle movement, the equations of motion need to be solved:

$$\begin{cases} m\dfrac{d^2x}{dt^2} = \sum F_i \\ m\dfrac{d^2y}{dt^2} = \sum F_j \end{cases} \tag{2.12}$$

where m represents mass of particle; x and F_i represent the displacement and forces in the horizontal direction; y and F_j represent the displacement and forces in the vertical direction.

David and coworkers [93] used Runge-Kutta method in solving the equations of motion. As for the electric field calculation, they built a computer interface and users can choose from three different field solving methods: analytical method, numerical method, and a combination of numerical method and analytical method according to the users' accuracy acquirement. The simulation results showed that levitation height would be higher with the increase of voltage in curtain mode. And both simulation results and experimental results showed that particle's levitation height decreased with the increase of frequency [94].

Kawamoto and Hayashi [90] have performed simulations and experimental research on the basic mechanism of movement of single liquid drop and soft body. The pitch of the electrodes was 2 mm and the movement of particles of three diameters was researched experimentally: a) less than one pitch; b) between 1.5 and 2.5 pitches; c) larger than 3.5 pitches. For a type c, liquid drop, the positive and negative Coulomb forces tended to be similar due to its large size across three electrodes, so the electrokinetic effect on it was cancelled. A four-phase wave with wavelength covering four electrodes was more effective to move type c liquid drop than three-phase wave. A type b liquid drop was in a stationary polarization stage when the voltage was constant and only moved with the transition of voltage. A type a liquid drop was easier to transport due to its smaller size. The moving direction of three types of liquid drop was explained using the schematic drawing of the polarity of electrodes along the direction of the travelling wave.

In order to optimise removal efficiency, Horenstein et al. [69] simulated the trajectories of single particle in an EDS system under different conditions. A Fourier expansion method was used to solve Laplace's equation. They divided the simulation time into n parts (Δt) and precomputed the electric field for each type of boundary condition at each time period. For each discrete time step, the vector sum of forces acting on the particle ($\sum F_n$) was calculated, then the acceleration, velocity (U) and displacement (dx) of the particles and for the vertical direction.

$$\begin{cases} \mathrm{d}U = \left(\sum F_n / m\right)\Delta t \\ \mathrm{d}x = U\Delta t \end{cases} \tag{2.13}$$

In addition, they assumed that when a particle contacted the EDS surface, its perpendicular velocity and parallel velocity retained 25% and 90% of the incoming value, respectively. Therefore, with the discrete time step method, the position of the particle could be calculated for the full-time scale. With this simulation method and in comparisons with experiments [70], they studied the effects of charge-mass ratio, particle radius, electrode spacing and starting positions on the particle movement. The key conclusions were that smaller particles tended to move more synchronously with the travelling wave and the initial position of a particle could lead to different chaotic trajectory.

Recently, Zouaghi and Zouzou made similar simulations, but delved deeper into the theory of particle motion [33]. They calculated the electric field using the same Fourier expansion method as

Masuda et al. [23] and analysed the effect of the first and second harmonics of the travelling potential wave on motion of particles.

$$V(x,y,t) \approx W_{for} + W_{back} = V_0 \left[\frac{3}{2} a_1 e^{-\frac{2\pi}{\lambda} y} \mathrm{Cos}\left(\frac{2\pi}{\lambda} x - \omega t \right) + \frac{3}{2} a_2 e^{-\frac{4\pi}{\lambda} y} \mathrm{Cos}\left(\frac{4\pi}{\lambda} x + \omega t \right) \right] \tag{2.14}$$

Here V_0 is amplitude of the voltage on the electrodes, and a_1 and a_2 are the coefficients of first order and second order Fourier series based on their simulation model.

Zouaghi and Zouzou [33] also added the effects of the image-, DEP-, gravitational- and drag forces. Moreover, they ignored the thickness of the electrodes and dielectric barrier and assumed an elastic collision on the contact between particle and conveyor surface, which meant that the particle's perpendicular velocity was reversed and parallel velocity remained constant. They divided the second order differential moving equation into four first order equations (2.15). Similar simplifying methods were used by Jie et al. [67].

$$\begin{cases} v_x = \dfrac{dx}{dt} \\ a_x = \dfrac{dv_x}{dt} \\ v_y = \dfrac{dy}{dt} \\ a_y = \dfrac{dv_y}{dt} \end{cases} \tag{2.15}$$

where v_x and v_y are the velocity in x and y direction, a_x and a_y are the acceleration in x and y direction.

Through analysing single particle trajectory under different simulation parameters, Zouaghi and Zouzou found that the initial position had a large effect on the initial movement, but had little effect on the average velocity of the particle in steady state. The particles' trajectories with different departure positions are shown in Fig. 2.17. Backward motion was thought to be caused by backward harmonic waves. They concluded that analysing the effect on particle levitation height and displacement and optimising the frequency were necessary for EDS optimisation.

As for the effect of initial position, Sun and co-workers [115] found that well charged particles located on the top of electrodes tended to enter into hopping mode and particles located between electrodes had transverse movement along the surface in a standing wave. However, in large scale multiple particle motion, the overall behaviour of particles was essentially independent of the initial position of particles, which was confirmed by Thomapson and Gartstein [95, 97]. This may because that the effect of initial position was averaged for multiple particles. The conclusions are consistent with that of research on single particle motion.

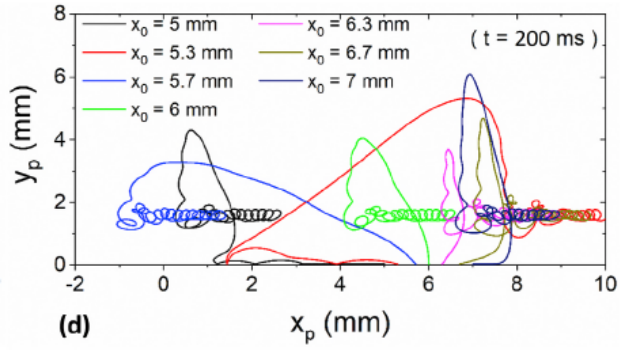

Fig. 2.17 Trajectories of particles with different departure positions (x_0 represents departure position) [33].

2.3.2.2 Multiple Particle Simulations and Experimental Research

The approach to multiple particle simulation picture is quite different to single particle [95]. In order to improve the understanding of particle motion and performance of particle separation using ETW, Adachi et al. [9] simulated multiple particles' trajectories and compared the results with experiments. First, the potential distribution was calculated with the two-dimensional finite element method in a cyclic domain of two-pitch width. Then, a series of force formulas involving electric field strength and particle parameters was presented. Finally, a three-dimensional modified hard-sphere model was introduced into the DEM simulation model, which takes the collision order between particles into account. The modified hard-sphere model has higher accuracy than hard sphere model and can significantly reduce computation time [96]. The motion equations were calculated using Runge-Kutta method. Through the numerical results, the authors studied the effects of frequency and concluded that:

i. The direction of particle transport was related to the frequency of the applied voltage;
ii. Particles moved synchronously with the travelling wave at low frequency;
iii. Some particles' velocities were slower than the travelling wave velocity at medium frequency;
iv. Most particles were transported backward at relative high frequency and were not transported but only vibrated at very high frequency.

Moreover, Adachi et al. [9] predicted particles' motion both in air and vacuum and illustrated particles' motion and maximum height. The results indicated that particles would float higher in vacuum than in air. And in air, smaller particles, with relatively higher drag force, would not fly as high as larger particles.

Liu and Marshall [31] adopted a soft-sphere model to simulate multiple particles and research the effect of particle adhesion and collisions on motion modes. They considered soft-sphere model more realistic as hard-sphere models are too fast for simultaneous collisions for a single particle. They used the BEM to calculate the electric field and decoupled it for a time-varying electric field. To reduce the computational cost, they used a box-particle multiple expansion method and dimensionless models.

They introduced the “sweeping effect”, in which synchronous moving particles could sweep forward low charge particles. Adhesion forces hindered the particle motion and affected the motion mode of particles. They observed both forward and backward transport at high frequency, while forward-moving particles tended to have a higher charge. Finally, they claimed that higher charge particles lofted to higher altitudes, which may be utilized for the separation of particles.

Gu and coworkers [91] performed multiple particles simulations based on the Hertz-Mindlin contact model using DEM. The computational domain was restricted to 14.66 mm long (consisting of 12 electrodes) and the voltage was a four-phase square wave. The quantity of simulated particles was 10,000 and their size distribution and properties were consistent with lunar regolith simulant FJS-1. Detailed analyses for particle lifting from the conveyer surface were provided and the relationship between the particle’s velocity and applied frequency was studied. The results showed that particles could get a higher backward transport rate at 1.04 m/s when the frequency was at 200 Hz, which was thought to be utilized in the transport of particles. The applied frequency and electrode configuration affected the particle’s moving direction simultaneously. Experimental results within their designed platform showed that particles could also be transported backward at very low frequency, such as 2 Hz [39].

Digital printing technologies in electrophotography have also studied ETW theory for application to toner particles. Kober [98] researched the differences in motion between conductive and insulating toners. The conclusions were:

i. Insulating toner must be charged before it could be transported.
ii. The toner charging and the moving velocity mainly depended on the magnitude of the electric field intensity.
iii. Toner particles with smaller size and higher conductivity moved faster and the critical frequency, at which particle’s travelling direction reversed, was higher.

In contrast to the finding of Zouaghi and Zouzou [33] for a single particle, Thompson [97] found that multiple particles’ behaviour was essentially independent of the initial particles’ positions because the total electric field was not only generated by the travelling wave but also influenced by other charged particles and their image charges. This ensemble electric field may led to a self-consistent behaviour of multiple particle movement, in a large scale, which was not affected by the initial positions [97]. Taniguchi et al. [99] stated that mechanical vibration of the system could improve the driving characteristics.

Lunar soil particle transport and separation by size has been conducted by Kawamoto and coworkers [9, 104, 106], which is introduced in section 2.2.4. Kawamoto et al. [83] found experimentally that the maximum transport rate of lunar soil simulant FJS-1 was 13 g/min for an ETW conveyor with a width of 100 mm using mechanical vibration to assist particle transport. In the size separation system developed by Adachi et al. [9], particles smaller than 20 μm could be collected at 250 mm height and particles of about 10 μm could be collected effectively at 1.5 m height under vacuum. However, there was a trade-off between separation rate and collection, with a higher separation rate resulting in smaller collection amounts. The main cause was the accumulation of particles on the conveyor and the interaction between particles that hinder their movement. Testing the system must be performed under a high vacuum to avoid arcing at the voltages required for transport.

2.3.2.3 Summary

Table 2-3 summarises the major simulation and experimental studies of particle transport by ETW methods. Particle charge, transport rate, transport direction, transport mode, effect of particle collision and adhesion, and levitation height of particles have been researched.

There were four main findings:

1. The charge-to-mass ratio was affected by contact with the dielectric layer. After repeated contact, particles became saturated and the saturation charge was largely related to their physical properties.
2. The transport rate of particles was affected by voltage amplitude, voltage type (wave form and phase number), electrode configuration and frequency of voltage. Larger voltage amplitude generated a larger electric field, thus increased transport rate of particles.
3. The frequency of applied voltage was a critical parameter that influenced transport rate and motion direction of particles. Particles may move backward at higher frequencies. However, high frequency is ill- defined because different research groups used different experimental parameters and their conclusions about the boundary range of low and high frequency was different.
4. The levitation height of particle was affected by particle mass and charge. Collecting particles at different height could be used to separate particles.

Table 2-3 Summary of selected prior research, collated in columns by research group

Research Group / Parameter	Kawamoto, et al. [9, 51, 104, 117]	Marshall, et al. [31]	Zouaghi and Zouzou [32-34]
Particle type	ACM particles made by the polymerization method (Toda Kogyo): density at 3.5 g/cm^3	Simulation particle: density at 3.5 g/cm^3; relative permittivity: 3	PMMA particles: density at 1.2 g/cm^3; relative permittivity: 2.8

Measurement of charge on particles	Initial charge: −0.01 to −0.03 µC/g, increased with vibration to saturation	Mean value of charge: −8.53 10^{-9} µC; Standard deviation: 9.22 10^{-9} µC	Most positively charged and the charge per gram was of the order of 0.01 µC/g.
Voltage amplitude	Transport rate increased linearly with voltage (with a threshould voltage)	Only simulated with 1.6 kV	Particles velocity stagnated at a certain critical value
Voltage type	Square wave was the most effective (RMS field strength)	Only simulated with square wave	Only used square wave; Travelling wave was more effective than Standing wave; More particls moved backward at four-phase low voltage
Electrode parameters	Particle was not transported if particle radius was 3.5 times larger than electrode separation	Only one type: Width: 1 mm Separation: 2 mm; depth: 40 um;	Small width/gap values decreased the ratio of particles moving backward
Frequency	Transport rate increased with increasing frequency at low frequency; Forward with low frequency; Backward with high frequency; Non-transport with extremely high frequency > 250 Hz; Critical frequency is linked with particle size and electric field	At high frequency, particles were transported both forward and backward.	20 Hz to100 Hz, average velocity continued to increase ; above 100 Hz, average velocity droped with the increase of frequency; At low frequency, particles moved forward. Over 50 Hz, a considerable amount of particles moved backward;
Particle charge	Not researched	The forward-moving particles tended to have higher	High Q/M particles moved forward Lower Q/M particles moved backward

		charge than the backward	
Levitation height	Decreased with increasing particle size	Increased with particle charge magnitude	Maximum levitation height increased with frequency at first and then decreased with further increase of frequency

2.4 Research Gaps Identified

2.4.1 Development Needs

Simulation research methods allow a deeper understanding of the mechanism of particle transport in an ETW field. In recent years, multiple models and simulation methods have been applied to explore this transport theory. Considering these studies together, there is a lack of consensus on the nature of particle motion modes with variation in conditions, and also which parameters dominate particle velocity. A more comprehensive investigation using simulation based on the combination of different parameters is needed. In addition, single particle experiments have not been reported, so simulation results of single particle motion have not been verified with controlled experiments.

The literature review has highlighted four key limitations in the existing research:

i. ETW is applied in widely diverse fields, including cell separation, dust mitigation of solar panels, lunar beneficiation and toner particle transport. This diversity weakens the integration between different lines of research and hinders the development and implementation of practical ETW systems. For example, the research on different scales of parameters lead to different conclusions at different scales.

ii. The comparison between simulation and experimental results is not straightforward, making it difficult to reproduce and apply published models. Realistic simulations need to be experimentally verified where both the simulation and the experiments involve multiple particles.

iii. The simulation process needs to be more rigorous. The accuracy of each step of simulation process needs to be evaluated, such as calculation of electric fields and the set up of particle motion simulation models. For example, many studies keep the particle charge constant during transport. However, triboelectric charging between particles and the dielectric layer must be included.

iv. The motion of particles is affected by the combination of many different parameters. The inherent connections between the effect of these parameters on particle moving characteristics, such as the motion modes and backward motion, haven’t been revealed.

Experimental results involving multiple particles may show significant differences to single particle simulations [33]. These experimental results cannot be used to verify single particle simulation model adequately. Therefore, single particle experiment needs to be carried out to verify single particle simulations. For the verification of multiple particle simulations, the results of multiparticle simulations and experiments have only compared certain results such as general moving height [9], and require greater detail. Experiments can provide more direct and accurate information in the design and application of devices. Innovative design of experimental platforms, such as the configuration of experimental conveyors [108, 117], and additional mechanical and magnetic methods can be used to improve the performance and wider application [53, 109, 134, 137].

Recently, the ETW system has gained more attention and many simulation methods and models have been proposed [30, 31, 68]. The combination of improved theoretical calculations and laboratory experiments will help better understand the physical mechanism of how particles move and interact in the ETW field.

2.4.2 Summary

The ETW method has undergone considerable development in recent years and has emerged as an innovative method for use in particle transport and separation. To improve its performance, several research gaps have emerged from this literature review:

i. Calculation of the electric field is critical to the development of robust models for the ETW system. Accurate and fast analytical solutions are not currently embedded in existing simulations, which largely rely on Fourier expansion methods and the finite element methods.
ii. The effect of frequency on particle motion, particularly with regards to backward motion, has not yet been explained thoroughly, which may become a bottleneck in the development of ETW, or may be exploited to separate particles by size.
iii. The effect of size and shape characteristics of the particles is often overlooked.
iv. Large scale simulations of multiple particles in an ETW field has not been carried out comprehensively; this is critical to design practical systems.
v. Experimental verification of multiple particles ETW flows needs to be carried out both to validate simulations but also allow the reliable specification of system parameters.
vi. Motion modes are complex, and the transition between modes requires greater investigation.

Based on the identified gaps and development needs highlighted in the literature review, both simulation and experimental approach were performed to investigate the theory of particle motion in this research. The simulation accuracy was improved, and a more comprehensive analysis was conducted to establish stronger connections between the simulation and experimental results. This integrated approach offers clearer and more fundamental insights, guiding the design of an ETW system for particle separation.

Chapter 3 Electric Field distribution and Dielectrophoresis

A theoretical understanding of particle movement in the ETW conveyer system will allow design and operating parameter evaluations. Particles in ETW are subject to many forces, including the Coulomb force, dielectrophoretic force, gravitational force, friction, image force, and possibly fluid drag. Of these, the Coulomb and dielectrophoretic forces are predominant, and their analysis requires the accurate calculation of the electric field [35, 51]. Also, detailed and accurate knowledge of the field distribution in ETW systems is required to simulate and predict particle trajectories. The accurate prediction of the ETW electric field distribution is, therefore, essential.

In this chapter, two alternative calculation approaches are presented, the charge simulation method (CSM) and the boundary element method (BEM). The CSM and BEM have the benefit of no requirement for any approximation of the boundary conditions or the electrode shape and can accurately calculate the electric field on the electrode edges and gaps. For the improvement of calculation efficiency and simplification of coding, the method of images is introduced in the implementation of the CSM and BEM. The derived formulas can be adapted to various designs and parameters in the calculation of electrostatic potential problems.

This chapter is divided into five sections:

Section 1 concisely introduces the electric field background and the development of numerical methods. It also describes the mathematical model of ETW systems for the following calculations.

Section 2 addresses the CSM, including the introduction and derivation of basic principles. The implementation of the calculation process and accuracy evaluation of CSM results are provided in detail. A low accumulated error of the CSM is achieved by properly arranging the positions and numbers of contour points and fictitious charges.

Section 3 addresses the BEM, including the derivation of formulas and implementations. Analytical formulas are obtained for the integral of Green's function along boundary elements. The results of BEM are compared with that of CSM and FEM. The BEM can avoid the inconvenience of the arrangement of simulating charge positions required in the CSM. The numerical results show extremely close agreement between the CSM and BEM.

Section 4 analyses the electric field and DEP components. Emphasis is given to the regions close to the electrode surfaces. These results provide guidance for the design of ETW systems for various applications.

Section 5 gives the main conclusions.

3.1 Background

An ETW field can be produced by a set of electrodes, insulated from each other and connected to AC poly-phase voltage sources. Either neutral or charged fine particles brought into such a field move due to the action of electric forces, gravitational forces, and other forces related to their different physical properties. The ETW methods originates from DEP, first defined by Pohl as the interaction between non-uniform electric fields with polarized particles and liquids [18, 19]. The researchers who followed have developed a generalized theory for calculating DEP and explored its various practical applications, such as the precipitation and dispersion of liquids [138, 139]. Recently, this electrokinetic phenomenon has been applied in many diverse areas, such as xerographic particle transport in electrophotography, dust mitigation of solar panels, cell manipulation and separation in biology, and lunar particle transport and separation [12, 39, 101, 107, 140, 141].

3.1.1 Background of the Electric Potential Problem

The ETW field is generally produced by an array of parallel electrodes with the same width and thickness. Fig. 3.1 shows a diagram of a typical ETW system for particle transport and separation. A four-phase rectangular wave voltage source is often used in ETW systems [31, 38, 72], and is used here as an example in the calculations.

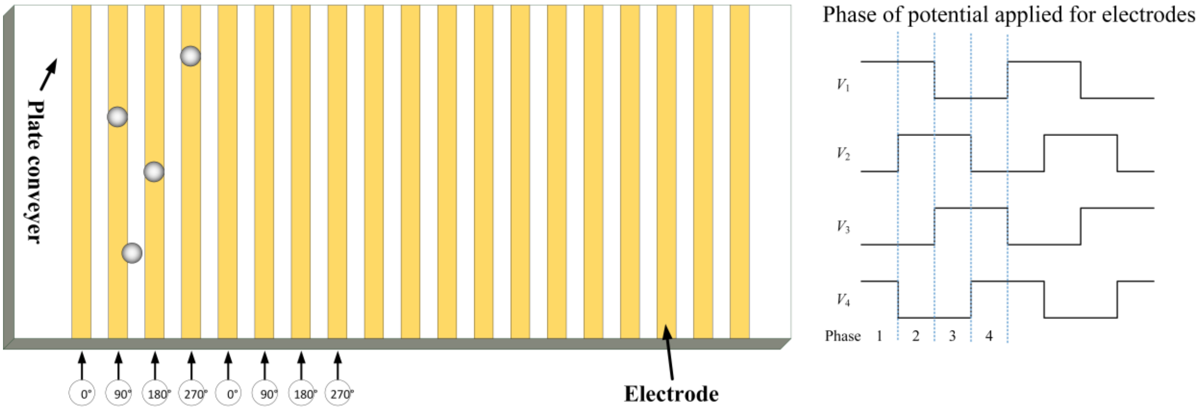

Fig. 3.1 Diagram showing the structure of typical application system and wave profile of applied voltage.

The electrode length is much larger than both the electrode width and the gap between the electrodes, and the electric field model can be simplified to a 2D problem in the $x-y$ plane, as shown in Fig. 3.2. In phases 2 and 4, Dirichlet conditions $\phi = 0$ can be designated on $x = 0$. In phases 1 and 3, the symmetry leads to the Neumann condition: $\partial\phi / \partial n = 0$. The 2D electrostatic problem can be described by Laplace's equation $\Delta\phi = 0$, associated with the boundary conditions on the electrode surfaces, which varies in time according to the system function.

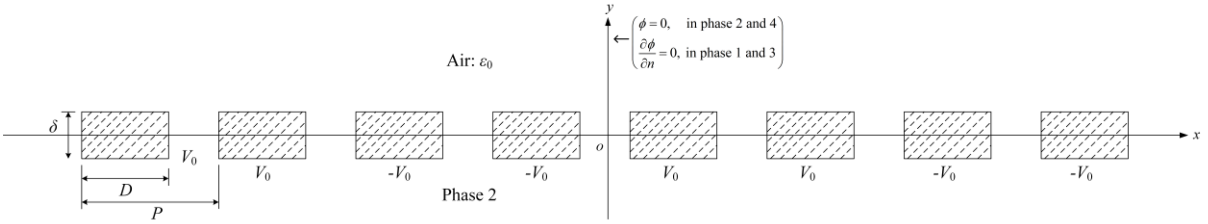

Fig. 3.2 Diagram showing the typical application system, consisting of the interdigitated electrode array. D is the electrode width, p is the electrode pitch, and δ is the electrode thickness. The voltages on the boundaries are the example at phase 2.

3.1.2 Development of Calculation Methods

Several approximate analytical and numerical methods have been proposed for the solution of the electric field produced by this particular arrangement of electrodes. In 1996, Wang and co-workers [111] used Green's theorem to calculate the electric field for 2D electrode arrays. A similar approach to the BEM, a boundary integral solution of a potential problem, has been obtained and has high computation efficiency using the Nyström method [142]. Morgan and co-workers [112, 113] developed Fourier series methods and the FEM for calculating DEP and travelling wave forces generated by interdigitated electrode arrays. Sun and co-workers [115] completed an analytical solution using the Schwarz–Christoffel mapping method without any approximation of the boundary conditions. Gauthier and co-workers [116] developed a Fourier series method to calculate DEP with two facing electrode arrays. However, in all these papers, either or both of the following two approximations have been applied: (1) the electrode boundaries are set as a line without considering the electrode shape, and (2) a linear potential variation between electrodes is assumed. These approximations deviate from reality in certain conditions and restrict the application scope of their methods.

3.2 Theory of the Charge Simulation Method

3.2.1 Basic Principle

The CSM is based on the concept of discrete charges, which has proven to be very powerful and efficient for solving many electrostatic problems [143]. Masuda and Kamimura [21] used a similar substitute charge method to calculate the electric field of parallel cylindrical electrodes.

The CSM is a numerical method for the application of the Trefftz method for the solution of the boundary value problem (BVP) in an electrostatic field where the partial differential equation is satisfied perfectly while the boundary conditions are satisfied approximately [144, 145].

The basis of the CSM is the use of a group of discrete, fictitious charges as particular solutions of Poisson's equations, where the distributed charges on the boundary are replaced by these discrete charges arranged outside the boundary. The fictitious charges are shown as the hollow circles in the first quadrant inside the boundary in Fig. 3.3, and $(x_{\mathrm{f}}^{(\mathrm{i})}, y_{\mathrm{f}}^{(\mathrm{i})})$ represents the position of the i-th fictitious charge. Using the method of images, the image fictitious charges are applied in the other three quadrants, and the positions can be easily obtained according to the symmetries. In the CSM, the solution of Laplace's equation depends on the determination of the values of these fictitious charges. The arrangement of fictitious charges and contour points is illustrated in Fig. 3.3. The contour points are on the boundary of electrodes with known potentials, which can be used in the equations to solve the unknown fictitious charges. The contour points are shown as the symbol × on the boundaries, and $(x_{\mathrm{e}}^{(\mathrm{i})}, y_{\mathrm{e}}^{(\mathrm{i})})$ represents the position of the i-th contour point. Γ_e and Γ_f represent the *e*-th and *f*-th boundaries, while Γ_e' and Γ_f' are the image boundaries, respectively. r_1, r_2, r_3, and r_4 are the distances between the contour point and the fictitious charge and image fictitious charges. d_1, s_1, s_2, and δ are simulation parameters that are used to determine the positions of contour points and fictitious charges, which can be referred to in the following calculations.

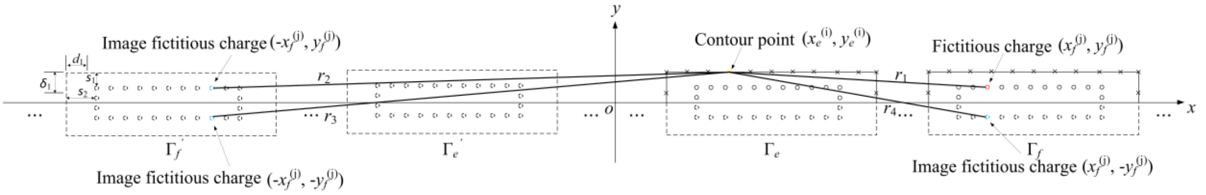

Fig. 3.3 Allocation of contour points and fictitious charges with the method of images.

The potential resulting from the superposition of discrete charges must be equal to the boundary potential ϕ_{C} on the electrode surfaces:

$$\phi_f = \sum_{e=1}^{w}\left(\sum_{i=1}^{n} P_{e,f}^{(i,j)} Q_f^{j}\right) \tag{3.1}$$

where $P_{e,f}^{(i,j)}$ is the associated potential coefficient that can be found from the fundamental solution of Poisson's equation, and it only depends on the related position between the calculating point and the *n*-th fictitious charge.

$$P_{e,f}^{(i,j)} = -\frac{1}{2\pi\varepsilon_0}\cdot\ln\sqrt{\left(x_e^{(i)} - x_f^{(j)}\right)^2 + \left(y_e^{(i)} - y_f^{(j)}\right)^2} \tag{3.2}$$

Q_f^j is the value of the *j*-th fictitious charge on the *f*-th electrode. *n* is the total number of fictitious charges in an electrode. *w* is the total number of electrodes. Since there is a unique solution to this boundary value problem, the potential can be found unambiguously from equation (3.1), where ε_0 is the permittivity of air, and $(x_e^{(i)}, y_e^{(i)})$ and $(x_f^{(j)}, y_f^{(j)})$ represent the positions of the *i*-th fictitious charge of the *e*-th electrode and the *j*-th points on the surface of the *f*-th electrodes.

The application of equations (3.1) and (3.2) leads to a system for *w* electrodes, each with *N* discrete charges:

$$\begin{bmatrix} \mathbf{P}_{11} & \mathbf{P}_{12} & \cdots & \mathbf{P}_{1w} \\ \mathbf{P}_{21} & \mathbf{P}_{22} & \cdots & \mathbf{P}_{2w} \\ \vdots & \vdots & \ddots & \vdots \\ \mathbf{P}_{w1} & \mathbf{P}_{w2} & \cdots & \mathbf{P}_{ww} \end{bmatrix} \begin{bmatrix} \mathbf{Q}_1 \\ \mathbf{Q}_2 \\ \vdots \\ \mathbf{Q}_w \end{bmatrix} = \begin{bmatrix} \boldsymbol{\phi}_1 \\ \boldsymbol{\phi}_2 \\ \vdots \\ \boldsymbol{\phi}_w \end{bmatrix} \tag{3.3}$$

where the elements of the submatrices are:

$$\mathbf{P}_{ef} = \begin{bmatrix} P_{e,f}^{(1,1)} & P_{e,f}^{(1,2)} & \cdots & P_{e,f}^{(1,N)} \\ P_{e,f}^{(2,1)} & P_{e,f}^{(2,2)} & \cdots & P_{e,f}^{(2,N)} \\ \vdots & \vdots & \ddots & \vdots \\ P_{e,f}^{(N,1)} & P_{e,f}^{(N,2)} & \cdots & P_{e,f}^{(N,N)} \end{bmatrix} \tag{3.4}$$

$$\mathbf{Q}_f = \begin{bmatrix} q_f^{(1)} & q_f^{(2)} & \cdots & q_f^{(N)} \end{bmatrix}^T \tag{3.5}$$

$$\boldsymbol{\phi}_f = \begin{bmatrix} \phi_f & \phi_f & \cdots & \phi_f \end{bmatrix}^T \tag{3.6}$$

where $q_f^{(j)}$ is the value of the fictitious charge of $(x_f^{(j)}, y_f^{(j)})$. ϕ_f is the potential of the *f*-th electrode. Equation (3.3) can be expressed in a simplified form:

$$\mathbf{PQ} = \boldsymbol{\phi} \tag{3.7}$$

where **P** is the potential coefficient matrix, **Q** is the column vector of unknown charges, and $\boldsymbol{\phi}$ is the potential of the points on the electrode boundaries.

3.2.2 Implementation of CSM

Considering the symmetry of the electrode array and the applied voltage, the method of images can be used to simplify the analysis. Based on the centre position of *o* in Fig. 3.3, the boundaries are evenly distributed in the four quadrants of the coordinate, and the fictitious charges in the first quadrant are used as the origin charges. The combination of the associated potential coefficient of the fictitious line charges and its image fictitious line charges in the other three quadrants (see Fig. 3.3) can be expressed as follows:

$$P_{e,f}^{(i,j)*}=\begin{cases}\dfrac{1}{2\pi\varepsilon_0}\ln\dfrac{r_2r_3}{r_1r_4} & \text{for phase 2 and 4}\\ \dfrac{1}{2\pi\varepsilon_0}\ln\dfrac{1}{r_1r_2r_3r_4} & \text{for phase 1 and 3}\end{cases} \tag{3.8}$$

where

$$r_1=\sqrt{\left(x_e^{(i)}-x_f^{(j)}\right)^2+\left(y_e^{(i)}-y_f^{(j)}\right)^2} \qquad (a)$$

$$r_2=\sqrt{\left(x_e^{(i)}+x_f^{(j)}\right)^2+\left(y_e^{(i)}-y_f^{(j)}\right)^2} \qquad (b)$$

$$r_3=\sqrt{\left(x_e^{(i)}+x_f^{(j)}\right)^2+\left(y_e^{(i)}+y_f^{(j)}\right)^2} \qquad (c) \qquad (3.9)$$

$$r_4=\sqrt{\left(x_e^{(i)}-x_f^{(j)}\right)^2+\left(y_e^{(i)}+y_f^{(j)}\right)^2} \qquad (d)$$

The two definitions of the associated potential coefficient in equation (3.8) are automatically satisfied with Dirichlet and Neumann conditions, respectively. Formula (3.2) is a generalized expression for each situation.

In this way, equation (3.7) can be modified as follows:

$$\begin{bmatrix}\mathbf{P}_{11}{}^{*} & \mathbf{P}_{12}{}^{*} & \cdots & \mathbf{P}_{1,w/2}{}^{*}\\ \mathbf{P}_{21}{}^{*} & \mathbf{P}_{22}{}^{*} & \cdots & \mathbf{P}_{2,w/2}{}^{*}\\ \vdots & \vdots & \ddots & \vdots\\ \mathbf{P}_{w/2,1}{}^{*} & \mathbf{P}_{w/2,2}{}^{*} & \cdots & \mathbf{P}^{*}{}_{w/2,w/2}\end{bmatrix}\begin{bmatrix}\mathbf{Q}_1\\ \mathbf{Q}_2\\ \vdots\\ \mathbf{Q}_{w/2}\end{bmatrix}=\begin{bmatrix}\boldsymbol{\phi}_1\\ \boldsymbol{\phi}_2\\ \vdots\\ \boldsymbol{\phi}_{w/2}\end{bmatrix} \tag{3.10}$$

where the submatrices are given by

$$\mathbf{P}_{ef}{}^{*}=\begin{bmatrix}P_{e,f}^{(1,1)*} & P_{e,f}^{(1,2)*} & \cdots & P_{e,f}^{(1,N/2)*}\\ P_{e,f}^{(2,1)*} & P_{e,f}^{(2,2)*} & \cdots & P_{e,f}^{(2,N/2)*}\\ \vdots & \vdots & \ddots & \vdots\\ P_{e,f}^{(N/2,1)*} & P_{e,f}^{(N/2,2)*} & \cdots & P_{e,f}^{(N/2,N/2)*}\end{bmatrix} \tag{3.11}$$

After obtaining the value of the fictitious charge in each position, the potential above the electrodes can be found with the following:

$$\phi(x,y)=\mathbf{P}^{*}(x,y)\mathbf{Q} \tag{3.12}$$

where

$$\mathbf{P}^{*}(x,y)=\left[P^{(1)*}(x,y)\quad P^{(2)*}(x,y)\quad \cdots \quad P^{(N/2)*}(x,y)\right] \tag{3.13}$$

$$\mathbf{Q} = \left[q^{(1)} \quad q^{(2)} \quad . \quad . \quad . \quad q^{(N/2)} \right]^T \tag{3.14}$$

and

$$P^{(n)*}(x,y) = \begin{cases} \dfrac{1}{2\pi\varepsilon_0} \cdot \ln \dfrac{r_2(x,y) r_3(x,y)}{r_1(x,y) r_4(x,y)} & \text{for phase 2 and 4} \\ \dfrac{1}{2\pi\varepsilon_0} \cdot \ln \dfrac{1}{r_1(x,y) r_2(x,y) r_3(x,y) r_4(x,y)} & \text{for phase 1 and 3} \end{cases} \tag{3.15}$$

where

$$\begin{aligned} r_1(x,y) &= \sqrt{\left(x - x^{(n)}\right)^2 + \left(y - y^{(n)}\right)^2} && (a) \\ r_2(x,y) &= \sqrt{\left(x + x^{(n)}\right)^2 + \left(y - y^{(n)}\right)^2} && \text{(b)} \\ r_3(x,y) &= \sqrt{\left(x + x^{(n)}\right)^2 + \left(y + y^{(n)}\right)^2} && \text{(c)} \\ r_4(x,y) &= \sqrt{\left(x - x^{(n)}\right)^2 + \left(y + y^{(n)}\right)^2} && \text{(d)} \end{aligned} \tag{3.16}$$

where n represents the n-th fictitious charge. The electric field comes from the differentiation of the potential $\phi(x,y)$ with respect to x and y:

$$E_x(x,y) = -\frac{\partial \mathbf{P}}{\partial x} \mathbf{Q} \tag{3.17}$$

and

$$E_y(x,y) = -\frac{\partial \mathbf{P}}{\partial y} \mathbf{Q} \tag{3.18}$$

3.2.3 Accuracy Evaluation

The modified standard norm error [146] is introduced for the evaluation of accuracy, which is defined by the sum of the deviation of potential at contour checkpoints, calculated from

$$Error = \sqrt{\sum_{i=1}^{m} \left[\frac{V - \phi_i(x_i, y_i)}{V} \right]^2 / m} \tag{3.19}$$

where $\phi_i(x_i, y_i)$ is the calculated potential at the i-th checkpoint, m is the total number of checkpoints, and V is the corresponding surface potential of the electrode (i.e., applied voltage on the electrode). This accuracy criterion is more rigorous than the maximum deviation previously used in [21]. The electrode configuration parameters are as previously used by Kawamoto [104]. The width of the electrode is 300 μm, the pitch is 600 μm, and the amplitude of the voltage is 800 V. The following calculations are based on the same parameters.

The accuracy of the CSM is affected by the number and placement of fictitious charges and contour points. Normally, the collocated contour points are evenly spaced along the horizontal and vertical axes with pitches of d_1 and δ_1. The distance between the fictitious charge and the boundary, vertically and horizontally, are represented by s_1 and s_2, respectively:

$$s_1 = k_1 d_1 \tag{3.20}$$

$$s_2 = k_2 \delta_1 \tag{3.21}$$

Here, k_1 and k_2 are the assignment factors deciding the position of fictitious charges. In Table 3-1, n_1 and n_2 represent D/d_1 and δ/δ_1, respectively, the numbers of contour points along the length and width of each electrode boundary. The total number of checkpoints is 250. Different combinations of n_1, n_2, k_1, and k_2 were tested to estimate the numerical calculation accuracy of the CSM. Phases 3 and 4 are symmetrical to phases 1 and 2 with different polarity, so the accumulated error are the same and only shown for phases 1 and 2 in Table 3-1. Evaluations and simulations were implemented on a personal computer with a 2.9 GHz processor and 16 GB RAM using Wolfram Mathematica. The calculation time for the CSM to obtain the error results is also presented.

Table 3-1 Standard norm error on each electrode in two different phases
with a varying number of calculating points for the CSM.

Calculating parameters	$k_1 = 1/6$ $k_2 = 1/6$	$n_1 = 200$ $n_2 = 10$	$n_1 = 150$ $n_2 = 10$	$n_1 = 100$ $n_2 = 10$	$n_1 = 100$ $n_2 = 15$	$n_1 = 100$ $n_2 = 20$
Standard norm error	Phase 1	0.03%	0.04%	0.07%	0.08%	0.12%
	Phase 2	0.02%	0.03%	0.05%	0.03%	0.09%
Computation time		11.6 s	7.6 s	3.9 s	4.1 s	4.5 s
Calculating parameters	$n_1 = 200$ $n_2 = 10$	$k_1 = 1/6$ $k_2 = 1/6$	$k_1 = 1/5$ $k_2 = 1/5$	$k_1 = 1/3$ $k_2 = 1/3$	$k_1 = 1/2$ $k_2 = 1/2$	$k_1 = 1/3$ $k_2 = 1/6$
Standard norm error	Phase 1	0.03%	0.03%	0.04%	0.06%	0.06%
	Phase 2	0.02%	0.02%	0.03%	0.05%	0.04%
Computation time		12.0 s	12.1 s	12.3 s	12.1 s	12.1 s

The small accumulated errors confirm the accuracy of the CSM. By the appropriate arrangement of n_1, n_2, k_1, and k_2, the accumulated error can be decreased to as low as 0.02%. By keeping k_1 and k_2 constant, it is found that an increase in the simulation points can improve the calculation accuracy; however, further increases may impair this, as illustrated by the last three columns. This is because overly dense points may lead to an ill-conditioned matrix and a decrease in the solution accuracy. The test results with different combinations of k_1 and k_2 show that a reasonable arrangement of k_1 and k_2 can increase the accuracy of the CSM further.

3.3 Theory of the Boundary Element Method

3.3.1 Formulation

In the CSM, it may be challenging to arrange the positions of the fictitious charges properly, which affects the accuracy of the results. In contrast, the BEM does not rely upon fictitious charges, and only boundary discretization is required. Fig. 3.4 illustrates the basic parameters for deploying the BEM. P and P_i are integration and observation points, respectively. Γ_l^* is the electrode surface in the first quadrant of the coordinate system. r_1, r_2, r_3, and r_4 are the distances between the integration point and the observation points and image fictitious charges. Using Green's second identity with the appropriate fundamental solution, a boundary integral equation can be found as follows [147]:

$$c_i u(P_i) = \int_{\Gamma} \frac{\partial u(P)}{\partial n} G(P,P_i)\, d\Gamma - \int_{\Gamma} \frac{\partial G(P,P_i)}{\partial n} u(P)\, d\Gamma \tag{3.22}$$

where $u(P)$ is the solution of $\nabla^2 u = 0$ for $P \in \Omega$. And

$$c_i = \begin{cases} 1 & \text{for } P \text{ inside the region } \Omega \\ 1/2 & \text{for } P \text{ on the smooth boundary } \Gamma \\ 0 & \text{for } P \text{ outside the region } \Omega \end{cases} \tag{3.23}$$

and

$$G(P,P_i) = \frac{1}{2\pi} \ln \frac{1}{r_1} \tag{3.24}$$

Equation (3.24) is the fundamental solution, where r_1 is the distance between points P and P_i. Denoting the boundary of the electrodes as Γ_1, Γ_2, ..., Γ_w, it can be deduced from equation (3.22) that

$$c_i u(P_i) = \sum_{l=1}^{w} \int_{\Gamma_l} \frac{\partial u(P)}{\partial n} G(P,P_i)\, d\Gamma - \sum_{l=1}^{w} \int_{\Gamma_l} \frac{\partial G(P,P_i)}{\partial n} u(P)\, d\Gamma \tag{3.25}$$

On account of the relation in [148],

$$\int_{\Gamma_l} \frac{\partial G(P,P_i)}{\partial n} d\Gamma = (1 - c_i)\delta_{kl}, \quad \text{for } P_i, P \text{ on the boundary } \Gamma_k, \Gamma_l, \text{resp.} \tag{3.26}$$

where δ_{kl} is the Kronecker delta, and noting that $u(P) = u_l$ (constant) on the boundary Γ_l, it follows that

$$\sum_{l=1}^{w} \int_{\Gamma_l} u(P) \frac{\partial G(P,P_i)}{\partial n} d\Gamma = \sum_{l=1}^{w} u_l (1-c_i)\delta_{kl} = (1-c_i)u_k \tag{3.27}$$

Using equations (3.23) and (3.25), this can be transformed into

$$u_k = \sum_{l=1}^{w} \int_{\Gamma_l} \frac{\partial u}{\partial n} G(P,P_i) d\Gamma \tag{3.28}$$

In addition, G in equation (3.28) can be replaced with a modified fundamental solution G_s, that is,

$$G_s(P,P_i) = \begin{cases} \dfrac{1}{2\pi} \ln \dfrac{r_2 r_3}{r_1 r_4} & \text{for phase 2 and 4} \\ \dfrac{1}{2\pi} \ln \dfrac{1}{r_1 r_2 r_3 r_4} & \text{for phase 1 and 3} \end{cases} \tag{3.29}$$

where

$$\begin{aligned} r_1 &= \sqrt{(x-x_i)^2 + (y-y_i)^2} && (a) \\ r_2 &= \sqrt{(x+x_i)^2 + (y-y_i)^2} && \text{(b)} \\ r_3 &= \sqrt{(x+x_i)^2 + (y+y_i)^2} && \text{(c)} \\ r_4 &= \sqrt{(x-x_i)^2 + (y+y_i)^2} && \text{(d)} \end{aligned} \tag{3.30}$$

Equation (3.30) (*a* to d) can be interpreted by the method of images, as shown in Fig. 3.4. As a consequence, equation (3.28) can be simplified to

$$u_k = \sum_{l=1}^{w/2} \int_{\Gamma_l^*} \frac{\partial u}{\partial n} G_s(P,P_i) d\Gamma \tag{3.31}$$

Equation (3.31) reduces the unknowns, remarkably, to 25% of those in the original equation (3.28).

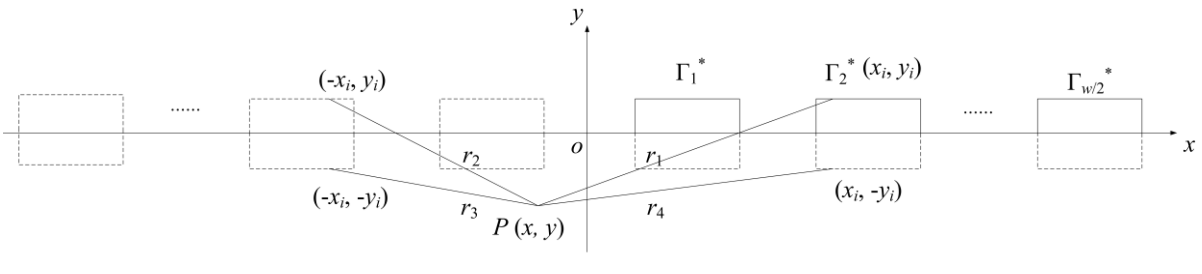

Fig. 3.4 Electrode geometry for the BEM with the method of images.

The discretization of (3.31) yields

$$u_k^{(i)} = \sum_{l=1}^{w/2} \sum_{j=1}^{N} \int_{\Gamma_{l,j}^*} \frac{\partial u(P)}{\partial n} G_s\left(P, P_i\right) d\Gamma = \sum_{l=1}^{w} \sum_{j=1}^{N} \left(\frac{\partial u}{\partial n}\right)_l^{(j)} G_{k,l}^{(i,j)} \tag{3.32}$$

where

$$G_{k,l}^{(i,j)} = \begin{cases} \dfrac{1}{2\pi} \displaystyle\int_{\Gamma_{l,j}^*} \ln \frac{r_2 r_3}{r_1 r_4} d\Gamma & \text{for phase 2 and 4} \\ \dfrac{1}{2\pi} \displaystyle\int_{\Gamma_{l,j}^*} \ln \frac{1}{r_1 r_2 r_3 r_4} d\Gamma & \text{for phase 1 and 3} \end{cases} \tag{3.33}$$

$\left(\frac{\partial u}{\partial n}\right)_l^{(j)}$ is assumed to be constant in each boundary element and needs to be solved. Accordingly, a linear equation system can be established with Equations (3.31) and (3.32):

$$\begin{bmatrix} \mathbf{G}_{11} & \mathbf{G}_{12} & \cdot & \cdot & \mathbf{G}_{1,w/2} \\ \mathbf{G}_{21} & \mathbf{G}_{22} & \cdot & \cdot & \mathbf{G}_{2,w/2} \\ \cdot & \cdot & \cdot & \cdot & \cdot \\ \cdot & \cdot & \cdot & \cdot & \cdot \\ \cdot & \cdot & \cdot & \cdot & \cdot \\ \mathbf{G}_{w/2,1} & \mathbf{G}_{w/2,2} & \cdot & \cdot & \mathbf{G}_{w/2,w/2} \end{bmatrix} \begin{bmatrix} \mathbf{u}_n^{(1)} \\ \mathbf{u}_n^{(2)} \\ \cdot \\ \cdot \\ \cdot \\ \mathbf{u}_n^{(w/2)} \end{bmatrix} = \begin{bmatrix} \mathbf{s}_1 \\ \mathbf{s}_2 \\ \cdot \\ \cdot \\ \cdot \\ \mathbf{s}_{w/2} \end{bmatrix} \tag{3.34}$$

Where

$$\mathbf{G}_{kl} = \begin{bmatrix} G_{k,l}^{(1,1)} & G_{k,l}^{(1,2)} & \cdot & \cdot & G_{k,l}^{(1,N)} \\ G_{k,l}^{(2,1)} & G_{k,l}^{(2,2)} & \cdot & \cdot & G_{k,l}^{(2,N)} \\ \cdot & \cdot & \cdot & \cdot & \cdot \\ \cdot & \cdot & \cdot & \cdot & \cdot \\ \cdot & \cdot & \cdot & \cdot & \cdot \\ G_{k,l}^{(N,1)} & G_{k,l}^{(N,2)} & \cdot & \cdot & G_{k,l}^{(N,N)} \end{bmatrix} \tag{3.35}$$

$$\mathbf{u}_n^{(l)} = \left[\left(\frac{\partial u}{\partial n}\right)_l^{(1)} \quad \left(\frac{\partial u}{\partial n}\right)_l^{(2)} \quad \cdot \ \cdot \ \cdot \quad \left(\frac{\partial u}{\partial n}\right)_l^{(N)} \right]^T \tag{3.36}$$

$$\mathbf{s}_l = \left[u_l \quad u_l \quad \cdot \ \cdot \ \cdot \quad u_l\right]^T \tag{3.37}$$

Equation (3.34) can be written more concisely as follows:

$$\mathbf{GU}_n = \mathbf{S} \tag{3.38}$$

where **U**$_n$ is the solution vector representing the normal derivative of the potential on the electrode surfaces.

Using the obtained normal derivative $\partial u/\partial n$ on the electrode surfaces, the potential of P in the region Ω can be found by equation (3.25) with $c_i = 1$:

$$u(P_i)=\sum_{l=1}^{w}\int_{\Gamma_l}\frac{\partial u(P)}{\partial n}G(P,P_i)d\Gamma-\sum_{l=1}^{w}\int_{\Gamma_l}\frac{\partial G(P,P_i)}{\partial n}u(P)d\Gamma \tag{3.39}$$

The second term on the RHS of equation (3.39) vanishes due to $u(P) = u_l$ on Γ_l and

$$\int_{\Gamma_l}\frac{\partial G(P,P_i)}{\partial n}d\Gamma=0,\quad \text{for } P_i \text{ inside the region } \Omega \text{ and } P \text{ on the boundary } \Gamma_l \tag{3.40}$$

Consequently, equation (3.39) can be reduced to

$$u(P_i)=\sum_{l=1}^{w}\int_{\Gamma_l}\frac{\partial u(P)}{\partial n}G(P,P_i)d\Gamma \tag{3.41}$$

Equation (3.41) can be simplified further by replacing G with G_s as follows:

$$u(P_i)=\sum_{l=1}^{w/2}\int_{\Gamma_l^*}\frac{\partial u(P)}{\partial n}G_s(P,P_i)d\Gamma \tag{3.42}$$

Discretization of equation (3.42) gives the following:

$$u(P_i)=\mathbf{G}_K\mathbf{U}_n \tag{3.43}$$

where

$$\mathbf{G}_K=\left[\mathbf{G}_1,\mathbf{G}_2,\ldots,\mathbf{G}_{w/2}\right],\mathbf{G}_l=\left[G_l^{(1)},G_l^{(2)},\ldots,G_l^{(N)}\right] \\ l=1,2,\ldots,w/2 \tag{3.44}$$

with

$$G_l^{(j)}=\begin{cases}\dfrac{1}{2\pi}\displaystyle\int_{\Gamma_{l,j}^*}\ln\frac{r_2r_3}{r_1r_4}d\Gamma, & \text{for Phase 2 and 4}\\ \dfrac{1}{2\pi}\displaystyle\int_{\Gamma_{l,j}^*}\ln\frac{1}{r_1r_2r_3r_4}d\Gamma, & \text{for Phase 1 and 3}\end{cases}\qquad j=1,2,\ldots,N \tag{3.45}$$

and

$$\mathbf{U}_n=\left[\mathbf{u}_n^{(1)},\mathbf{u}_n^{(2)},\ldots,\mathbf{u}_n^{(w/2)}\right]^{\mathrm{T}} \tag{3.46}$$

Therefore, the x, y components of $\boldsymbol{E}$ can be calculated as follows:

$$E_x(P_i) = -\frac{\partial \mathbf{G}_K}{\partial x_i}\mathbf{U}_n \tag{3.47}$$

and

$$E_y(P_i) = -\frac{\partial \mathbf{G}_K}{\partial y_i}\mathbf{U}_n \tag{3.48}$$

The computation efficiency can be improved further by solving the integrals (3.33) analytically with the approach given in [149]. However, more convenient results can be obtained for the evaluation of the integrals. An illustration of the integral model is shown in Fig. 3.5. Parameter s is the arclength of a linear segment, and the integral point P (x, y) moves along the linear segment. (x_0, y_0) is the coordinate of the segment midpoint, and (x_i, y_i) is the coordinate of the observation point.

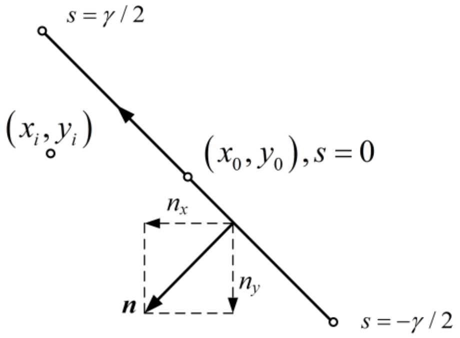

Fig. 3.5 Arclength parameters for the element integration.

The position of P (x, y) can be denoted by

$$x = x_0 + \beta s\,,\ \ y = y_0 + \delta s \tag{3.49}$$

where $\beta = n_y$, $\delta = -n_x$. It is worth mentioning that the normal vector always points to the left as s increases, and $\beta^2 + \delta^2 = 1$. The integral of (3.33) can be expanded as the sum form of four integrals related to r_1, r_2, r_3, and r_4, respectively. By this notation, each of the integrals relevant to (3.33) can be written as

$$\frac{1}{2\pi}\int_{\Gamma} \ln\frac{1}{|P_i - P|}d\Gamma = \frac{1}{2\pi}\int_{-\gamma/2}^{\gamma/2} \ln\frac{1}{\sqrt{(x_0+\beta s - x_i)^2 + (y_0 + \delta s - y_i)^2}}ds \tag{3.50}$$

where γ is the length of the element. Moreover, by the substitution

$$s = t - \kappa\,,\quad \kappa = \beta(x_0 - x_i) + \delta(y_0 - y_i) \tag{3.51}$$

The integral of (3.50) is equivalent to

$$\begin{aligned}
&\frac{1}{2\pi}\int_{-\gamma/2}^{\gamma/2}\ln\frac{1}{\sqrt{\left(x_0+\beta s-x_i\right)^2+\left(y_0+\delta s-y_i\right)^2}}ds=-\frac{1}{4\pi}\int_{\kappa-\gamma/2}^{\kappa+\gamma/2}\ln\left(t^2+u^2\right)dt\\
&=-\frac{1}{4\pi}\left[t\ln\left(t^2+u^2\right)-2t+2u\arctan\left(t/u\right)\right]_{t=\kappa-\gamma/2}^{t=\kappa+\gamma/2}\\
&=-\frac{1}{4\pi}\left\{\begin{array}{l}\kappa\ln\dfrac{\left(\kappa+\gamma/2\right)^2+u^2}{\left(\kappa-\gamma/2\right)^2+u^2}+\dfrac{\gamma}{2}\ln\left\{\left[\left(\kappa+\gamma/2\right)^2+u^2\right]\left[\left(\kappa-\gamma/2\right)^2+u^2\right]\right\}\\
-2\gamma+2u\left(\arctan\dfrac{\kappa+\gamma/2}{u}-\arctan\dfrac{\kappa-\gamma/2}{u}\right)\end{array}\right\}
\end{aligned}\qquad(3.52)$$

where

$$u=\delta\left(x_0-x_i\right)-\beta\left(y_0-y_i\right)\qquad(3.53)$$

Equation (3.52) is valid for $u\neq 0$. When $u = 0$, the following result can be employed:

$$\begin{aligned}
&\frac{1}{2\pi}\int_{-\gamma/2}^{\gamma/2}\ln\frac{1}{\sqrt{\left(x_0+\beta s-x_i\right)^2+\left(y_0+\delta s-y_i\right)^2}}ds=-\frac{1}{2\pi}\left[t\ln|t|-t\right]_{t=\kappa-\gamma/2}^{t=\kappa+\gamma/2}\\
&=-\frac{1}{2\pi}\left[\kappa\ln\left|\frac{\kappa+\gamma/2}{\kappa-\gamma/2}\right|+\frac{\gamma}{2}\ln\left|\kappa^2-\gamma^2/4\right|-\gamma\right]
\end{aligned}\qquad(3.54)$$

when $P_0(x_0, y_0)$ and $P_i(x_i, y_i)$ coincide, it gives $\kappa = u = 0$, and the corresponding singular integral can be obtained easily using equation (3.54):

$$\frac{1}{2\pi}\int_{-\gamma/2}^{\gamma/2}\ln\frac{1}{\sqrt{\left(x_0+\beta s-x_i\right)^2+\left(y_0+\delta s-y_i\right)^2}}ds=\frac{\gamma}{2\pi}\left(1-\ln\frac{\gamma}{2}\right)\qquad(3.55)$$

Thus, the integrals of (3.33) can be found by proper linear combinations of the analytical solutions (3.52), (3.54) or (3.55). By this approach, no numerical quadrature is required, and the BEM algorithm can be implemented with very high efficiency.

3.3.2 Comparison of CSM, BEM, and FEM

The two above-mentioned approaches were used to calculate the electric field. Fig. 3.6 and Fig. 3.7 show the electric field at the height of 50 μm above an electrode surface with 8 and 16 electrodes, respectively. Clearly, the BEM and CSM produce highly consistent results, which confirms their validity. The code for the BEM can be found from the supplementary material in the appendix B.

In order to quantify the comparison for the accuracy of the CSM and BEM, the same process for calculating the error for the BEM was applied, and the results are shown in Table 3-2. n_1 and n_2 are the numbers on each long side and short side of boundary elements. It is clear that the CSM has slightly higher accuracy than the BEM. The CSM only needs 4.5 s to achieve the accuracy of 0.12% at phase, while the BEM needs 12 s. However, the CSM needs time to set up the positions of fictitious charges manually, which might be time-consuming for complex boundary conditions. The BEM does not need pre-processing, and the image method reduces unknown elements to 25% of those in the original equations, which greatly improves the computation efficiency of the BEM.

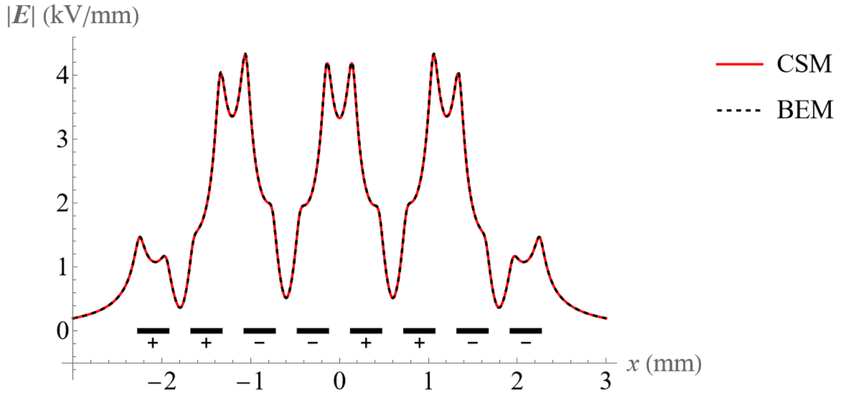

Fig. 3.6 Comparison of the electric field at the height of 50 μm above the 8 electrodes using the CSM and BEM.

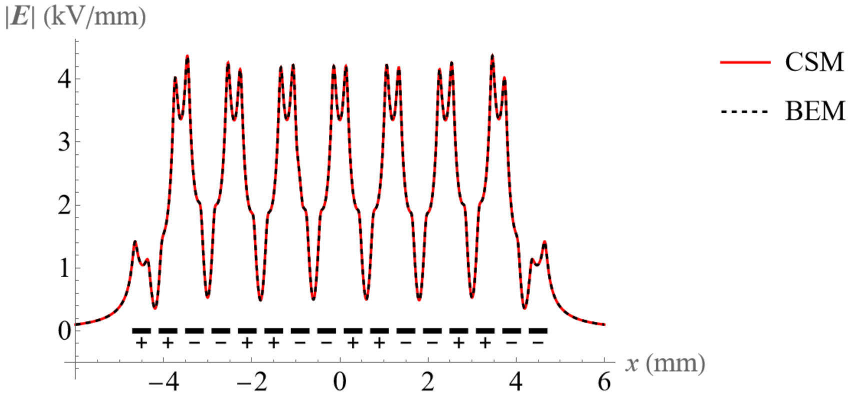

Fig. 3.7 Comparison of the electric field at the height of 50 μm above the 16 electrodes using the CSM and BEM.

Table 3-2 Standard norm error on each electrode in two different phases with a varying number of calculating points for the BEM.

Calculating parameters	Phase	$n_1 = 200$ $n_2 = 10$	$n_1 = 150$ $n_2 = 10$	$n_1 = 100$ $n_2 = 10$	$n_1 = 100$ $n_2 = 15$	$n_1 = 100$ $n_2 = 20$
Accumulated error	1	0.13%	0.16%	0.19%	0.19%	0.18%
	2	0.10%	0.12%	0.15%	0.14%	0.13%
Calculation time		12.0 s	8.1 s	4.9 s	5.3 s	5.4 s

The FEM is frequently used to solve electrostatic problems [33, 43]. The accuracy of the FEM is related closely to the quality of the calculating mesh used; at the edge of conductors, extremely fine meshing is required, while further away from electrodes, it can be coarser [59]. The area in the eight-electrode model was divided into two areas (blue and grey) by the rectangular boundary around the electrodes, as shown in Fig. 3.8. A triangular mesh was applied. The element size outside the rectangular area is set as extremely fine, while the mesh size is set to be smaller than 4×10^{-6} m inside the rectangular area.

Comparisons between the electric field obtained by the CSM, BEM, and FEM for 8 and 16 electrodes are shown in Fig. 3.9 and Fig. 3.10. All methods are in good agreement in the central electrode region. However, the FEM results show significant deviation from the CSM and BEM on both sides, especially at the corners of the electrodes. In addition, the FEM has a large deviation from the CSM and BEM in the area of the shear distribution of the electric field. It is clear that the CSM and BEM have higher accuracy than the FEM in solving this BVP. In addition, mesh generating is time-consuming with the FEM, and the impact of the increase in electrode number is more severe.

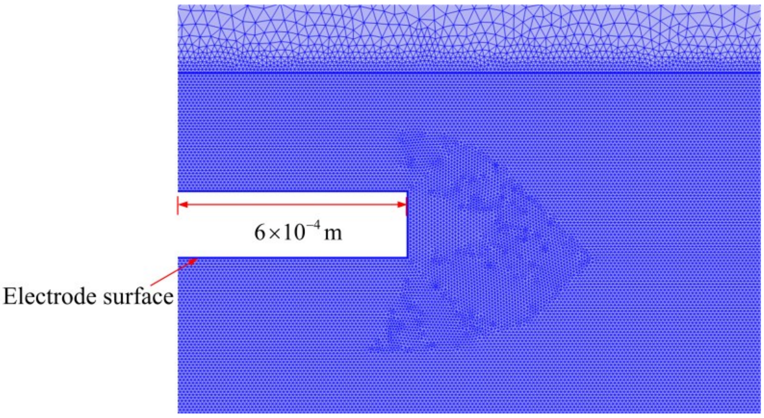

Fig. 3.8 Subdivision area illustration of part of the electrode and area close to the surface in COMSOL.

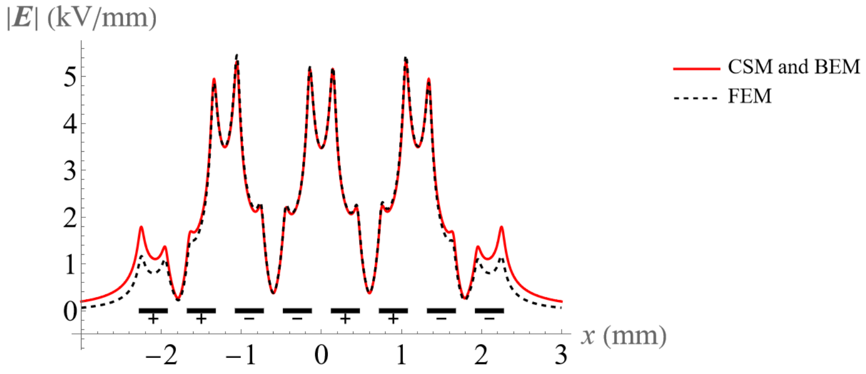

Fig. 3.9 Comparison of the electric field at the height of 32 μm above the 8 electrodes using the CSM, BEM, and FEM.

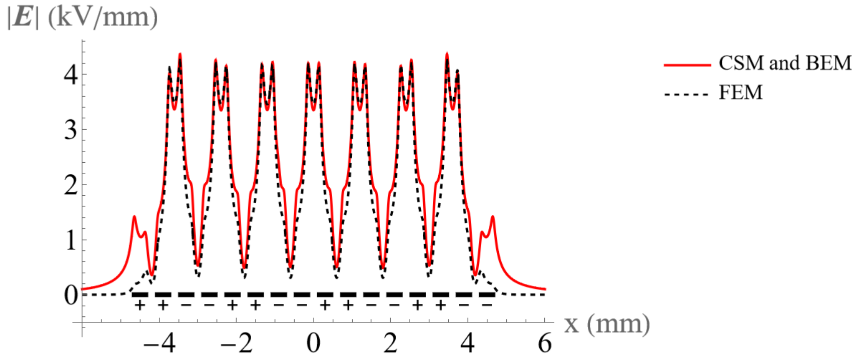

Fig. 3.10 Comparison of the electric field at the height of 50 μm above the 16 electrodes using the CSM, BEM, and FEM.

3.4 Electric Field and Dielectrophoretic Component Analysis

3.4.1 Distribution of Potential and Electric Field

The distribution of potential and electric field direction above eight electrodes in phases 1 and 2 are shown as contour lines and arrows in Fig. 3.11 (a) and (b), from the BEM. The black bars on the bottom of the two figures signify each of the eight electrodes. The field line directions can be used to predict the particle motion when the Coulomb force dominates.

The electric field components E_x and E_y of eight electrodes in phase 2 are calculated and shown in Fig. 3.12 and Fig. 3.13, which accurately include the edge effect on the end of electrode arrays. For the field of a large number of parallel electrodes, the periodic symmetry of the field allows the extension of the solution with the same phase relationship by simply repeating the periodic solution (in the middle range of the calculated field) in the positive and negative *x*-directions.

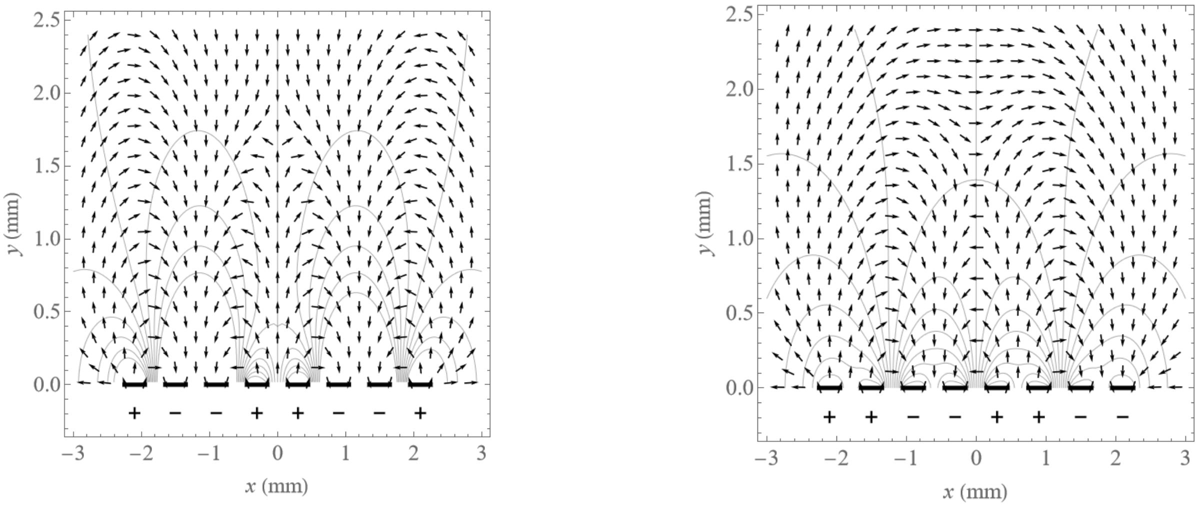

(a) Phase 1

(b) Phase 2

Fig. 3.11 Contour plot of potential and vector plot of electric field above eight electrodes at different phases.

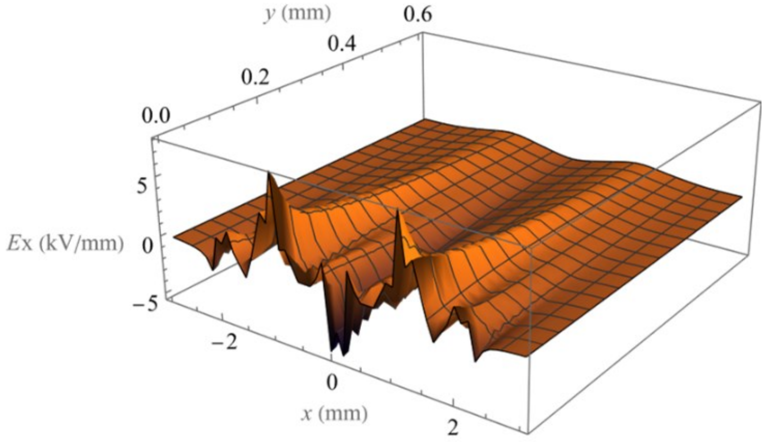

Fig. 3.12 Spatial distribution of the magnitude of field component Ex.

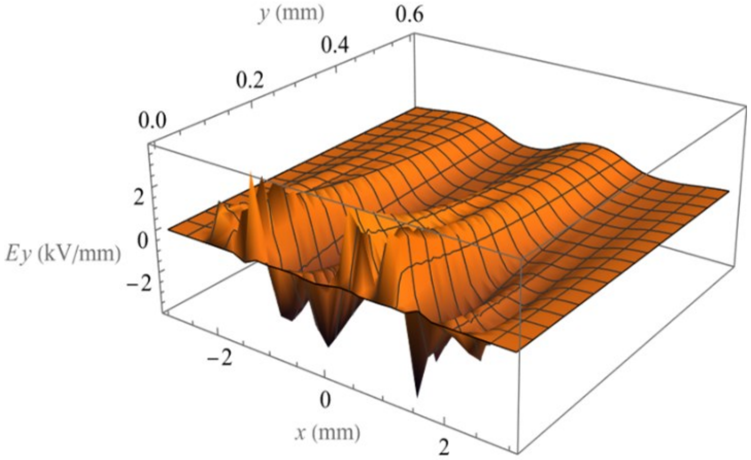

Fig. 3.13 Spatial distribution of the magnitude of field component Ey.

3.4.2 Electric Fields with Different Electrode Thickness

The electric field is evaluated at heights of 50 μm, 500 μm, and 1mm above the surface of the conveyor with different electrode thickness.

Fig. 3.14 (*a*) and (b) compares the electric field magnitude with electrode thicknesses of 18 μm and 180 μm while maintaining the other model parameters the same. At the height of 50 μm, the maximum value of the electric fields is similar. However, Fig. 3.14 (b) shows that electrodes with larger thickness have higher electric field and that the difference is more distinct at higher altitudes. The effect of electrode thickness on the electric field is instructive for the design of ETW system electrode configurations.

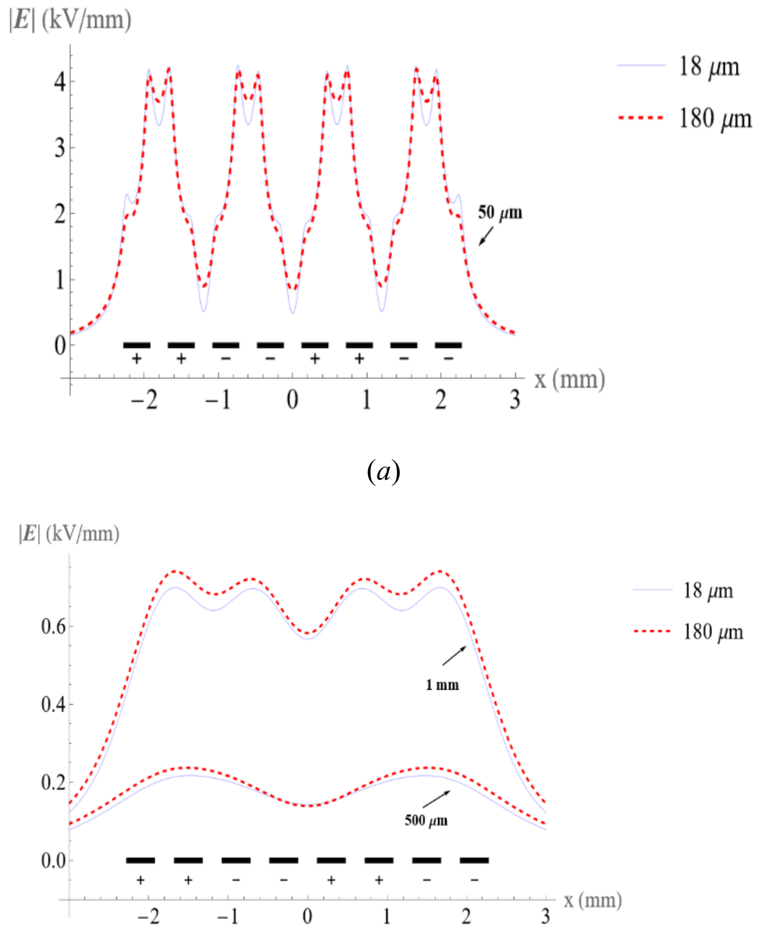

(*a*)

(b)

Fig. 3.14 Comparison of the electric field distribution with 18 μm and 180 μm electrode thicknesses (*a*) at the height of 50 μm above the surface of the conveyor and (b) at the height of 500 μm and 1 mm above the surface of the conveyor.

3.4.3 Dielectrophoretic Component Analysis

The dielectrophoretic force has received increasing attention in particles or biological cell separation [150] and carbon nanotube manipulation [151]. The DEP acts on particles that are polarizable in a non-uniform electric field. The time-averaged force on the particle can be calculated as follows [113]:

$$\langle F_{dep} \rangle = \frac{1}{4} v \operatorname{Re}\left[\alpha \nabla \left(\boldsymbol{E} \cdot \boldsymbol{E}^{*}\right)\right] - \frac{1}{2} v \operatorname{Re}\left[\alpha \nabla \times \left(\boldsymbol{E} \times \boldsymbol{E}^{*}\right)\right] \tag{3.56}$$

where $\boldsymbol{E}$ is a general complex amplitude of the electric field, * indicates a complex conjugate, v is the volume of the particle, and α is the effective polarizability related to particle and dielectric permittivity. In this case, the electric field is constant and calculated independently in each phase, so there is no phase variation, and the second term on the right side of equation in (3.56) is zero. Fig. 3.15 shows the DEP potential $\left(\boldsymbol{E}\cdot\boldsymbol{E}^*\right)$ as contour lines and vector direction $\langle F_{\mathrm{dep}}\rangle$ as arrows.

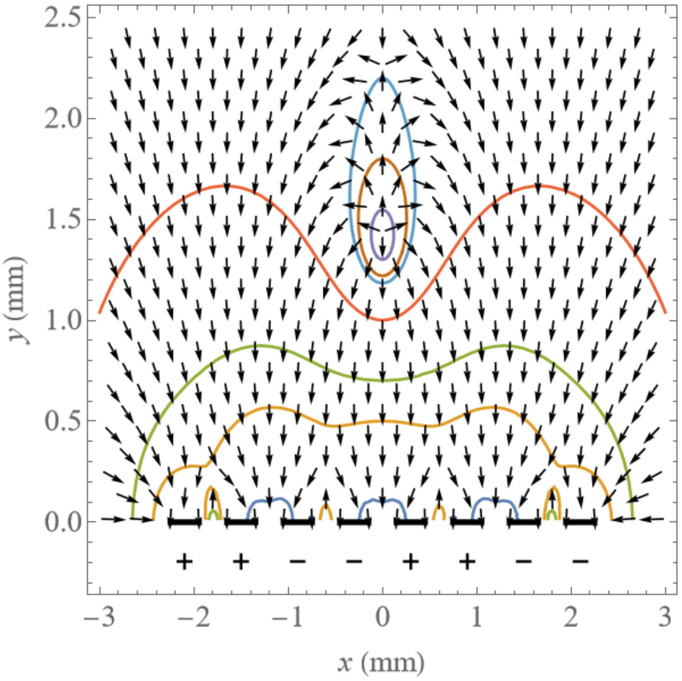

Fig. 3.15 Contour plot of DEP potential and vector plot of DEP above electrodes in phase 2.

3.5 Conclusions

The CSM and BEM were explored for the numerical solution of the electric field for an interdigitated, rectangular electrode array with a specified thickness. These two methods are readily implemented with the method of images and can achieve high computational efficiency and accuracy. In addition, analytical solutions for the integral of Green's function along the boundary elements were derived. These analytical formulas are beneficial to the efficient implementation of the BEM and can be utilized for the general 2D BEM of electrostatic problems.

The boundary conditions used in the CSM and BEM numerical calculation do not require simplification. Electric field and DEP component analysis with 8- and 16-electrode systems were provided, which showed accurate results near the electrode surface. These results can be used for the design of different ETW electrode configurations for particle transport and biological cell manipulations. The FEM results were compared with those of the CSM and BEM and showed differences at the electrode ends, indicating that the FEM may not be suitable for determining the electric field in systems with sharp boundaries. Moreover, the CSM and BEM are less time-consuming. Overall, the CSM and BEM are more general numerical methods for dealing with electrostatic field problems and can be adapted readily to more complex boundary conditions, such as a 3D model of the electrode array.

This accurate evaluation of the electric field could potentially benefit the analysis of particles and cells in transport and separation, as the estimation of particle trajectory is highly sensitive to the electric field.

Chapter 4 Numerical Modelling and Theory of Single Particle Movement

4.1 Introduction

This chapter analyses the motion of small particles in an ETW field with the aim of exploiting differences in motion direction and velocity to separate particles by size. Single particle simulation can qualitatively evaluate the effect of forces and operating parameters on the particle motion. The analysis for the results of single particle simulation give a more detailed view of how particles will act in the field. The conclusions of how the operating parameters affect the motion of particles as a function of size can improve the understanding of the motions of multiple particles and applications involving separation by size. For example, the critical frequency that induces particles to move in different directions found from single particle simulation can guide the design of particle separation systems.

This chapter is divided into four sections:

Section 1 introduces the requirements of the single particle simulation and establishes the approach to achieve those requirements.

Section 2 introduces the simulation methods. The net force on single particle is described in detail. The formulas for calculating the electrostatic fields are derived by using the Fourier expansion method including the accurate boundary conditions near the surface of the electrodes based on the results from chapter 3. The basis of the selected particle compositions and size ranges was explained and how the reasonable values for the particle charge were derived.

Section 3 shows and analyses the simulation results. The combination effect of different parameters, such as particle size, charge, and frequency on particle moving velocity and levitation height have been evaluated.

Section 4 is the summary of this chapter.

4.2 Simulation Model

4.2.1 Force Analysis

A three-phase potential is applied to the assumed infinite parallel electrodes series inserted into the substrate and the diagram is shown in Fig. 4.1. *d* is the width of electrode and *p* is the pitch.

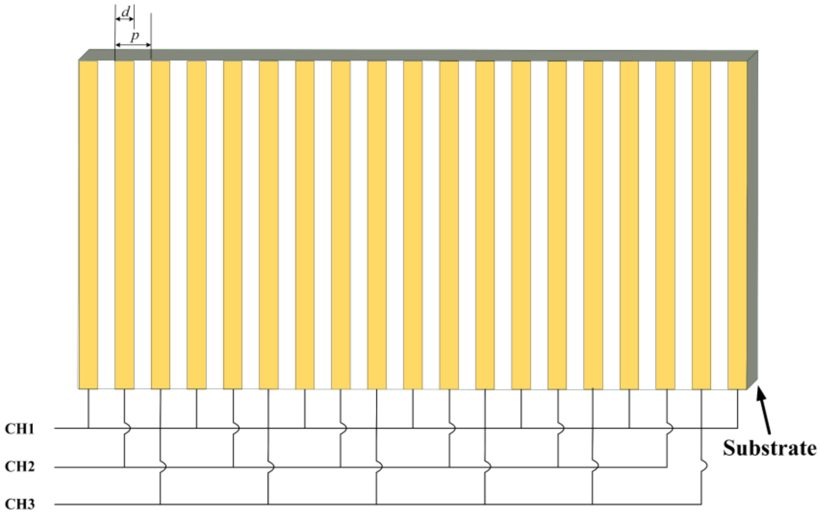

Fig. 4.1 Design of simulation model showing the configurations of electrodes with the input of three channels of volage.

The length of the electrodes is much larger than the width and pitch, so the electric field is assumed to be uniform in the length direction. As the system generates high electric fields up to $2\times10^{\wedge 6}$ V/m with 1 kV on the electrodes [59] and the saturation of 100 µm ballotini particle (density is $2.5\times10^{\wedge 3}$ kg/m$^{\wedge 3}$) is about $1.6\times10^{\wedge -12}$ C based on the relation of Pauthenier [152], the Coulomb force ($\boldsymbol{F}_{\mathrm{C}}$) on the particle will be larger than the gravitational force ($\boldsymbol{F}_{\mathrm{G}}$), which is about $1.28\times10^{\wedge -8}$ N. Therefore, the Coulomb force ($\boldsymbol{F}_{\mathrm{C}}$) will be the dominant force that drives and levitates particles. The dielectrophoretic force ($\boldsymbol{F}_{\mathrm{DEP}}$) will affect polar particles in high electric fields. If a particle is close to the electrode surface, the image force may also have an effect. Because the field is electrostatic, the magnetic force is neglected. There will be also friction ($\boldsymbol{F}_{\mathrm{f}}$) and van der Waals force ($\boldsymbol{F}_{\mathrm{vdW}}$) when the particle is on or very close to the surface. In all, the net force on a single particle in two dimensions (2D) is shown in Fig. 4.2.

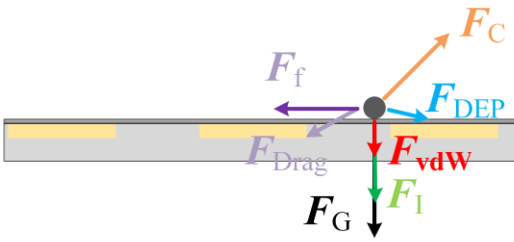

Fig. 4.2 Net force on a single charged particle in an ETW field.

In an electric field $\boldsymbol{E}$, the Coulomb force can be calculated as follows:

$$\boldsymbol{F}_C = \boldsymbol{E}\cdot q \qquad (4.1)$$

where q is the total charge of particle.

The n^{th} multipolar dielectrophoretic force in a 2D field in the *x-y* Cartesian coordinate system can be calculated as [153]:

$$\boldsymbol{F}_{DEP}^{(\mathrm{n})} = -\frac{4\pi \mathrm{n}\varepsilon_m K_\mathrm{n} r^{2n+1}}{(2n-1)!!} \sum_{p+q=\mathrm{n}} \frac{1}{p!q!}\left[\frac{\partial^\mathrm{n}\phi}{\partial x^p \partial y^q}\frac{\partial^\mathrm{n}\boldsymbol{E}}{\partial x^p \partial y^q}\right] \tag{4.2}$$

where ε_m is the dielectric permittivity of the medium, r is the radius of particle, ϕ is the potential of electric field and the factors K_n represent generalized polarization coefficients, of which K_1 is the Clausius-Mossotti factor.

The calculation of K_n can be obtained by:

$$K_\mathrm{n}(\omega) = \frac{\varepsilon_p^*(\omega) - \varepsilon_m^*(\omega)}{\mathrm{n}\varepsilon_p^*(\omega) + (\mathrm{n}+1)\varepsilon_m^*(\omega)} \tag{4.3}$$

where ε_p^* and ε_m^* are the complex dielectric permittivity of particle and medium, which are related to angular frequency (ω) of the electric field. The complex permittivity is given as:

$$\varepsilon^* = \varepsilon - i\sigma / \omega \tag{4.4}$$

where σ is conductivity, and $i^2 = -1$. For a homogeneous spherical particle, a polarized dipole was assumed and only the first order DEP was used in the simulation model. The first order of dielectrophoretic force is expressed as the combination of standing dielectrophoresis and travelling dielectrophoresis [154]:

$$\boldsymbol{F}_{DEP} = 2\pi\varepsilon_m r^3 \,\mathrm{Re}[K_1]\nabla E_{rms}^2 + 4\pi\varepsilon_m r^3 \,\mathrm{Im}[K_1]\left(E_{rms,x}^2 \nabla\varphi_x + E_{rms,y}^2 \nabla\varphi_y\right) \tag{4.5}$$

where E_{rms} is the amplitude of electric field.

However, if the size of the particle is comparable to the electrode features, higher order of dielectrophoretic force should be considered.

The gravitational force ($\boldsymbol{F}_\mathrm{G}$), friction force ($\boldsymbol{F}_\mathrm{f}$), image force ($\boldsymbol{F}_\mathrm{I}$) and air drag force ($\boldsymbol{F}_\mathrm{Drag}$) are calculated using these formulas, respectively:

$$\boldsymbol{F}_G = -\frac{4}{3}\rho\pi r^3 \boldsymbol{n} \tag{4.6}$$

where ρ is the density of particle and $\boldsymbol{n}$ represents upward normal vector perpendicular to the surface.

Friction force is calculated by the product of pressure and friction coefficient:

$$\boldsymbol{F}_f = -\mu F_{total,y} \boldsymbol{n}_T \tag{4.7}$$

where μ is friction coefficient and is approximated as 0.25 based on the experiment [155]. $F_{total,y}$ represents the net force in vertical direction. $\boldsymbol{n}_T$ represents normal vector perpendicular to $\boldsymbol{n}$ and the direction is the same as the particle motion direction. $\boldsymbol{F}_\mathrm{f}$ only appears when particle slides along the surface.

Van der Waals force is calculated based on a simplified model assuming a smooth spherical particle contacting a smooth surface [156]:

$$\boldsymbol{F}_{\mathrm{vdW}} = -\frac{A_h r}{6H_0^2}\left[\frac{1}{1+58.14r\cdot\mathrm{RMS}/\lambda_d^2}+\frac{1}{1+1.817\mathrm{RMS}/H_0^2}\right]\boldsymbol{n} \tag{4.8}$$

where A_h is the Hamaker constant, H_0 is the minimum separation distance between the adhering particle and asperity (0.3 to 0.4 nm), RMS is the root mean square roughness of the flat surface and λ_d is the average peak-to-peak distance between asperities.

Image force is obtained by:

$$\boldsymbol{F}_I = -\frac{q^2}{4\pi\varepsilon_0\left(2y_p\right)^2}\boldsymbol{n} \tag{4.9}$$

where y_p is the height of particle above the surface and ε_0 is the vacuum permittivity;

Air drag force is generally simplified as:

$$\boldsymbol{F}_{Drag} = -6\pi\eta r\boldsymbol{v}_p \tag{4.10}$$

where η is the viscosity of air, $\boldsymbol{v}_\mathrm{p}$ is the velocity of the particle.

Finally, the motion equation of particle in the *x-y* Cartesian coordinate system is expressed as:

$$\begin{cases} m\dfrac{dx^2}{dt^2} = F_{C,x} + F_{DEP,x} + F_{Drag,x} + F_f\cdot\delta_{yr} \\ m\dfrac{dy^2}{dt^2} = F_{C,y} + F_{DEP,y} + F_{Drag,y} + F_G + F_I + F_{\mathrm{vdW}}\cdot\delta_{yr} \end{cases} \tag{4.11}$$

where δ_{yr} is the Kronecker delta and is equal zero if the particle has a y value greater than r.

4.2.2 Electric Field Calculation

According to superposition theory, the potential above electrodes of the model in Fig. 4.1 can be obtained by:

$$\phi(x,y,t) = V_A\left(f(x,y)\cos(\omega t) + f(x,y-\lambda/3)\cos(\omega t-\varphi_1) + f(x,y-2\lambda/3)\cos(\omega t-\varphi_2)\right) \tag{4.12}$$

where λ is the wavelength, φ_1 and φ_2 are the phase differences, $f(x, y)$ is the potential generated by the first phase potential with amplitude of unit voltage while the other two phases are set to be zero, and V_A is the amplitude of applied voltage. The wavelength is given by the product of the number of phase and pitch.

Based on Laplace's equation, potential function can be expressed as the product of trigonometric function related to x and exponential function related to y. And if the axis of $x = 0$ is set at the middle of the first phase electrode, there is:

$$f(x,y)=\sum_{n=0}^{\infty} a_n \cos(\alpha_n x) e^{-\alpha_n y} \tag{4.13}$$

where α_n and a_n are coefficients dependent on boundary conditions and $\alpha_n > 0$.

The accurate distribution of potential on the boundary $y = 0$ can be obtained using the results of BEM in chapter 3.

Fig. 4.3 shows the potential when the wavelength $\lambda = 6$ mm and the gap between electrodes equals to the width of electrode.

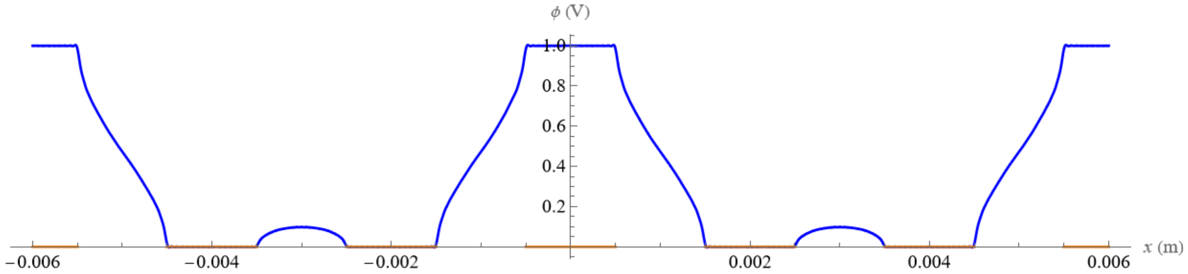

Fig. 4.3 Potential distribution on a certain height at y=0.

A polynomial function (4.14) is used to numerically fit the potential:

$$\phi(x,0)=\begin{cases} 1, & 0 \le \mathrm{x} \le \lambda/12 \\ \sum_{i=0}^{j} c_i x^i, & \lambda/12 < \mathrm{x} \le \lambda/4 \\ 0, & \lambda/4 < \mathrm{x} \le 5\lambda/12 \\ \sum_{i=0}^{j} l_i x^i, & \lambda/12 < \mathrm{x} \le \lambda/2 \end{cases} \tag{4.14}$$

where c_i and l_i are coefficients and j is the order of polynomial function. Then, a_n can be calculated by the integral:

$$a_n = \frac{4}{\lambda} \int_0^{\lambda/2} \phi(x,0) \cos(\alpha_n x) dx \tag{4.15}$$

where $\alpha_n = 2n\pi/\lambda$. Finally, the electric field comes from the negative gradient of the potential function.

Combining formulas (4.12), (4.13), (4.14) and (4.15), the first two terms of electric field in the *x* and *y* direction is:

$$\begin{cases} E_x = V_A\left(\frac{3a_1\alpha_1}{2}\sin\left(\alpha_1 x - \omega t\right)\exp\left(-\alpha_1 y\right) + \frac{3a_2\alpha_2}{2}\sin\left(\alpha_2 x + \omega t\right)\exp\left(-\alpha_2 y\right)\right) \\ E_y = V_A\left(\frac{3a_1\alpha_1}{2}\cos\left(\alpha_1 x - \omega t\right)\exp\left(-\alpha_1 y\right) + \frac{3a_2\alpha_2}{2}\cos\left(\alpha_2 x + \omega t\right)\exp\left(-\alpha_2 y\right)\right) \end{cases} \tag{4.16}$$

where $a_1 = 0.484$, $a_2 = 0.235$ in this model.

4.2.3 Simulation Parameters and Set-up

Various operating and system parameters will affect the motion characteristics of particle, as well as its own physical properties. In the simulations, the properties for the simulated particle is selected as the same as the material of ballotini, which refers to small glass beads that are commonly used for various applications and experimental research. And ballotini particles are usually spherical and have uniform size, which facilitates experiment research and comparison in future. The parameter of charge on the particle in the simulation is important. Experiments for measuring the charges of particles are introduced in section 4.2.3.1, which is used to estimate the maximum charge on ballotini particles potentially. Other simulation parameters and set-up are introduced in section 4.2.3.2.

4.2.3.1 Charge of Particles

A free fall system is used to measure the charges of ballotini particles and the diagram is shown in Fig. 4.4. A funnel and slit system allow a particle to fall straight into the normal electric field. The Coulomb force, air drag force and gravitational force are considered as the main effect on particle motion. Therefore, movement formulas in the *x* and *y* direction can be given as:

$$\begin{cases} my'' = -6\pi\eta r y' + mg \\ mx'' = -6\pi\eta r x' + E_d q \end{cases} \tag{4.17}$$

where *m* is the mass of particle. E_d is the normal electric field, which equals to ($U_p - U_n$) divided by *l*. U_p and U_n are the voltage applied on the positive and negative panel. *l* is the distance between the two panels.

In the experiment, the diameters of particle are classified into three groups: 50 to 150 μm, 150 to 250 μm, and 250 to 400 μm. A mass of 0.5 g of neutralized particles are shaken in a cylinder stainless-steel cup by hand for 2 minutes. The height and diameter of cup is 60 mm and 20 mm. The shaking frequency is two shakes per second and kept constant throughout all of the experiments. During the shaking, there is tribocharging between particles and particles with the stainless-steel wall. The contacting between particles will make particles have opposite charge since they are the same material, while the contacting between particles and wall will make particles acquire negative charge. After the shaking, particles are fed into the stainless steel funnel and free fall into the electric field. The parameters of the systems are: $h_1 = 120$ mm, $h_2 = 360$ mm, $l = 175$ mm, $U_p = 15$ kV, and $U_n = -15$ kV.

According to motion equations (4.17) and the particle properties, the charges on particle can be obtained through the distance that particles travel away from centre line, and the distance increases linearly with charge. The locations of 250 to 400 μm particles fallen through funnel and slit are shown in Fig. 4.5. Particle saturation charge is evaluated by the relation of Pauthenier [152]:

$$q_m = 4\pi r^2 \varepsilon_0 \frac{3\varepsilon_p}{\varepsilon_p + 2} E_c \tag{4.18}$$

where E_c is the dielectric strength of air and $E_c \approx 3\times10^6$ V/m, and ε_p is the relative dielectric permittivity of particle.

Calculations of particle charge from the measured results of three groups of particles are shown in Fig. 4.6. The abundance ratio is defined as the percent of particles with certain charges and the charge is represented as the percent of saturation charge. The results show that the bulk charge of particles were negative, which was due to the metallic stainless steel cup. The charges of most particles lie within 15% of saturation charge. The collision of particles can introduce errors in experimental results. Therefore, it was used to predict the maximum possible electric charge of the particles.

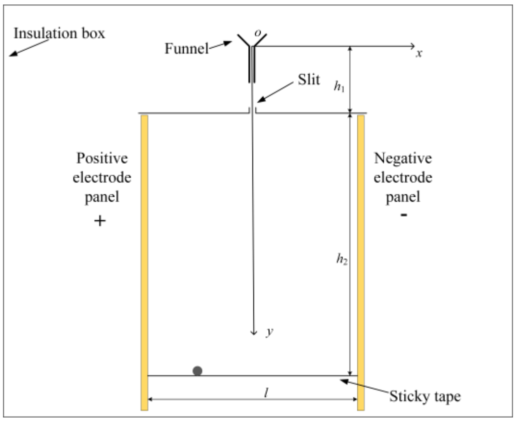

Fig. 4.4 Diagram of the free fall system composed of two parallel panel charged with DC voltage and a funnel feeding particles.

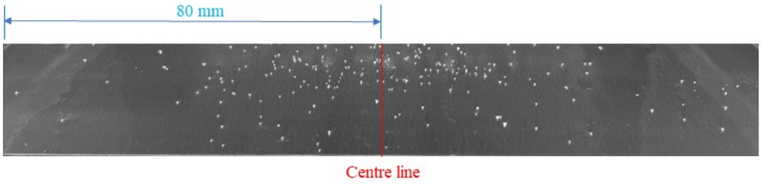

Fig. 4.5 Particles trapped on the tape, after falling through the DC fields, in a distributed manner.

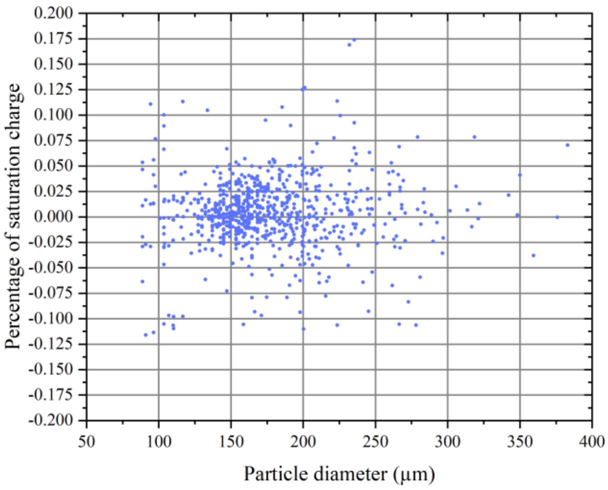

Fig. 4.6 Measured charge distribution of ballotini particles post-shaking in a stainless-steel cup.

4.2.3.2 Simulation Set-up

The main variables are particle size and charge, and frequency. Wavelength is also researched, and it is related to the arrangement of electrode configuration, while the phase number and wave profile of input voltage are fixed. In addition, the effect of the initial conditions, such as particle initial velocity and positions are investigated. The range of variables are listed in Table 4-1.

Table 4-1 Simulation parameters

Parameters	Value	Unit
Applied voltage wave type	Sinusoidal wave	
Applied voltage wave phase	3	
Applied voltage frequency, *f*	20 to 200	Hz
Applied voltage amplitude,	1500	V
Electrode width, *d*	1	mm
Electrode pitch, *p*	2	mm
Wavelength, λ	4 to 16	mm
Particle type	ballotini	
Particle size	10 to 400	μm
Particle density, ρ	2.5	kg/m^3
Particle relative permittivity,	3.7	
Initial position in *x* and *y* axis	x_0, y_0	m
Initial velocity in *x* and *y*	v_{x0}, v_{y0}	m/s

The computation procedures and set-up are as follows:

1) Only the first two terms of the Fourier expansion series are maintained to represent the electric field;

2) Particles are assumed spherical and charge is evenly distributed on the surface and constant in the simulations;

3) Elastic collisions between the particle and conveyer surface are assumed, so the particle horizontal velocity keeps constant and vertical velocity reverses after collision;

4) The origin of *x*-*y* coordinate is set on the surface of the middle position of first phase electrode. The wave direction is the positive direction of *x* axis and the upward direction is the positive direction of *y* axis. The package of NDSolve in Wolfram Mathematica is used to solve motion equations using Runge-Kutta methods. To ensure the accuracy, stability, and consistency of the simulation results, the calculation step size should be fixed and kept small, preferably no larger than 10^{-6} s, comparing that the average time for a particle across a wave length is about 10^{-4} s

4.3 Simulation results

A series of combinations of parameters with different values, such as voltage frequency, particle size and charge, were simulated to produce particle trajectories. Particle motion modes, moving velocity and the variation of forces on particle are obtained through their trajectories. The effect of simulation parameters on the transitions of motion modes and particle moving average velocity are analysed in detail.

4.3.1 Analysis of Simulation Results

4.3.1.1 Effect of Particle Charge, Wavelength and Frequency

Coulomb force is thought to be the predominate force to drive particles in ETW fields, which is largely related to the charge of particle and characteristics of electric field. In addition, the frequency of applied voltage is a key parameter that affects the particle motion mode. In this section, the effects of charge, frequency and wavelength are examined. In the simulations, the particle size is fixed at 10 μm and other parameters are set as in Table 4-1. The initial position of x_0 and y_0 are zero and *r*, respectively. Particle is set motionless initially on the conveyer, so the initial velocity is zero.

The variation of simulated average velocity in terms of charge and frequency is shown in Fig. 4.7. The frequency is increased by 5 Hz from 20 Hz to 100 Hz and q is the ratio of particle saturation charge. At lower frequencies, the particle moves in surfing mode and the calculated average velocity increases with frequency linearly proportionately to wavelength λ. Therefore, the average velocity of a particle in surfing mode equals the wave velocity: $v = \lambda f$. This relation has been verified by testing different wavelengths and the results are shown in Fig. 4.8. The increase of wavelength can significantly increase particle velocity as long as particle remains in surfing mode. However, the range of frequency for the surfing mode is compressed with the increase of wavelength. Particle charge also has an effect on the transition of motion mode. Fig. 4.7 shows that the increase in particle charge will extend the frequency domain for surfing mode. The transition of motion modes is analysed in the following sections.

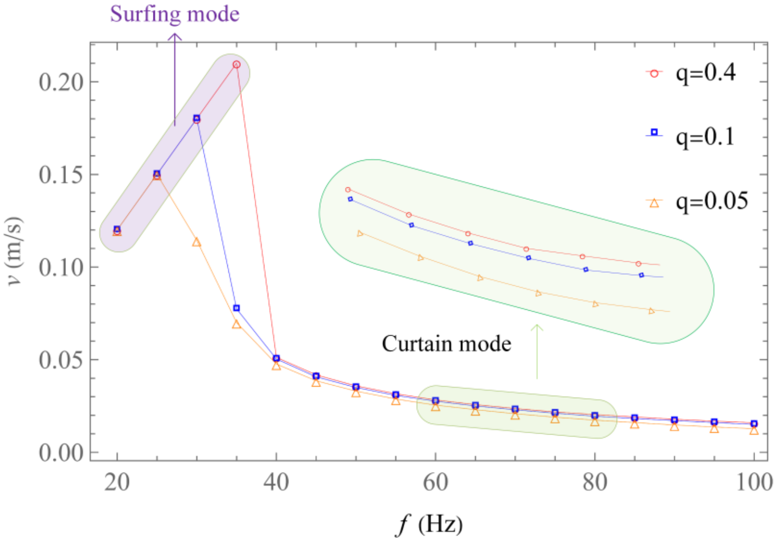

Fig. 4.7 Relationships between average velocity and motion mode with charge and frequency.

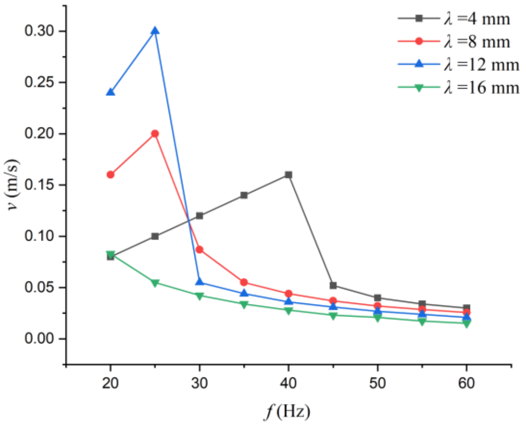

Fig. 4.8 Relationships between average velocity with wavelength and frequency.

The typical trajectories of surfing mode and curtain mode motion are shown in Fig. 4.9. The blue trajectory shows particle motion at frequency of 60 Hz in the first 1.0 s, while the red trajectory shows particle motion at a frequency of 20 Hz in the first 0.2 s. Surfing mode displays a cyclic motion due to the characteristic of rotational travelling electric field and the balance of air drag due to the large velocity in *x* direction. The condition for particle motion in surfing mode is that the Coulomb force in *y* direction must be downward in most time. The analysis of the variation of forces on particle in the *y* direction for surfing mode during 0.1 to 0.118 s is shown in Fig. 4.10.

Curtain mode has a cyclic motion due to the rotational travelling electric fields and the balance of the Coulomb force with the gravitational force. In curtain mode, particle is levitated away from electrodes, where the electric field is much weaker. A particle vibrating in the *y* direction stays in equilibrium state of Coulomb force and gravitational force. The two forces on a particle in curtain mode is shown in Fig. 4.11. At this height, the gravitational force is always comparable to the Coulomb force, unlike particles near the surface.

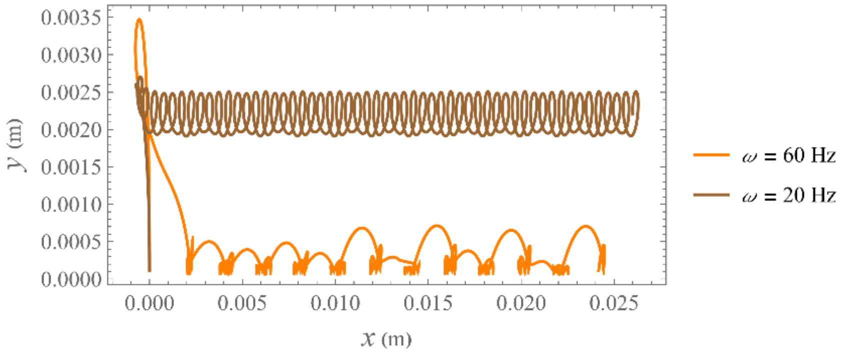

Fig. 4.9 Trajectories of curtain mode and surfing mode motion at different frequencies.

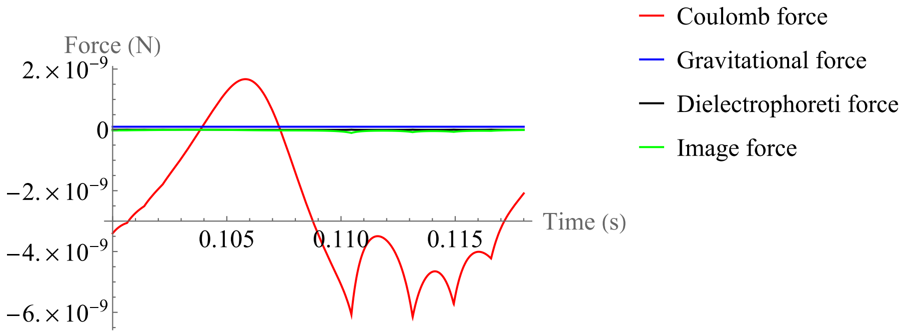

Fig. 4.10 Forces variation in *y* direction during particle movement in surfing mode.

The condition for a particle entering into the curtain mode or surfing mode is whether the particle can escape from the equilibrium state and be dragged down to the conveyer surface. Comparing the trajectories in Fig. 4.9, particle in both modes are levitated away from electrodes in the beginning stage, which is due to the acceleration of strong electric field near the surface of electrodes. As the particle is levitated, the Coulomb force weakens and particle slows to zero velocity in the *y* direction, then falls due to gravity. The electric field exhibits alternating positive and negative polarity [33].

If the particle has higher charge or the frequency is smaller than the curtain mode condition, shown as the dash line in Fig. 4.11, the total work done by Coulomb force will be larger in the period of negative polarity. In this way, the particle moves lower down and may escape the equilibrium range. The closer particle is to the electrode, the stronger the electric field, which will make particle fall faster to the electrodes and enter into surfing mode. For the condition with larger wavelength, the negative period is shorter. In addition, simulation results show that particle will be levitated higher with larger wavelength. Both consequences resist the particle escaping the range of curtain mode.

Therefore, the increase of wavelength shortens the range of frequency for surfing mode to lower frequencies.

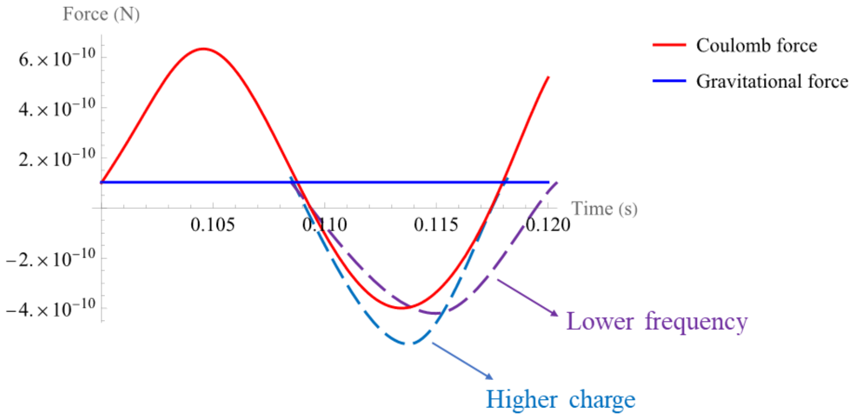

Fig. 4.11 Variation of forces in the *y* direction during particle motion in curtain mode.

4.3.1.2 Effect of Particle Size and Frequency

Considering the gravitational force $\boldsymbol{F}_G \propto r^3$ and the Coulomb force $\boldsymbol{F}_C \propto q \propto r^2$, an increase in particle size weakens the Coulomb force compared to the gravitational force. The gravitational force may prevent the particle entering into curtain mode. As a result, hopping mode is the most common motion mode for relative large particles. However, for particles of even larger sizes, the Coulomb force is not large enough to levitate the particle and with the action of travelling dielectrophoresis, the particle can only roll along the surface. The predominate force in this surfing mode is the combination of dielectrophoretic force and Coulomb force, which is different from that of small particles in surfing mode.

In the simulations on the effects of particle size and voltage frequency, the charge of particle is set as 10% of the saturation charge and the amount of charge on a particle varies with size. Particle size is set to 70 µm, 90 µm, 110 µm, 130 µm, respectively. The initial position of x_0 and y_0 are zero and r, respectively. Initial velocity is zero. Other parameters are set as in table 1. The total simulation time is 6 s and the displacement divided by the time intervals of 2 s to 5 s is regarded as average velocity. The results of simulated trajectories show that most particles are in the hopping mode when frequency varies from 40 Hz to 120 Hz with step size of 5 Hz. Fig. 4.12 shows the interpolation distribution of particle average velocity with different frequencies and their potential motion modes based on the measured average velocity.

At lower frequencies, particle average velocity tends to increase with an increase of frequency. However, when frequency increases further, the particle velocity drops quickly and even moves backward at certain high frequencies. In addition, particles with larger size tend to drop and move backward at lower frequencies. These simulated results and conclusions show good agreement with previous work [32, 33]. The backward motion has been explained as the action of the second harmonic wave of the travelling wave field, which is the second term in formula (4.16). However, small particles can be driven by the travelling wave and move forward at low frequencies in hopping mode. The backward motion due to the effect of harmonic wave is only noticeable when the particle size is large or frequency is high. The relationship between the effect of harmonic wave with particle size and frequency has not been clearly explained previously. The following paragraphs provide a potential explanation.

According to formula (4.15), the coefficient $3a_1\alpha_1/2$ is slightly larger than $3a_2\alpha_2/2$, so the driving effect of the second harmonic term is close to the first term when particle is near the surface. Regarding the coefficient $\alpha_2 = 2\alpha_1$, the second term decays faster than the first term. Therefore, as particle levitates, the effect of second term decreases quickly and only the first term dominates. The electric field in the x direction at a height of $y = 0$ and $y = 2$ mm at different time in a period of T (0.02 s) is shown in Fig. 4.13 (*a*) and (b). The two figures show that electric field at electrode surface is almost like a standing wave field while field away from electrodes is a travelling wave field. The fact is that if particle lies in a standing wave, the moving direction could either be forward or backward. In this way, the approximate standing wave area near surface appears to be the reason for the backward motion of particle. These explanations align well with the experimental observations, which will be introduced in the chapter 5 and 6.

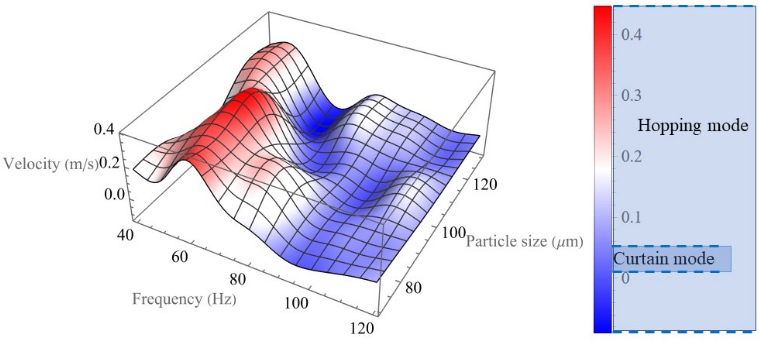

Fig. 4.12 Relationships between average velocity with particle size and frequency, colour bar indicating the amplitude of velocity.

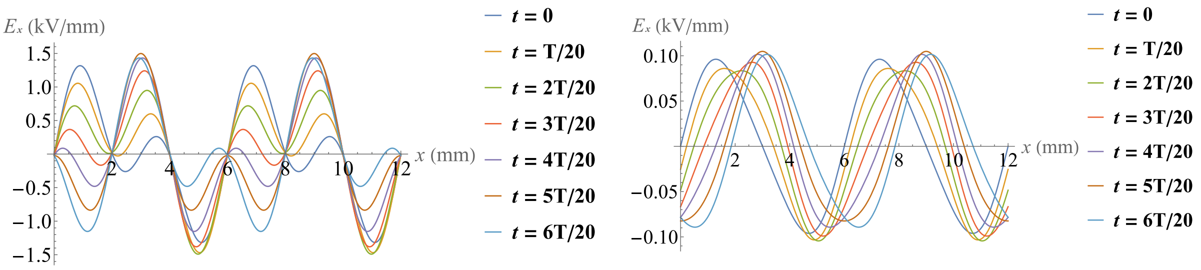

(*a*) At a height of $y = 0$.

(b) At a height of $y = 2$ mm.

Fig. 4.13 Electric field variation at different time in a period in x direction.

Even though the second harmonic term of electric field introduces backward driving characteristic, most areas in the field are dominated by the first term and show a forward driving characteristic. Hopping mode is not stable compared to surfing and curtain modes. Particles in hopping mode are not likely to travel along the wave and the behaviour of a particle is hard to predict. Small perturbations for a particle in hopping may lead to large differences of the trajectory. Under most conditions, particles will travel forward. Two conditions can increase the probability for particle moving backward: hopping close to surface, and a high frequency field.

Hopping close to surface means that the particle may stay close to the standing wave area, which may lead the particle to move backward. Fig. 4.14 (*a*) shows a simulated trajectory for a 60 μm particle at 70 Hz. Most of the time, the particle will be hopping higher than 0.004 m and travel forward. However, it can be observed that if the particle stays in the area lower than 0.001 m, the particle moves backward. Fig. 4.14 (b) shows that when the size of a particle increases to 130 μm, with larger gravitational force, it hops in the standing wave zone and keeps moving backward by chance.

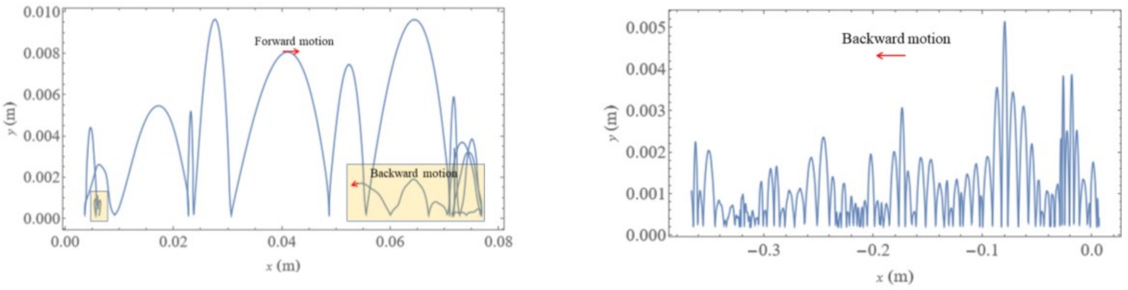

(*a*) size: 60 μm; frequency: 70 Hz (b) size: 130 μm; frequency: 70 Hz

Fig. 4.14 Simulation of particle trajectory in hopping mode with different motion direction.

For the second condition (high frequency field), due to the action of air drag force, the particle can not keep up with the travelling wave, which has high wave velocity. If the wave field travels too fast, accelerated and decelerated regions intersect through the particle. The moving direction then depends on the contacting times and strength of acceleration in forward and backward directions. Therefore, particles have a larger chance to move backward at higher frequencies.

The mechanism for backward motion has been explained here based on the effect of the resultant harmonic waves. Lower levitation height and higher frequency increase the probability of a particle moving backward. This explanation will guide the design of particle separation system based on different motion directions.

4.3.1.3 Effect of Initial Conditions

Particle motion equations are second order differential equations, so the results of (x, y) should depend on the initial conditions of (x, y) and (v_{x0}, v_{y0}). Some previous studies [33, 67, 69] have revealed that the trajectories of particles could be effected by initial positions. Gu and co-workers [39] have done detailed experimental research on the effect of initial positions in their four-phase rectangular system. In this section, the effect of initial position was analysed in terms of motion modes in the simulation conditions and firstly the effect of initial velocity was included.

Fig. 4.15 and Fig. 4.16 show trajectories of particles in surfing mode and curtain mode with different initial positions. The simulation frequency in Fig. 4.15 and Fig. 4.16 were 20 Hz and 70 Hz, respectively. Other parameters were kept the same: (r = 10 μm, q = 0.1, V_A = 1000 V, $y_0 = r$, $v_{x0} = 0$, $v_{y0} = 0$). It is true that the difference of electric field at different positions affects the initial motion. However, once the Coulomb force dominates other forces, the initial positions do not further affect particle motion modes, as can be seen in Fig. 4.15 and Fig. 4.16.

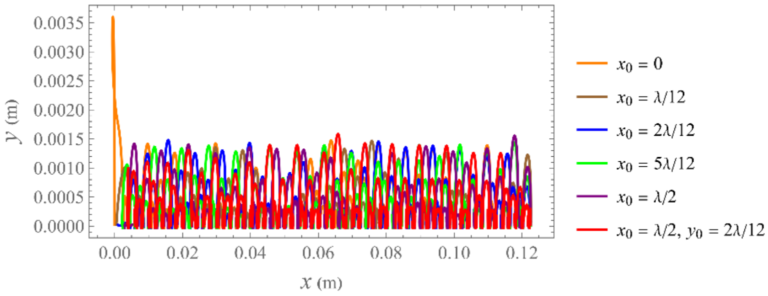

Fig. 4.15 Simulated results of trajectories of particles with different initial positions at 20 Hz showing 'surfing mode'.

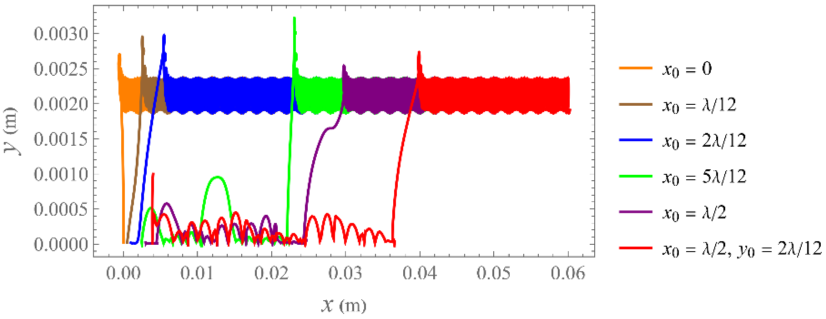

Fig. 4.16 Simulated results of trajectories of particles with different initial positions at 70 Hz showing the eventual 'forgetting' of the initial position and entering 'curtain mode'.

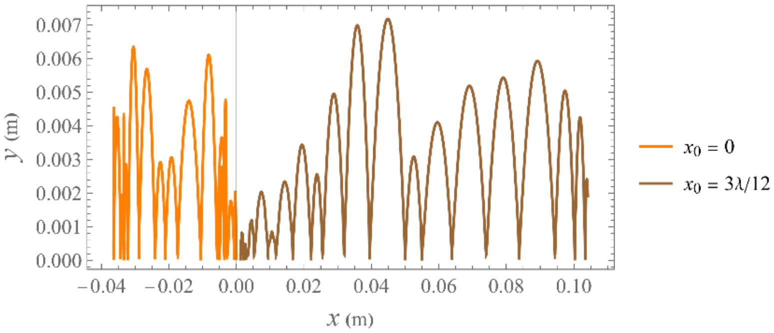

Fig. 4.17 Simulated results of trajectories of particles with different initial positions at 110 Hz, 'hopping mode'.

In hopping mode, the particle motion is not determined solely by the action of forces. Trajectories of particles may be effected largely by initial positions and have different moving direction, especially at high frequencies, as shown in Fig. 4.17, where particle size is 130 μm and the frequency is 110 Hz.

In terms of the initial velocity of particles, an increase may impede their ability to levitate to the required height for curtain mode, thus altering their motion. Fig. 4.18 shows different motion modes under different initial velocities. Here v_0 represents initial velocity in x direction. Other parameters are kept the same: ($r = 20$ μm, q = 0.1, $V_A = 1000$ V, $f = 100$ Hz, $x_0 = \lambda$, $y_0 = r$, $v_{y0} = 0$). However, for most conditions, if the initial velocity of a particle is not large enough or the initial position has high electric field intensity, the particle will still be levitated and enter into curtain mode.

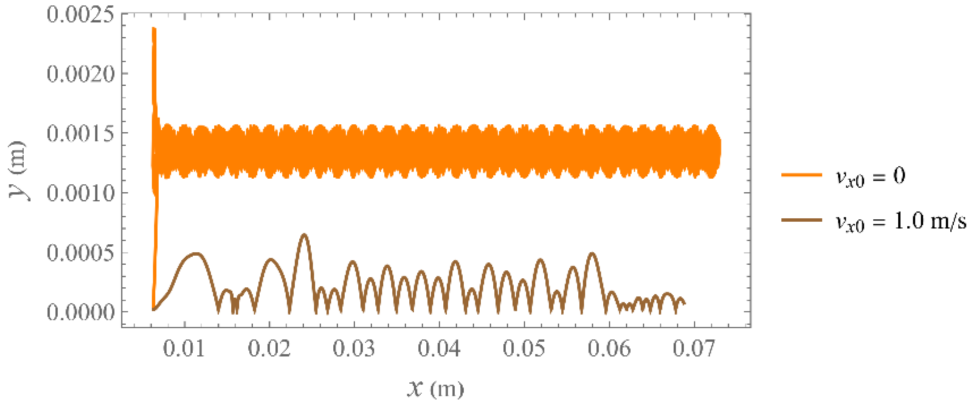

Fig. 4.18 Simulation of particle trajectories with different initial velocities at 110 Hz.

4.3.2 Particle Motion Direction Analysis

The previous section shows the overall simulation results, including the effect of different parameters on particle motion modes, moving velocity and levitation height. And it reveals that particle motion direction could be manipulated, which may be utilized to separate particles by size. In this section, the motion direction of particles is specifically studied to seek out an appropriate design for particle separation by size.

4.3.2.1 Motion direction related to initial positions

The trajectories of particles could be affected by initial position and exhibited different moving directions in hopping mode, especially at higher frequencies, shown in Fig. 4.7. And it is possible to predict the direction of travel for particles. The particle diameter was set at 250 μm and the particle charge was at 5% of the saturation charge. The simulation was run at the frequency of 100 Hz by selecting 1000 random initial positions across a wavelength and their relative displacements after a time of 0.5 s were recorded. A time interval of 0.5 s was chosen because the experimental board is 0.2-meter long, aligning with the average distance particles cover within that time frame. The relative positions are shown in Fig. 4.19. The number of particles in forward direction is 489, which means the estimated probability for particles moving forward is 48.9%. A similar simulation without DEP have been done and the result is shown in Fig. 4.19 (b). The particles in Fig. 4.19 (b) move further away in the forward direction. The comparison of (a) and (b) shows that adding DEP increases the probability of particles moving in the backward direction. However, the effect of DEP on backward motion is less significant compared with harmonic waves and other effects, and affects mainly particle motion close to surface, as DEP decays much faster than Coulomb force as particles levitate away from the surface.

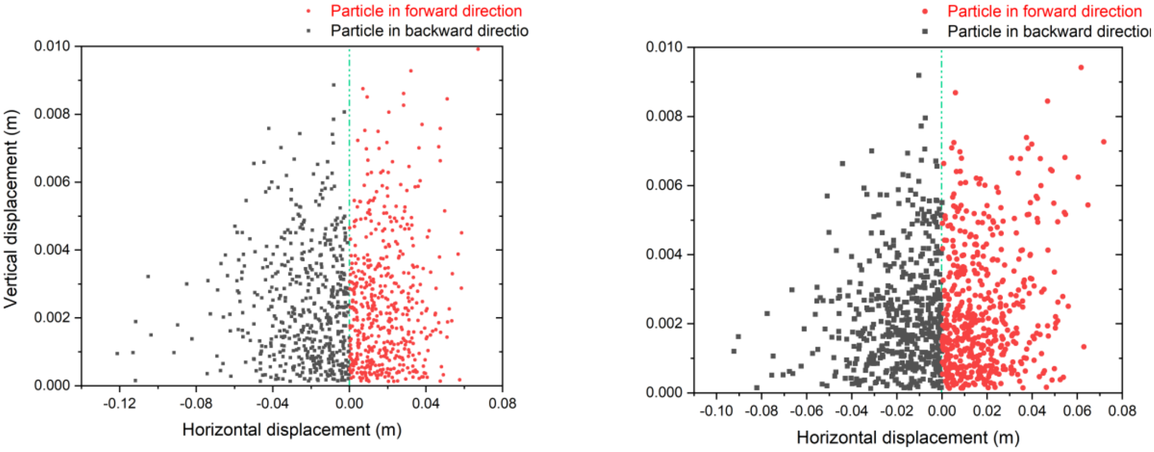

(*a*) With DEP (b) Without DEP

Fig. 4.19 Scatter plot of particle positions at the frequency of 100 Hz for particles of 250 μm with random initial position.

4.3.2.2 Effect of Frequency, Particle Size and Charge

At low frequencies, the wave velocity is low and particles can de driven by the electrostatic travelling wave to move synchronously. The first order wave is dominant, so most of the particles will follow along the wave in the forward direction. Fig. 4.20 (a) shows the final positions of 1000 particles with a random starting position at a frequency of 40 Hz. The number of particles in the forward direction is 774.

When the frequency increases, the wave velocity increases. Due to the action of the air drag force, the particle can not keep up with the travelling wave. If the wave field travels at a high-speed, the accelerated and decelerated regions intersect through particles. The subsequent movement direction is determined by the frequency and intensity of forward and backward accelerations. The forces induced by Coulomb forces in both positive and negative directions counterbalance each other, making the effect of DEP more pronounced. Therefore, particles have a larger chance to move backward at higher frequencies. Fig. 4.20 (b) presents simulation results at 200 Hz, the fraction of the particles in the backward direction increases compared with that at low frequencies. The travelling distance also decreases with an increase of frequency, which demonstrates the counterbalancing effects of forward and backward waves.

As the particle size increases, the saturation charge decreases [157]. It assumed that the saturation rate for particle size at 150 and 350 μm were 10% and 2% based on the charge measurement in section 4.2.3. The charge and size of particles are the critical factors affecting particle motion. Simulations were carried out recording the fraction of particles of different sizes moving in the forward direction at various frequencies, as shown in Fig. 4.21. It is evident that as the frequency increases, the fraction of particles moving forward decreases. The results of Fig. 4.21 also demonstrate that larger particles tend to move backward at lower frequencies, while a large percentage of smaller particles travel in the forward direction.

The above simulation results suggest that a system operating at a specific frequency could be used to separate particles by size.

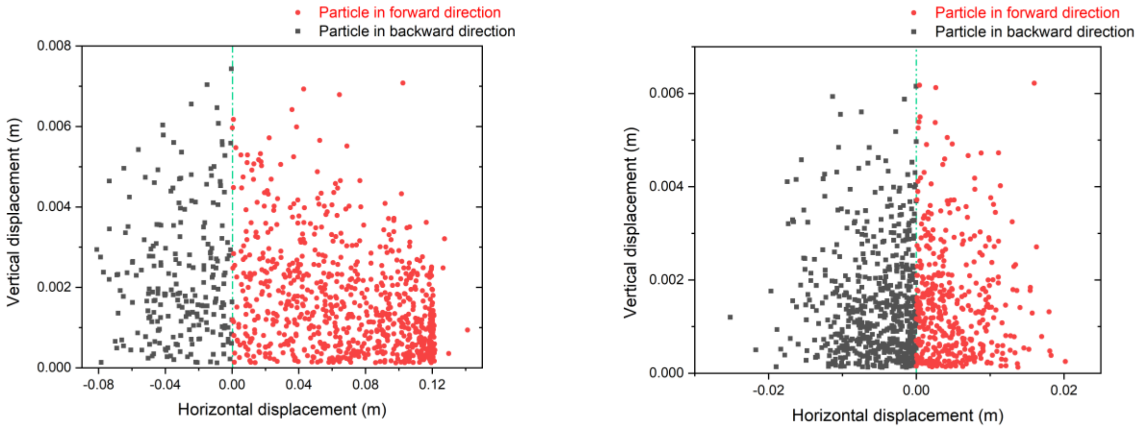

(*a*) 40 Hz

(b) 200 Hz

Fig. 4.20 Scatter plot of particle positions for particles of 250 μm with random initial position at different frequencies.

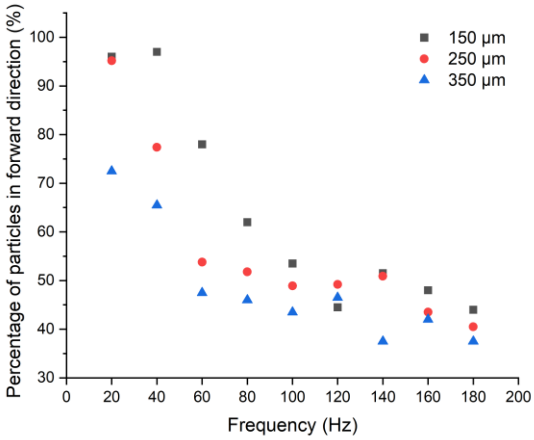

Fig. 4.21 Relationship between the percentage of particles in forward direction and frequency based on the simulation results.

4.3.3 Comparison of Analytical Results and Numerical Results

In order to verify the simulation model, the average velocity and levitation height are compared with the analytical results, which are shown in Fig. 4.22 (*a*) and (b). The formulas and derivation process can be found from the appendix A. Parameters are kept the same: (r = 30 µm, q = 0.2, V_A = 1000 V, f = 100 Hz, $x_0 = 0$, $y_0 = r$, $v_{x0} = 0$, $\mathrm{v}_{y0} = 0$). The comparisons show close agreement. With analytical solutions, the effect of different parameters or their combinations on curtain mode motion can be evaluated more clearly. In addition, key parameters may be derived from formulas that can determine particle motion modes.

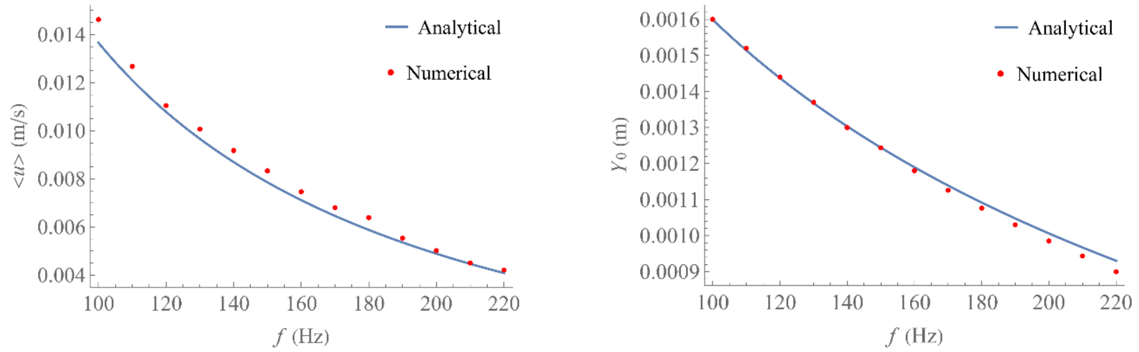

(*a*) Comparison of average velocity (b) Comparison of average levitation height

Fig. 4.22 Comparison of analytical and numerical results on particle average velocity and levitation height.

4.4 Conclusion

This chapter presents a detailed simulation model, which can be used to predict and control particle motion in ETW fields. The results clarify and explain the effect of various parameters on particle moving velocity and levitation height in terms of motion modes. The conclusions provide insights for the design and optimization of ETW systems, potentially improving transportation efficiency and inspiring separate ideas. The findings are:

1. Small particles in surfing mode tend to move along the travelling wave and the average velocity equals to the wave velocity. An increase in wavelength could increase particle velocity in surfing mode but also decreases the frequency domain for a particle entering into surfing mode;
2. Based on the simulation results and analysis of different forces in a period, an equilibrium state was used for the description of curtain mode. An increase of particle size or decrease of particle charge could make particle leave the equilibrium state and enter into hopping mode;
3. The levitation height of a particle and wave velocity are additional factors that affect particle motion mode. Particles closer to surface will be affected more by the approximate standing wave field. Therefore, particles with larger sizes at higher frequencies are affected more by the backward harmonic waves and to move backward;

4. The effect of different initial positions on particle motion characteristics was clarified. Due to the difference of electric field at different initial positions, the initial levitating stage of particle motion will be affected and thus the trajectory for particles in hopping mode may be considerably changed. However, if a particle is likely to enter curtain mode or surfing mode, the initial positions will not have a significant effect. Instead, the change of initial velocity could affect the motion mode, which may be used to improve the efficiency of transport;
5. The motion direction of particles was specifically researched at different frequencies, which provides a potential design for particle separation by size.

Chapter 5 Single-particle Experiments

5.1 Introduction

The previous chapters simulated the effects of system and operating parameters on particle transport characteristics, such as motion mode, moving velocity and levitation height. These conclusions provide guidance for the design and optimization of ETW systems, for particle separation by size. The following chapters address the experimental research. These results validate the theories and simulation results.

Experiments can provide more direct and accurate information in the design and application of devices. Results-oriented experiments, such as dust removal and particle separation, focus on multi-particle scenarios. Multi-particle experiments are more appealing, because the experimental outcomes are highly intuitive, and with specific structural optimizations, performance can be significantly enhanced. In previous experimental research, researchers have predominantly involved multiple particles [158], with few instances of single particle experiments [159].

ETW is inherently a chaotic system with numerous systematic parameter variables, such as electrode configurations and properties of applied voltage. When introducing multi-particle experiments, the interactions between particles, disturbances to the electric field from net charge, and tribocharging between particles extensively contribute to experimental instability, making it challenging to analyse causality. For example, most experimental conclusions in the literature are qualitative and the basic relationships between particle transport characteristics, conveyor parameters and applied voltage remain unclear. This makes experimentally observed phenomena difficult to explain and presents challenges in optimising equipment design.

The value of single particle experiments is to clarify the basic mechanisms. It facilitates a more straightforward quantitative analysis of variables. Single particle simulations are straightforward and avoid complexities of particle-to-particle interactions (e.g. electric forces and collisions). In addition, the single particle simulation results cannot be robustly verified without the comparison of results single particle experiments.

This chapter first introduces the set up of the experimental platform, control of the experimental conditions and selection of the materials. Then it details the experimental procedures, the data collection and analysis methods. The single particle experiment results clearly present the three kinds of typical motion modes and the effect of particle size on the transition of motion modes. In addition, the effect of frequency on moving speed is quantitatively analysed. The DEP effect on particle motion direction is demonstrated by controlling particle charge. In addition, the conclusions of experiment results were compared with that of simulations. The similar conclusion from both results confirms the simulation model. Limitations and conclusions are presented finally.

5.2 Material and Experiment Set-up

This section details each component. The components and their relationship are as shown in Fig. 5.1, including the fabrication of the ETW board, the operation of the function generator, details, verification and operation of the power supply system, and the observation system using high-speed camera and photography.

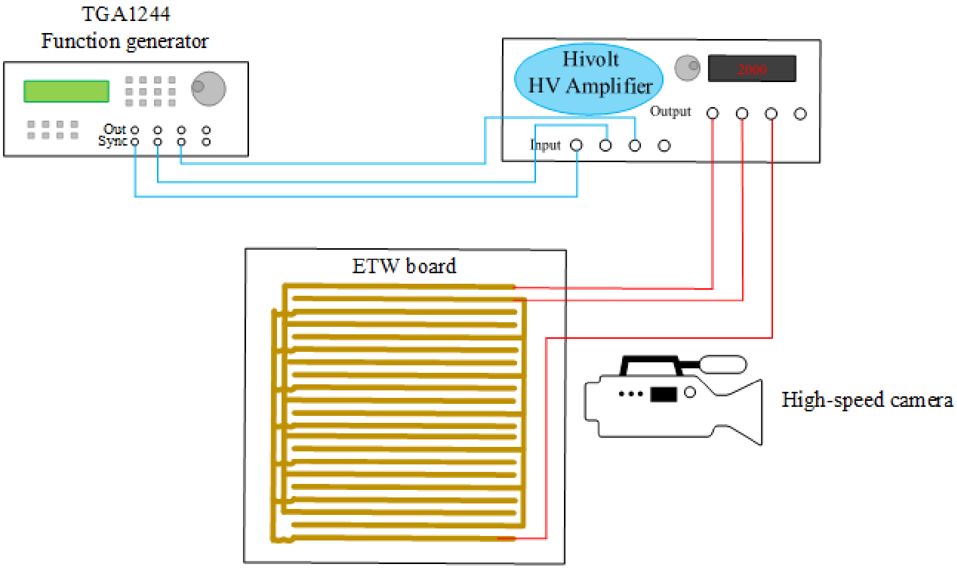

Fig. 5.1 Schematic diagram of experimental system consisting of power system, ETW board and observation system (note, system grounding not shown for clarity).

5.2.1 ETW Conveyor Board Fabrication

The generation of an ETW field requires a series of parallel electrodes supplied with a multi-phase time-varying voltage. In this research, the design and manufacture of the ETW conveyor board used printed circuit board (PCB) technology. A basic PCB is made up of an insulating material sheet and a tightly bonded layer of copper foil on the substrate. The desired electrode configuration is formed by chemically etching the copper that is retained on the board. The layout design of the electrodes was done by a professional software, and which then transformed into the physical ETW board by a specialised supplier.

A three-phase design of the ETW system was selected, because it represents the minimum number of phases necessary to create a travelling wave field that controls the direction of particle movement. This also allows comparison with simulation results using a three-phase model. The three-phase voltages are delivered to three sets of electrodes separately. This requires an additional layer of PCB to connect these three sets of electrodes independently.

The design of the electrode configuration was made in Kicad software, shown in Fig. 5.2. Red tracks represent the electric circuits in the front layer, while blue tracks represent the electric circuits in the back layer. The electrodes on the corresponding positions of the front and back sides are interconnected with the connecting electrodes on the back via the pads. They are copper-filled holes. The four mounting holes are designed for the support structure of the board. The footprint is designed for the connection with a pluggable terminal block, which was in turn connected with the output of high voltage cables. The width of the board used in the particle separation experiment is 210 mm and the length of each electrode is 200 mm. The width and gap between electrodes are 1 mm. A wider board can generate a more uniform electric field in the central region.

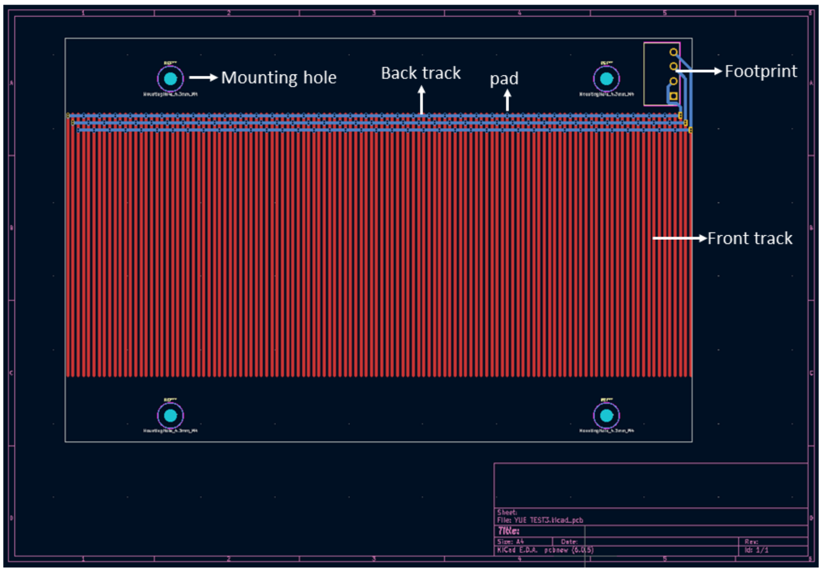

Fig. 5.2 The design of PCB using Kicad and description of each components (the length of electrodes in this example is 90 mm).

The output file from the design was sent to the manufacturer, with PCB specifications. The manufacture of the board was performed by PCBWAY company (details of the company is in appendix C). The main PCB specifications are as follows:

1) number of layers is two;
2) dielectric material is Flame Retardant 4 (FR4);
3) temperature resistance of the material is 150-160°C;
4) minimum size of the pad hole is 0.3 mm;
5) minimum spacing and track is 0.15 mm, which is enough for the design at 1 mm;
6) surface finish is Hot air solder levelling (HASL) with lead;
7) via processes is tenting vias;
8) thickness of copper on the outer layers is 1 oz, which means the weight of copper in in one square foot of PCB;

9) in some design, an extra white silk screen is added to smooth the surface, reducing the effect of wrinkles in the gaps between electrodes.

The physical diagram of the PCB is illustrated in Fig. 5.3.

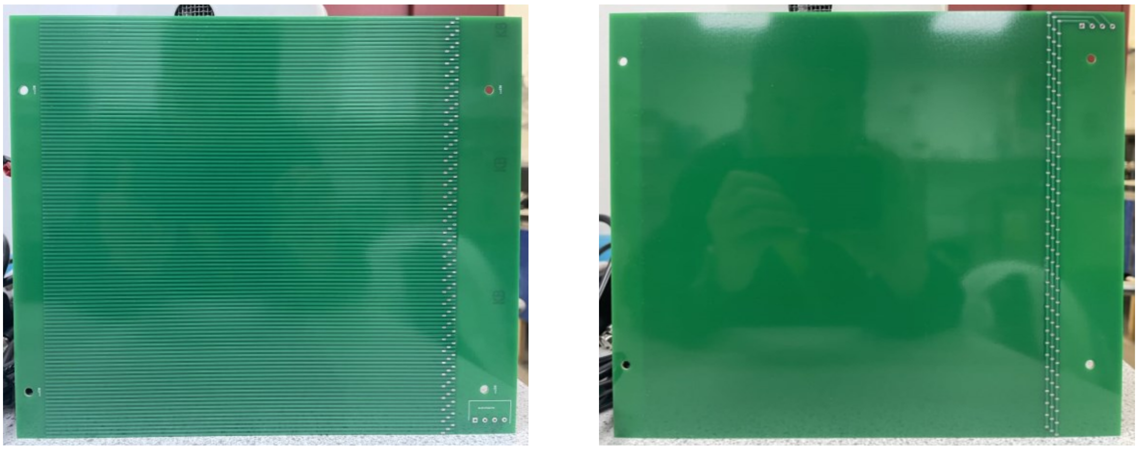

(*a*) Front panel

(b) Back panel

Fig. 5.3 Photograph of the PCB of front and back panel: raised lines represent electrodes.

5.2.2 Experiment Set-up

The experimental set up is illustrated in Fig. 5.4. The function generator and voltage amplifier provide a three-phase high voltage to the ETW board. After activating the system, an ETW field is generated above the ETW board. A vibratory feeder can provide particles with initial velocities and particle charge. This was seldom utilized, only in specific experiments, such as when investigating the impact of particle initial velocity. Particles can be collected by collector containers at each end for weighing and analysis after transportation. The systems is housed in a Perspex case for safety, and to avoid interference from stray air currents.

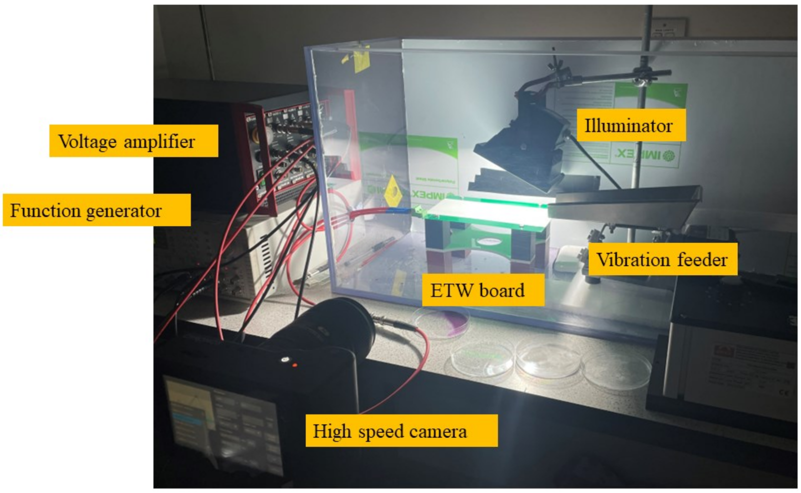

Fig. 5.4 Photograph of experimental setup.

The voltage is supplied by a high voltage amplifier (HAR42-4, hivolt.de) and controlled by a function generator (TGA1244, TTi), both of which have four channels. As noted, only three channels were used in this study.

The TGA1244 function generator combines a true variable clock arbitrary generator with a high performance DDS function generator. The four output channels can be linked with specific phase difference, which is crucial for the control of ETW field. The selectable frequency range for sine-, square- and triangle waves are from 0.1 mHz to 100 kHZ, which meets the experimental needs. The outputs of the function generator were measured and verified by an oscilloscope.

The HAR42-4 is a high precision high voltage amplifier. It provides output voltages of −2000 V to +2000 V at load currents of up to ±5 mA and > 7 mA with four channels. The signal gain is 200, so the input voltage range is −10 V to +10 V. The accuracy of the high voltage output from HAR42-4 was verified by an oscilloscope combined with a high voltage probe. The attenuation factor is 100.

The test and verification of the functions and accuracy of the power system are provided in the appendix C.

5.2.2.1 Observation system

A high-speed camera (Chronos 1.4) and an illuminator were used to capture particle motion in detail. The size of recording area is 50 mm*15 mm in the middle of platform, shown as the pink rectangle in Fig. 5.5. The recording frame rate is 2134 frames per second.

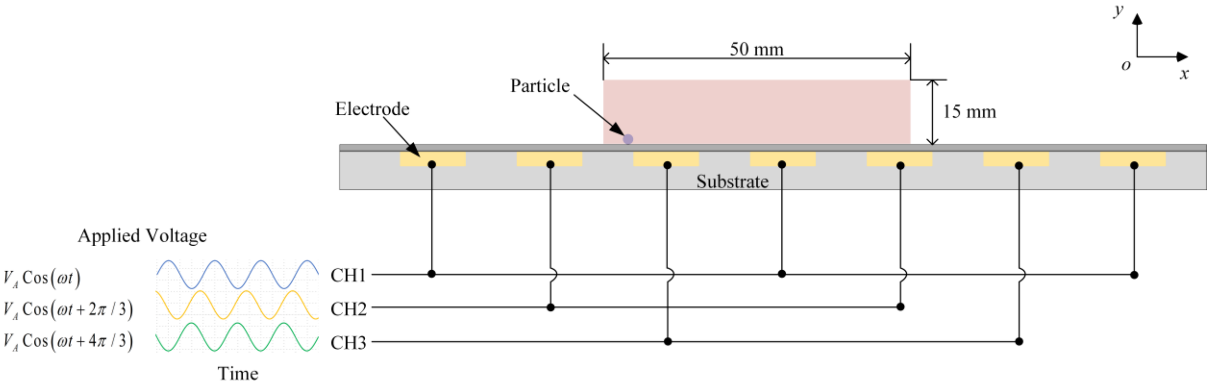

Fig. 5.5 Schematic of operating parameters and system configuration and recording area (pink rectangle).

5.2.2.1 Control of experimental conditions

Due to the sensitivity of triboelectric charging to changes in environmental conditions, some testing experiments were performed in a humidity controlled box to determine the effect of humidity. A Coy Laboratory Products (USA) humidity-controlled glovebox is used to precisely manage environmental conditions. Humidity regulation is achieved through a dual approach involving cobalt chloride desiccant and dry nitrogen purging, maintaining a precise control range of 1% to 95%

relative humidity with an accuracy of ±0.5%. The temperature was set at room temperature, around 20 degrees Celsius.

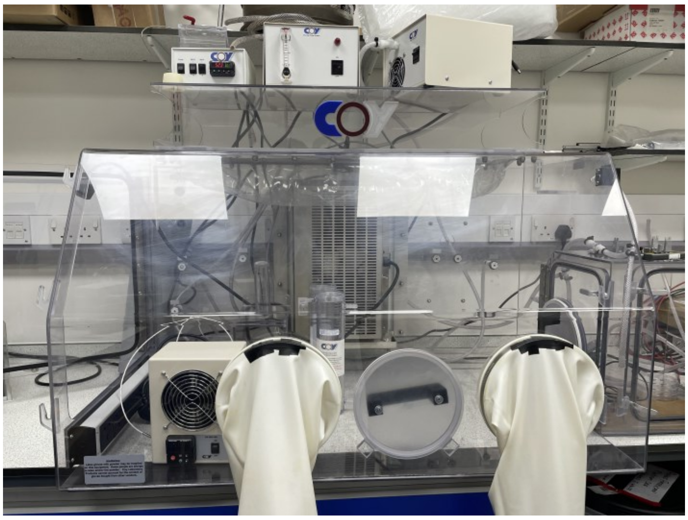

Fig. 5.6 Environmental Control in a Coy Laboratory Products Humidity-Controlled Glovebox

In the experiments, the selection of particles and the operating parameters are as detailed in Table 5-1. The particles used in these experiments were heated before testing to reduce effects of moisture and aggregation. To prevent charge breakdown, the amplitude is limited to 1500 V. In the experimental research, the primary factors under investigation are frequency and particle size.

Table 5-1 List of experiment variables

Parameters	Value	Unit
Applied voltage wave type	Sinusoidal wave	
Applied voltage wave phases	3	
Applied voltage frequency, f	20 to 800	Hz
Applied voltage amplitude, V_A	1500	V
Electrode width, d	1	mm
Electrode pitch, p	2	mm
Electrode length	200	mm
ETW board length	210	mm
Wavelength, λ	6	mm
Particle type	Ballotini, PMMA	
Particle size	30 to 400	µm
Particle polarity	Positive, negative and neutral	
Environment control	Humidity	

5.2.3 Selection of Material

Ballotini was chosen as the primary particle material due to its widespread use in various applications and experimental research. Additionally, its spherical shape and uniform size make it a suitable choice. Four groups of narrow particle size ranges were tested, 30 to 50 µm, 75 to 110 µm, 220 to 280 µm, and 300 to 350 µm. Ballotini particles were bought from VWR company, supplied from Sigmund Lindner GmbH. PMMA particles were also tested. These particles are less dense than ballotini, and their charge is less affected by moisture. PMMA particles were purchased from Cospheric LLC (USA). The properties of the ballotini and PMMA particles are included in appendix C. The comparison of the basic physical properties between ballotin and PMMA particle are in Table 5-2.

Table 5-2 Comparison of properties between Ballotini and PMMA particle

Material	Density (g/cm³)	Relative permittivity	hydrophobicity	Size (μm)
Ballotini	2.5	3.7	hydrophilic	30 to 350
PMMA	1.2	2.8	hydrophobic	250 to 350

5.3 Experimental Procedure

5.3.1 Sample Preparation

Before each experiment, the samples were placed in an oven at 150°C for 4 hours to dry and reduce the impact of moisture, thereby avoiding agglomeration. The particles were kept in a sealed container after removed from the oven to reduce exposure to ambient moisture.

In the experiment of exploring the effect of particle charge, three methods were used to charge or neutralize particles. A stainless steel container was used to shake particles to make them negatively charged, while a PTFE (Polytetrafluoroethylene) beaker was used to charge particles positively. And a neutralizer was used to eliminate the charge on particles. The devices used for the charging process are shown in Fig. 5.7.

(*a*) Stainless steel container

(b) PTFE baker with charged PMMA particles

(c) Static eliminators SIMCO

Fig. 5.7 Photograph of charged containers or neutralizer of three methods.

For each different charging processes, tools such as tweezer used for subsequent particle handling must also be made of the same materials as those used in the charging process to maintain the polarity of particle charge.

The detailed and complete experimental procedure is attached in appendix C.

5.3.2 Data Collection and Analysis

For single particle experiments, the trajectory of a particle is recorded by a high-speed camera. Any positions of particle varied with time can be extracted accurately. The frames extracted from the high-speed camera are further analysed by image processing software, which is Tracker. The quantitative data from the trajectories are average velocity and levitation height. In addition, the particle motion modes and travel direction are important, which are collected as qualitative data. The details for the operation of the software is attached in appendix C.

A schematic of the ETW platform is illustrated in Fig. 5.8. Three-phase high voltage is applied to the electrodes. The wave direction can be controlled by adjusting the phase difference through the function generator. In the all experiments, the three sinusoidal waves were set with an offset of 120 degrees. Selected sample particles fed into the field can be transported either forward or backward.

In the single particle experiments, four key variables were considered: particle type, particle size, particle charge, and frequency of applied voltage. Particle size was categorized into size ranges, including 30 to 50 μm, 75 to 110 μm, 220 to 280 μm, and 300 to 350 μm. For each experiment, a single particle was selected from a specific size group and placed on the board. Upon activating the system with preset frequency parameters, the particle moved in the ETW system, and its trajectory was recorded using the observation system. The average velocity of particle movement was then calculated. Each type of experiment was repeated at least three times for quantitative analysis. If the focus was solely on particle direction, a mobile phone was employed to straightforwardly record the motion directions of particles.

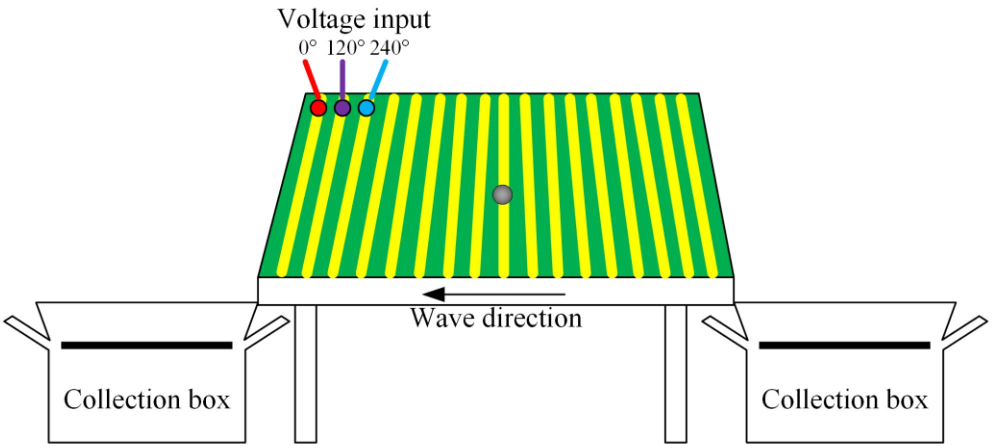

Fig. 5.8 Illustration of the experimental set-up. The yellow bars represent electrodes, which are connected to the three-phase voltage. The dark ball represents an experimental particle.

5.4 Results

The data collection and analysis for the results of single particle experiment are mainly based on the extracted trajectories from high-speed camera videos. The effects of system and operating parameters on particle motion mode, direction and moving speed are analysed. The conclusions are presented as follows.

5.4.1 Particle Motion Mode

The classification of particle motion modes is an effective tool to help understand the basic mechanisms of a particle moving in ETW fields. However, this type of single particle experiments have rarely been performed and the clear trajectories showing the particle moving in different modes are not found in the literatures.

In order to reproduce the different particle motions modes in simulations experimentally, three groups of ballotini particle were used with diameters of 75 to 110 µm , 220 to 280 µm and 300 to 350 µm. The wave direction is set leftward. In the experiments, a mass of 0.5 g of neutralized particles were shaken in a stainless-steel cup for 2 minutes and then a single particle in each group was picked up with stainless steel tweezer and placed on the surface. Then, the high-speed camera was turned on and the pre-set voltage was applied at the same time. In one of the experiments, at the condition of voltage amplitude of 1500 V and frequency of 150 Hz, three motion modes were observed simultaneously.

The superimposed frames are shown in Fig. 5.9. The smallest particle vibrated in a cyclic motion, which was a typical curtain mode. The measured levitation height of the particle in curtain mode is about 1 mm. The superimposed images allow average velocity to be calculated, and found to be approximately 0.056 m/s. As particle mass increases, the increase of the gravitational force makes the particle enter into the hopping mode, shown as the orange trajectory in Fig. 5.9. As the particle size increases further, the gravitational force is larger than the maximum value of electric force on the particle. Therefore, the particle was kept on the surface and it could only roll along the surface in surfing mode due to the horizontal component of the electric forces.

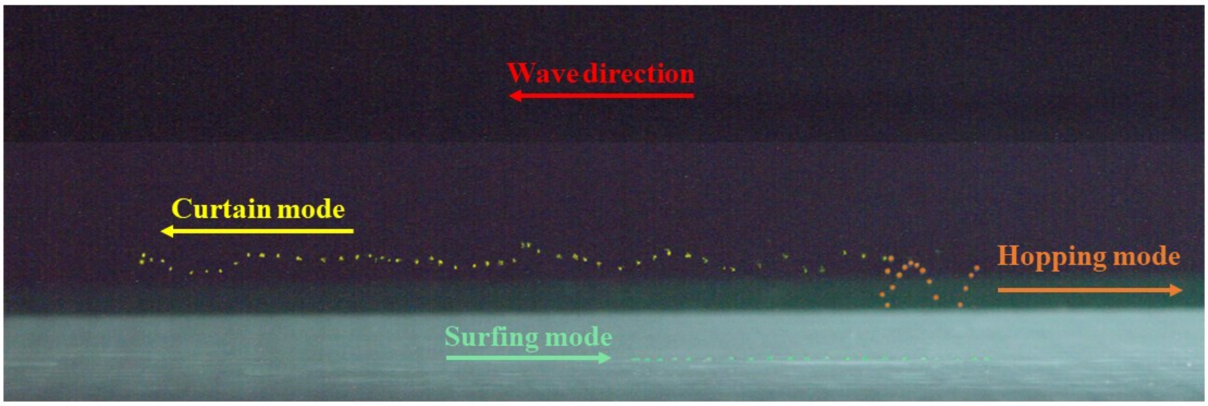

Fig. 5.9 Superimposed frames every 0.056 m/s indicating particle moving trajectories in three different motion modes with different colours.

5.4.2 Particle Motion Direction and Speed

The different motion directions, forward and backward, have been observed for particles in hopping mode and surfing mode experimentally. Backward motion has been observed and suggested that this was due to the second harmonic wave of ETW field [23, 24]. By utilizing the different transport directions, Masuda and coworkers tried to separate biological cells [23]; Machowski and coworkers [28] performed the separation experiments on sand and pulverised alumina powders. In chapter 4, the additional analysis is provided based on the simulation results, which shows that the backward motion is only noticeable when the particle size is large or frequency is high. In this section, the motion direction of large size particle of ballotini and PMMA have been researched and recorded. For the PMMA particle, the effect of whether PMMA is charged or neutralized on particle motion direction is also evaluated.

Fig. 5.10 shows one of the typical motions of ballotini of size between 300 and 350 μm. The images were extracted from high-speed camera videos and superimposed. In the experiment, the voltage amplitude was 1500 V and the frequency was 60 Hz. The wave direction was rightward and the motion direction of the particle was leftward. In the frame capture process, the time interval between each frame was the same, so the time interval was the same. The different distances between the particle points means that the velocity of particle was fluctuating.

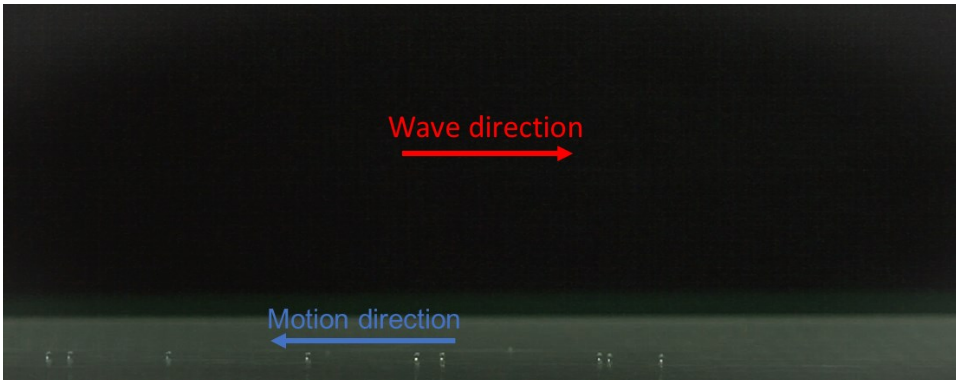

Fig. 5.10 Superimposed frames from high-speed camera video showing surfing mode backward motion of ballotini particle at 60 Hz, 1500 V.

Using the software of Tracker, the variation of particle position with time can be recorded accurately. The recording frame rate is 2134 f/s. Therefore, the particle motion characteristics such as, moving velocity, acceleration, and levitation height can be analysed quantitatively. Part of data processing record is shown in Fig. 5.11. The relationship between the average velocity of particle and wave velocity with frequency is shown in Fig. 5.12. The negative velocities at other frequencies in the range of 5 to 180 Hz mean particle exhibiting backward motion consistently. Wave velocity varies linearly with frequency, with its gradient roughly five times that of particle velocity with respect to frequency change. And there is a prime frequency showing the highest particle speed.

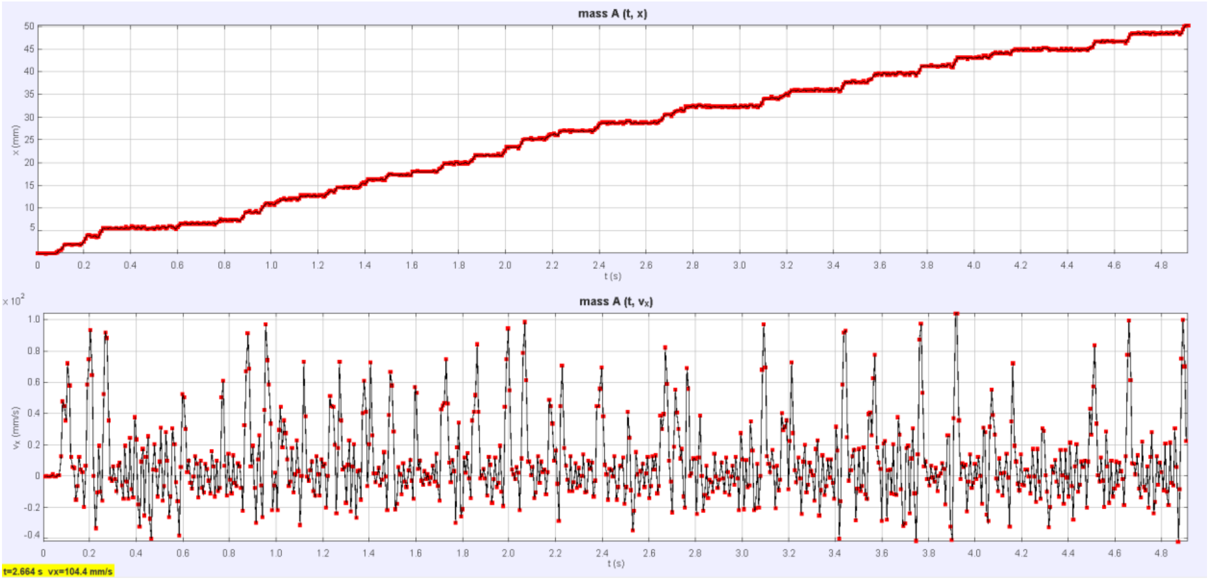

Fig. 5.11 Data processing and record interface in Tracker showing the positions and velocity of the particle at different time (note that some of the position noise results from taking the discrete time derivative).

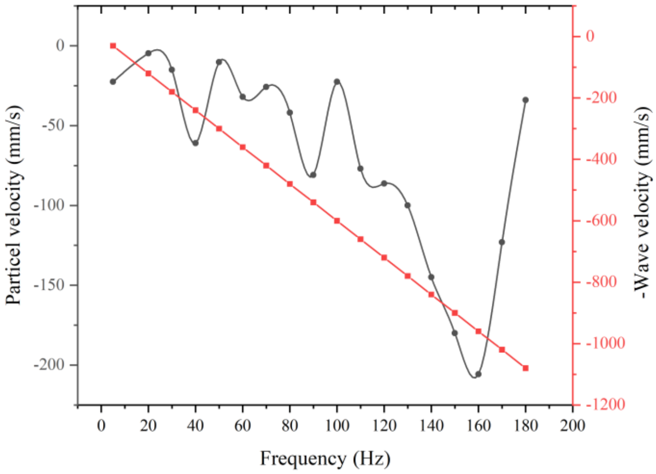

Fig. 5.12 The relationship between particle's average velocity and negative wave velocity with frequency based on single ballotini particle experiments.

The other type of material PMMA has also been tested. The size of PMMA is 280 to 320 µm. Particles with high charge travelling along the wave in surfing mode at 30 Hz and 60 Hz have been recorded and the superposed frames are shown in Fig. 5.13. The recording frame rate was 2134 f/s and the frames were extracted every 60 frames. The time between each frame was 0.028 s. Particle average velocity in surfing mode at 30 Hz and 60 Hz was calculated as 0.17 m/s and 0.36 m/s, respectively. The wave velocity at 30 Hz and 60 Hz was 0.18 m/s and 0.36 m/s, respectively. The close agreement proves the theory in section 4.3.1 that the average velocity of a particle in surfing mode equals the wave velocity.

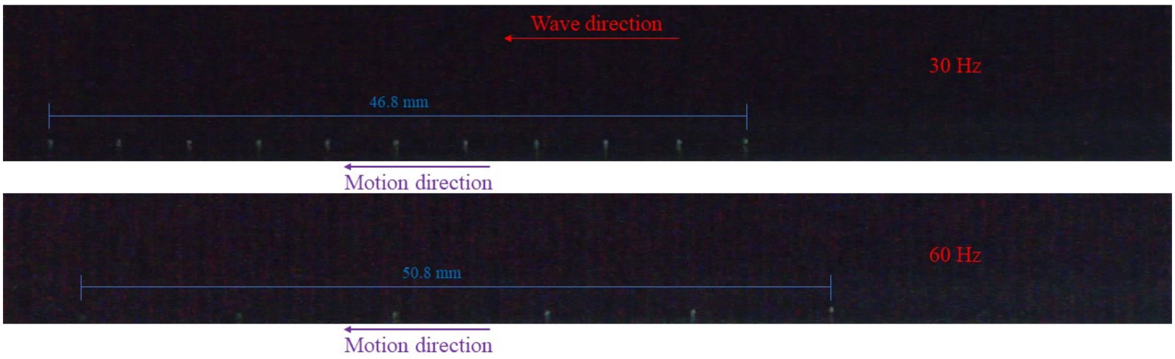

Fig. 5.13 Superimposed frames from high-speed camera video showing surfing mode motion of charged PMMA particle at different voltage frequencies.

The ballotini particle, with its lower charge, readily moves backward, while a charged PMMA particle travelled forward. The charge on the particles was shown to affect the particle motion direction. A static eliminator SIMCO was used to neutralize the PMMA particle on the board before the experiment, shown in Fig. 5.14. The particle moving trajectory was recorded by phone and it showed that particle moved in the backward direction, as seen in Fig. 5.15. The frame rate was 30f/s and the frames were extracted every 2 frames. This may suggest DEP make particle move backward.

The experiments of particle motion have also been conducted in the humidity control box. The set of parameters was introduced in section 5.2.2.1. The results in the box agreed with the results in the air. This means that the humidity and temperature in the room do not significantly affect the particles compared to the conditions in the box. Subsequently, multiple particles transport and separation experiments were conducted under room conditions.

In conclusion, the motion direction can be summarized as:

1. Ballotini particles with size 300 to 350 μm with low charge moved backward;
2. Neutralized PMMA particles with size 280 to 320 μm moved backward;
3. Charged PMMA particles with size 280 to 320 μm moved forward.

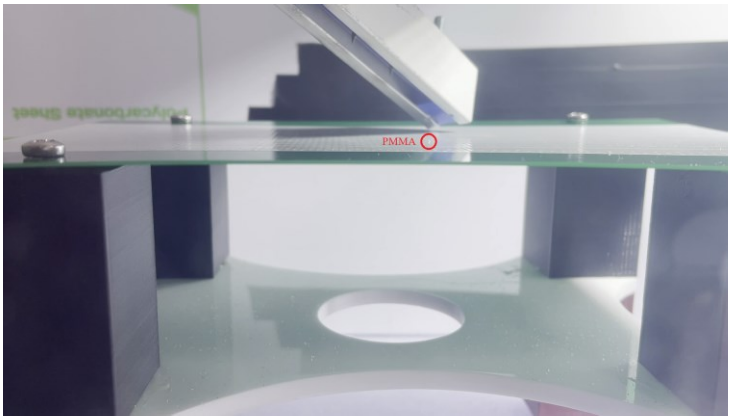

Fig. 5.14 PMMA particle was neutralized by static eliminators SIMCO in the beginning of the experiment.

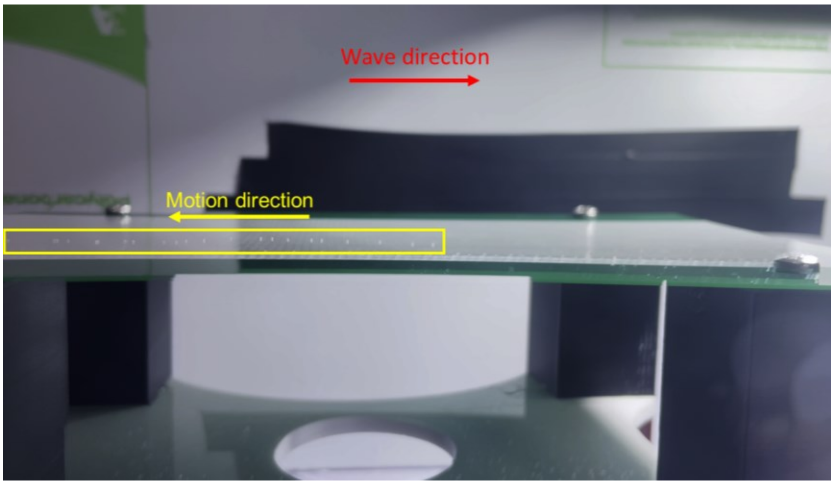

Fig. 5.15 Superimposed frames from phone video showing surfing mode backward motion of neutralized PMMA particle at 60 Hz, 1500 V.

As particle motion is dominated by the combination of the gravitational force and electric forces, such as Coulomb force and DEP, the trajectory of a particle is significantly affected by its charge. Due to the difficulty in strictly controlling particle size, charge, and the irregular shape of particles in experiments, it is challenging to rigorously control and predict the trajectory patterns of particles. It is hard to get precise quantitative conclusions. However, three empirical qualitative and approximately quantitative conclusions can be summarized based on the large number of experiments in terms of motion modes:

1. Only particles with size smaller than 110 µm have chance to enter into curtain mode. This may be due to the difficulty in achieving effective charging of ballotini particles. When the particle size is too large, the Coulomb force is not strong enough to keep the particle levitating above the surface under the action of gravity.
2. Curtain mode motion strictly follows the ETW direction, while hopping mode and surfing mode motion may act against the direction of the ETW. The speed for curtain motion is the slowest.
3. The effect of frequency on particle motion is significant. There is an optimal frequency for the most effective particle movement; frequencies that are too high or too low can hinder particle motion.

5.4.3 Comparison Between Simulation Results and Analytical Results

In Fig. 5.9, the curtain motion trajectory shows that the levitation height of the particle was about 1 mm. The superimposed images allow average velocity to be calculated using the same method in section 5.4.2, and was about 0.056 m/s. By deploying the simulation model in chapter 4, the numerical results of levitation height and average velocity for a particle size in the range 75 to 110 µm is about 1 mm and 0.0095 m/s. The comparison shows that the simulated levitation height agrees well with the experiment results. However, the experimental velocity is much larger than simulation results. This is because experimentally, a particle in curtain mode does not perform a circular motion in each period as in the simulation because of the air flow perturbation and drag. The frame-by-frame experimental result of the curtain trajectory (yellow ball) and the simulated curtain trajectory (brown track) are shown in Fig. 5.16. The measured trajectory illustrates the cyclical motion and move forward quite effectively and the distance that particle travels is about 1/5 of the simulated distance in each cycle. Therefore, the velocity extracted from the experiment is much faster than that of the simulated velocity. According to this proportional relationship, the simulated velocity still can be a reference of realistic motion. However, the actual ratio might be different for different ambient air conditions, plus the size and shape of particles.

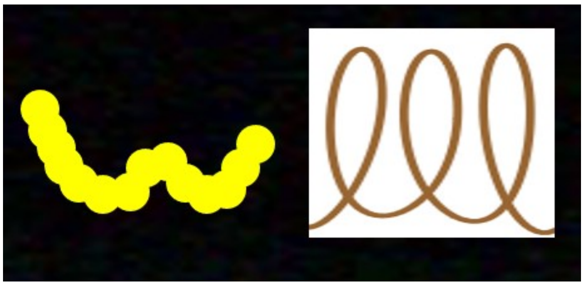

Fig. 5.16 Experiment curtain mode (yellow ball) and simulation curtain mode (brown track).

5.5 Backward Motion Analysis

From the experiments, the backward motion of particles was observed. In the following section, further analysis of this backward motion is given to better understand the mechanisms and assist in the design of a size separation ETW

5.5.1 Particle Motion Direction

The formula for a nonuniform electrostatic travelling field can be expressed as a Fourier series. The higher order terms of Fourier series decay fast so only the first and second terms are of importance and considered. In a 2D model, the electric field generated by three-phase sinusoidal waves in the horizontal and vertical directions can be found [160]:

$$\begin{cases} E_x = V_A\left(\dfrac{3a_1\alpha_1}{2}\sin\left(\alpha_1 x-\omega t\right)\exp\left(-\alpha_1 y\right)+\dfrac{3a_2\alpha_2}{2}\sin\left(\alpha_2 x+\omega t\right)\exp\left(-\alpha_2 y\right)\right) \\ E_y = V_A\left(\dfrac{3a_1\alpha_1}{2}\cos\left(\alpha_1 x-\omega t\right)\exp\left(-\alpha_1 y\right)+\dfrac{3a_2\alpha_2}{2}\cos\left(\alpha_2 x+\omega t\right)\exp\left(-\alpha_2 y\right)\right) \end{cases} \tag{5.1}$$

where V_A is the amplitude of applied voltage, a_1 and a_2 are coefficients dependent on the electrode configuration, $\alpha_n = 2n\pi/\lambda$, λ is the wavelength, ω is the angular frequency, x and y represent the positions on the horizontal and vertical axes of the Cartesian coordinate system. The wave velocity of the first and second wave is ω/α_1 and $-\omega/\alpha_2$, respectively.

The travelling direction of electrostatic wave field is consistent with the dominant first term wave direction. Under the pure perfect single wave, a particle will move along the wave in the same direction.

5.5.2 Effect of Harmonic Wave

The effects of backward harmonic wave on the particle backward motion have been explained in the literature [23, 32, 52, 89]. The simulation results in chapter 4 demonstrated that the addition factors of lower levitation height and higher frequency increased the probability of a particle moving backward due to the action of the harmonic wave. The actual motion direction of particles is determined by the interaction of the two waves. Thus, if the parameters of the field such as frequency and amplitude are adjusted to allow one type of particle to interact with one of the wave streams and the rest with the other, the separation and the transport of the particles can be achieved simultaneously.

5.5.3 Effect of Dielectrophoresis

The term “dielectrophoresis” (DEP) was coined by Pohl [18] in the research of precipitation suspensoids in fluids. In this case, the effect of DEP becomes important for relatively large particles with low charge.

According to the theory of calculating DEP [139], the dipole moment of a particle in the field is calculated as:

$$\boldsymbol{m} = m_x(t)\boldsymbol{a_x} + m_y(t)\boldsymbol{a_y} \tag{5.2}$$

where:

$$\begin{aligned}
m_x(t) &= -4\pi\varepsilon_m r^3 \frac{3a_1\alpha_1}{2}\exp(-\alpha_1 y)\left|f_{CM}\right|\sin(\omega t - \alpha_1 x - \varphi_m) \\
&+4\pi\varepsilon_m r^3 \frac{3a_2\alpha_2}{2}\exp(-\alpha_2 y)\left|f_{CM}\right|\sin(\omega t + \alpha_2 x - \varphi_m) \\
&= -4\pi\varepsilon_m r^3 \frac{3a_1\alpha_1}{2}\exp(-\alpha_1 y)\left\{\mathrm{Re}[f_{CM}]\sin(\omega t - \alpha_1 x) + \mathrm{Im}[f_{CM}]\cos(\omega t - \alpha_1 x)\right\} \\
&+4\pi\varepsilon_m r^3 \frac{3a_2\alpha_2}{2}\exp(-\alpha_2 y)\left\{\mathrm{Re}[f_{CM}]\sin(\omega t + \alpha_2 x) + \mathrm{Im}[f_{CM}]\cos(\omega t + \alpha_2 x)\right\}
\end{aligned} \tag{5.3}$$

$$\begin{aligned}
m_y(t) &= 4\pi\varepsilon_m r^3 \frac{3a_1\alpha_1}{2}\exp(-\alpha_1 y)\left|f_{CM}\right|\cos(\omega t - \alpha_1 x - \varphi_m) \\
&+4\pi\varepsilon_m r^3 \frac{3a_2\alpha_2}{2}\exp(-\alpha_2 y)\left|f_{CM}\right|\cos(\omega t + \alpha_2 x - \varphi_m) \\
&= 4\pi\varepsilon_m r^3 \frac{3a_1\alpha_1}{2}\exp(-\alpha_1 y)\left\{\mathrm{Re}[f_{CM}]\cos(\omega t - \alpha_1 x) - \mathrm{Im}[f_{CM}]\sin(\omega t - \alpha_1 x)\right\} \\
&+4\pi\varepsilon_m r^3 \frac{3a_2\alpha_2}{2}\exp(-\alpha_2 y)\left\{\mathrm{Re}[f_{CM}]\cos(\omega t + \alpha_2 x) - \mathrm{Im}[f_{CM}]\sin(\omega t + \alpha_2 x)\right\}
\end{aligned} \tag{5.4}$$

And $\boldsymbol{a}_x$ and $\boldsymbol{a}_y$ are unit vectors along the x and y axes. ε_m is the relative dielectric permittivity, *r* is the particle radius, and f_{CM} is the Clausius-Mossotti factor:

$$f_{CM} = \frac{\varepsilon_p^*(\omega) - \varepsilon_m^*(\omega)}{\varepsilon_p^*(\omega) + 2\varepsilon_m^*(\omega)} \tag{5.5}$$

where ε_p^* and ε_m^* are the complex dielectric permittivity of particle and medium, which are related to angular frequency (ω) of the electric field. The complex permittivity is given as:

$$\varepsilon^* = \varepsilon - \boldsymbol{i}\sigma / \omega \tag{5.6}$$

where σ is the conductivity, and $\boldsymbol{i}^2 = -1$.

The time-dependent DEP is calculated as:

$$\boldsymbol{F}(t) = F_x(t)\boldsymbol{a}_x + F_y(t)\boldsymbol{a}_y \tag{5.7}$$

where:

$$F_x(t) = m_x(t)\frac{\partial E_x(t)}{\partial x} + m_y(t)\frac{\partial E_x(t)}{\partial y} \tag{5.8}$$

and

$$F_y(t) = m_x(t)\frac{\partial E_x(t)}{\partial y} + m_y(t)\frac{\partial E_y(t)}{\partial y} \tag{5.9}$$

The time-dependent DEP in the *x* direction is simplified in the form associated with real part Re[f_{CM}] and imaginary part Im[f_{CM}], respectively:

$$\begin{aligned} F_x(t) &= m_x(t)\frac{\partial E_x(t)}{\partial x} + m_y(t)\frac{\partial E_x(t)}{\partial y} \\ &= -18\pi\varepsilon_m r^3 \,\mathrm{Re}\left[f_{CM}\right] a_1 a_2 \alpha_1^{\,3} \exp(-3\alpha_1 y)\sin(\alpha_1 x + 2\omega t) - \\ &\quad 9\pi\varepsilon_m r^3 \,\mathrm{Im}\left[f_{CM}\right]\alpha_1^{\,3}\exp(-4\alpha_1 y)\cdot \\ &\quad \left\{8a_2^{\,2} + a_1\exp(\alpha_1 y)\left[4a_2\cos(3\alpha_1 x) + 2a_2\cos(2\alpha_1 x - 2\omega t) + a_1\exp(\alpha_1 y)\cos(2\alpha_1 x - 2\omega t)\right]\right\} \end{aligned} \tag{5.10}$$

The ETW field generates both travelling DEP and standing DEP, which are associated with Im[f_{CM}] and Re[f_{CM}], respectively. It usually defines the phase-dependent portion of the field as travelling DEP. The relationship between the value of Re[f_{CM}] and Im[f_{CM}] at the frequency of 100 Hz, and conductivity of a particle in air is shown in Fig. 5.17. Because the conductivity of glass is smaller than 10^{-13} S/m, the Im[f_{CM}] is much smaller than Re[f_{CM}] for a glass particle in air. As a result, only the component of DEP associated with the real part of Clausius-Mossotti factor is considered.

The wave velocity of the standing DEP is $-2\alpha_1/\omega$. The negative velocity means the DEP is directed backward, which definitely contributes to the backward motion of particles. The travelling direction of DEP can also be found from the plots of DEP on the 0.2 mm glass particle in the *x* direction at a height of $y = 0.2$ mm at different time in a period of T (0.02 s) in Fig. 5.18.

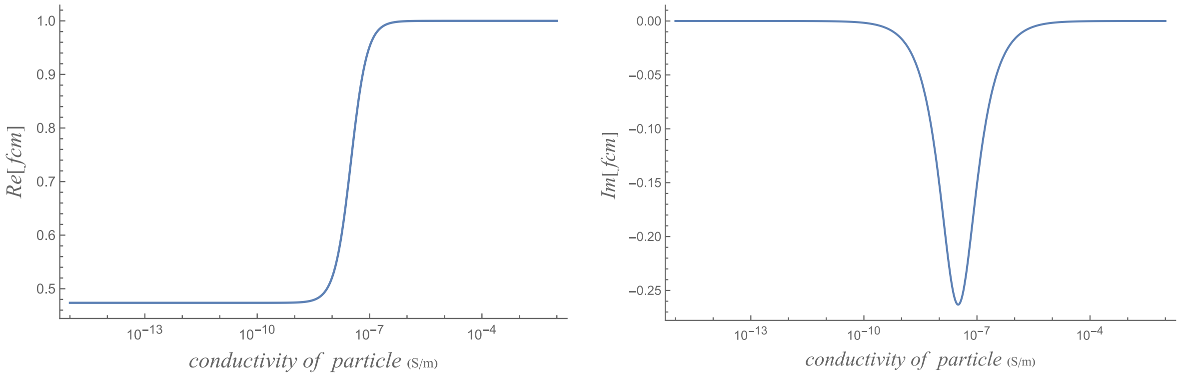

(*a*) Real part value of f_{CM} (b) Imaginary part value of f_{CM}

Fig. 5.17 DEP in the *x* direction.

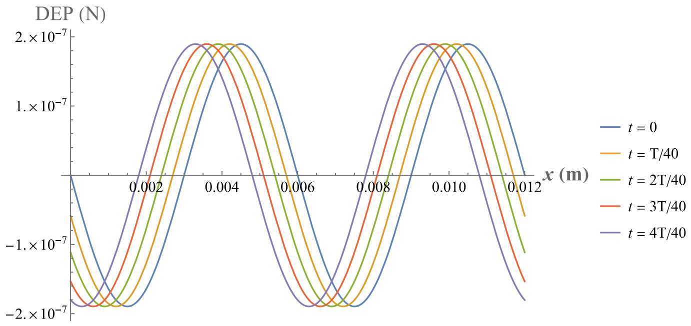

Fig. 5.18 DEP induced motion in the *x* direction for a 0.2 mm glass particle size.

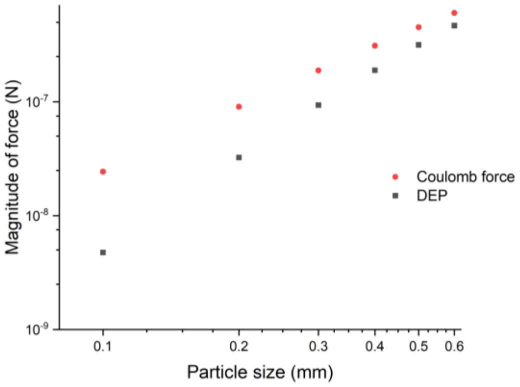

Fig. 5.19 Comparison of the maximum forces on particle with different sizes.

Assuming a particle with a charge of 1% of the saturation charge is at any positions on the board, Fig. 5.19 compares the peak value of DEP and Coulomb forces acting on it with various sizes. The saturation charge is calculated by the relation of Pauthenier [152], which is directly proportional to the square of particle size. According to formula (5.10), $F_{\mathrm{dep}} \propto r^3$, so DEP is volume related. While the forces are of a similar magnitude, the DEP becomes more dominant as the particle size increases. The analysis of comparison between DEP and Coulomb force explained the reason for the backward motion of poorly charged particles. This balance between DEP and Coulomb force is a function of particle size also suggesting that separation of particles by size is possible.

5.6 Limitations and Conclusions

5.6.1 Limitations

Due to constraints imposed by both environmental factors and technological limitations, the experiments are subject to certain limitations.

1. The particle sizes vary within a range and are not strictly uniform and spherical, which may pose challenges for quantitative analysis.
2. Measuring the charge on a particle, particularly for small single particles, is challenging and imprecise. Additionally, the particle charge may undergo significant variations when exposed to the ambient environment. The difficulty in controlling the charge quantity may increase the challenges of obtaining stable results in the experiments.
3. The simulation model is simplified as 2D by assuming the electric field remains constant along the length of the electrode. In realistic experiments, edge effects around the board disrupt the normal distribution of the electric field, resulting in unexpected phenomena compared to the simulation results.

The first two limitations primarily affect the single particle experiment. The presence of uncertainties in experimental data poses a challenge in achieving quantitative analysis. Attempts to acquire a more comprehensive understanding of the particle motion mechanism become difficult under these conditions. Therefore, the analysis of the results in single particle movement inclined towards obtaining qualitative conclusions. In multi-particle experiments, the overall performance of particle transport and separation was the main focus. The collective performance helps average out the effects of individual particles with varying charges and sizes. Additionally, incorporating a 3D simulation approach would be required to address the edge effects in transport and separation.

5.6.2 Conclusions

This chapter presents the experimental results of single-particle trajectories in ETW fields. The analyses of the results focus on the three aspects: particle motion mode, motion direction and speed. Three motion modes were observed clearly, and shown as superimposed frames. Data was extracted for particle average velocity and levitation height in curtain mode and surfing mode. These data were compared with simulation results, which confirmed the validity of simulation model.

An important experimental phenomenon was the backward motion exhibited by large particles of ballotini in hopping and surfing mode. To better understand the mechanism of backward motion, subsequent experiments and measurements on PMMA particles were done. The moving velocity and direction for charged and neutralized PMMA particle were compared. Charged PMMA particles travelled along the ETW wave, while neutralized ones moved backward. This reveals the effect of DEP on the backward movement of particles.

The mathematical formulas for the rigorous determination of the dielectrophoretic force were derived. The analysis on the effect of DEP by comparing the maximum forces on ballotini particle with different sizes was provided, which proves that the DEP becomes more dominant as the particle size increases. Therefore, large particles with low charge more easily move backward.

DEP is volume related. Additionally, the influence of frequency varies in proportion to the size of particles. Therefore, different sizes of particles can potentially be separated by their different motion directions at a proper designed frequency. This will be explored in the following chapter.

Chapter 6 Multi-Particle Experiments: Transport and Separation

6.1 Introduction

This chapter demonstrates that ETW can be used to separate particles by size. An ETW experimental system was developed to study particle transportation. The methodology for three type of experiments are introduced, which aims to test the transport ability of the ETW system, research the effect of particle size and frequency on particle transport direction, and particle separation experiment by size, respectively. Four distinct particle size groups were used.

In the research of relationship between particle transport direction and particle size and frequency, the particles were transported either forward or backward and collected in bins at the ends of the apparatus. The collected mass was measured in both forward and backward directions plus the particles remaining on the array. Each of these particle cohorts were analysed by size. The fraction of particles transported in each direction could be quantitative analysed, which exhibited a noticeable frequency-dependent effect. At lower frequencies, a majority of particles moved forward, but as the frequency increased, the fraction of particles being transported backward increased.

Two lines in the plots indicated the mass fraction of particles of each size range cohort collected in forward and backward directions as a function of frequency. These plots exhibited a crossover point. The frequency corresponding this point is defined as "crossover" frequency, which means a particle has an equal likelihood to move forward or backward. The crossover frequency decreases as the particle size increases.

The experimental results show that larger particles tend to move backward at lower frequencies, at which frequency smaller particles may still move forward effectively. Using the single size transporting data, the size concentration of a mixture of different sizes of particles in forward and backward directions could be estimated. The separation performance of particles of various sizes at different frequencies is predicted.

Finally, a mixture of different sizes of 30 to 50 μm and 75 to 110 μm particles were tested and show satisfactory separation performance. The mass recovery of each size of particle in forward and backward directions match well with the estimation of the mass recovery using the single size particle transport experiment results.

6.2 Methodology

Three types of experiments have been conducted to explore multiple particles transport and separation. The first type involves assessing particle transport capability to determine the maximum dust or particle mass transport of the ETW system. The second type focuses on examining the fraction of particles within a single size group transported in both forward and backward directions across varying frequencies, elucidating the correlation between transport direction, particle size, and frequency. These findings facilitate the prediction of particle separation performance in mixtures of different sizes. The third and final experiment type involves particle size separation at different frequencies.

The three types of experiments have different purpose, so their methodologies differ in various aspects, including the selection of variables, the way of feeding particle, data collection and analysis. The subsequent section will individually outline them. The ETW board used in the experiments is the same as in chapter 5.

6.2.1 Particle Transport Ability

In the experiments, two groups of particle size were used: 75 to 110 μm and 220 to 280 μm. The particles contained in a plastic petri dish were poured onto the surface of the board manually and slowly. The resulting thickness was recorded as *h*, as shown in Fig. 6.1. Increasing the initial mass will result in a thicker pile. Three mass groups were selected: 5, 10, and 20 g. A frequency of 20 Hz was chosen for operation, as particles could be transported efficiently at this frequency. After placing the particles on the surface of the ETW system and measuring the thickness of pile, the system was activated. The slew rate of the voltage amplifier is larger than 40 V/μs. The charge time to 1500 V is less than 40 μs. It is assumed that the high voltage is instantly applied to the board. The total transport time was recorded and the mass of the collection of particles was measured. The transport efficiency was defined as the ratio of the mass of collected particles to initial mass to evaluate the transportability of the system.

Fig. 6.1 Measurement of the thickness *h* of tested particle on the ETW board.

6.2.2 Particle Transport in Forward and Backward Directions

In the experiments, the mass of particles being used to assess their transport is measured before initialising the ETW system. The sample preparation follows the same procedure as outlined in section 5.3.1, and no prior charging of the samples is required. Then, the system is activated with preset parameters of voltages. The initial state of the particles is set up by having a mass (m_i) of particles, then they are slowly released to free-fall from a plastic petri dish at a height of 10 mm above the board in the middle of the platform. Under the action of ETW fields, the system transports the particles across the surface to be collected in the containers on each end. The mass of the collected particles in the forward direction and backward direction are weighed and recorded as m_f and m_b. In the experiment, the mass of the particles remaining on the board is also measured and recorded as m_s. Because a few particles may be transported away from the other two sides of the board, the sum of m_f, m_b and m_s is slightly smaller than 100%. The forward and backward recovery rate is calculated as $R_f = m_f/m_i$ and $R_b = m_b/m_i$, respectively. The sum of m_f, m_b and m_s represents the total particles that can be controlled. Controlled particles refer to the particles that can be manipulated, either by collecting them in the forward or backward direction or remaining on the board.

Four distinct particle size groups were used, which are 30 to 50 µm, 70 to 110 µm, 220 to 280 µm, 300 to 350 µm. The lowest and highest frequency applied on each group are listed in Table 6-1. As particle size increases, the maximum frequency for effective particle transport decreases. Each data point was obtained through a minimum of six repetitions of the experiment.

Table 6-1 Frequency range for different size groups of particles

Size (µm)	30 to 50	70 to 110	220 to 280	300 to 350
Lowest frequency (Hz)	20	20	20	20
Highest frequency (Hz)	700	500	200	200

6.2.3 Particle Separation

In the separation experiments, two groups of particles were selected: 30 to 50 µm and 75 to 110 µm. The mass of each group was 0.5 g. The size distribution of the two groups of particles were measured by the Mastersizer, shown in Fig. 6.2, from Malvern Panalytical, for size distribution analysis. The Mastersizer measures particle size distribution using laser diffraction. The results are typically presented as the percentage of particles within each size range. Fig. 6.3 shows the size distribution of the two groups of ballotini particles.

In each experiment, 0.5 g of each group were mixed and dropped from the petri dish into the board. Particles moved under the action of ETW fields. The mass of the particles collected in the forward and backward bins were measured and the size distribution of each collection were analysed again by the Mastersizer. In addition, a 50 µm sieve was used to separate particles from the forward and backward collection trays, respectively. The results show the fractions of fine and coarse particles collected in both forward and backward directions, providing a basis for comparison with the estimated particle separation performance.

Fig. 6.2 Photograph of the Mastersizer. This apparatus is used for the analysis of particle size distribution.

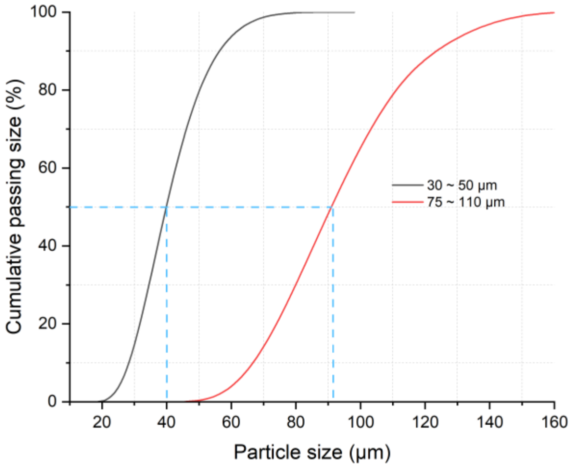

Fig. 6.3 Size distribution of the original sample of two size groups: 30 to 50 μm and 75 to 110 μm.

The experiments were repeated at least three times. In order to demonstrate the randomness of the presented data, the first and second run trials of each type of experiment were selected for presentation and analysis.

6.3 Results and Discussion

6.3.1 Particle Transport Ability

Transport of particles were tested with initial quantities ranging from single layers to small piles. On a sufficiently large surface, particles could be transported relatively easily if they were distributed in a single layer, regardless of their quantity. However, when particles clustered together to form a pile, the low electric field force acting on the top particles and the pressure exerted by the top particles on those beneath them might become obstacles that affect particle motion.

The transport results of piles of particles are shown in Table 6-2. Even if the thickness was about 18.5 mm for the particles from 220 to 280 μm, over 88% of the particles could be effectively transported. When the thickness is small, the electric field intensity remains high and the top particles experience enough electric force to make them move. If the thickness is increased, the electric force on the top particles is low. In this case, the particles at the bottom edge of the layer will start moving first, creating a gap. The particles above will slide down close to the surface and then continue moving. The motion is initiated from the outer edges. Therefore, as long as there is strong flowability among the particles, they will move effectively regardless of the thickness of the particle pile.

Table 6-2 Data record of the transport

Particle size (μm)	75 to 110			220 to 280		
Initial mass (g)	5	10	20	5	10	20
Thickness (mm)	8.5	10.5	13	11	13.5	18.5
Transport time (s)	100	130	210	85	114	201
Collection (g)	4.9	9.9	17.6	4.6	9.2	17.7
Transport efficiency (%)	98%	99%	88%	92%	92%	85.5%

6.3.2 Mass Measurement of Particle Transport in Forward and Backward Direction

In this type of experiment, four groups of particle size were tested individually, 30 to 50 μm, 75 to 110 μm, 220 to 280 μm, and 300 to 350 μm. The relationship between the recovery rate and frequency of each size group is shown in Fig. 6.4. The initial mass $m_{i,}$ in each case was 0.2 g. The experiments were repeated at least 6 times at each data point and the error bars represent the 95% confidence interval of the mean. Recovery rate indicates the fraction of particle collected from original feed. In the experiments, The particles were collected from their final position and the recovery rate were calculated and represented as the black and red points, respectively. The fraction of particles that remained on the board were represented by the blue points. The recovery rate of total controlled particles, represented by the green points, refers to the particles that can be manipulated, either by collecting them in the forward or backward direction or keeping them on the board, which is the sum of the forward, backward and on the board.

These data points are connected by a spline line fit. There is a crossover point where the forward and backward recovery rate lines intersect. The frequency corresponding to this point is defined here as the crossover frequency. At this frequency, a particle is equally likely to move along or against the travelling wave.

From Fig. 6.4, it is clear that a very large mass fraction of particles move in the forward direction at low frequencies. As the frequency increases, the fraction of particles being transported backward increases. In addition, at high frequencies, it can be seen that the amount of particles remaining on the board increases, indicating that the ability of the electrostatic travelling wave to transport particles from their initial positions decreases. Additionally, the total controlled fraction of particles, indicated by the green line, decreases as particle size and operating frequency increase. This indicates that an increasing number of particles flow from the sides of the board rather than in the forward or backward direction. This phenomenon may be attributed to the DEP effect, wherein variations in the electric field near the board edges induce strong DEP and particle movement.

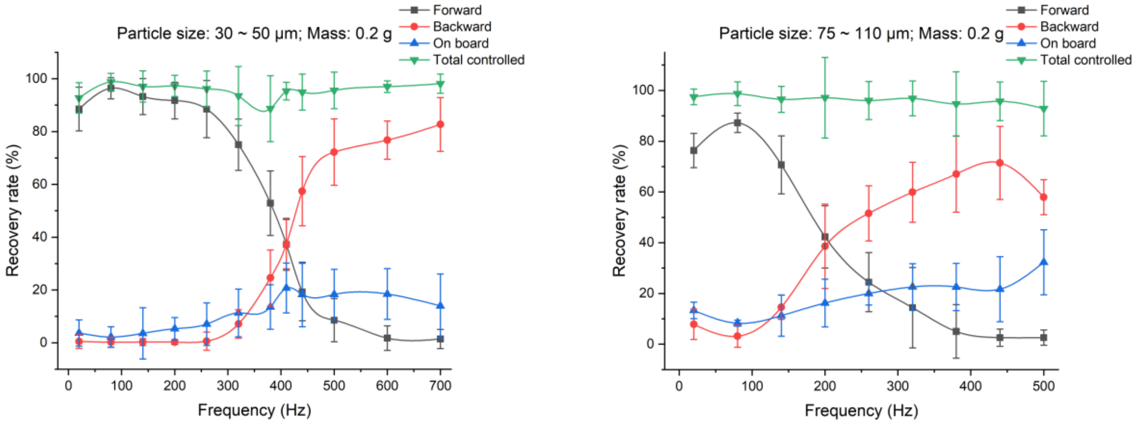

(*a*) Particle size: 30 to 50 µm (b) Particle size: 75 to 110 µm

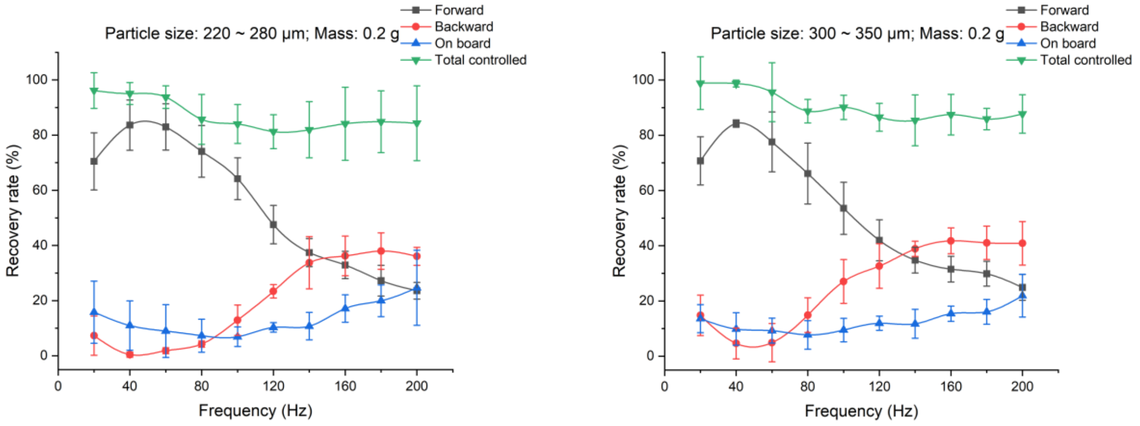

(c) Particle size: 220 to 280 µm (d) Particle size: 300 to 350 µm

Fig. 6.4 Relationship between the transport (recovery with confidence interval) and frequency.

Here it needs to be clarified separately that in single particle experiments, the large particle (300 to 350 µm) exhibits backward motion even at low frequencies, as shown in the results of Fig. 5.12. In multiple particles experiments, the overall direction of motion of particles is forward at low frequencies. This is because of collisions and tribocharging effect between particles, causing particles to become charged during collision processes. Under the influence of Coulomb force, particles still move forward. Only when the frequency increases does the influence of DEP and harmonic waves increases. These factors led to the difference for single particle experiments and multiple particles experiments.

The scatter plot of the relationship between the crossover frequency and the inverse of the mean particle size for each size group is shown in Fig. 6.5. The crossover frequency decreases as the particle size increases. A linear regression line in Fig. 6.5 (*a*) adequately describes the relationship:

$$f = \frac{0.125}{D} + 91.4 \tag{6.1}$$

where D is the diameter of the particle. The Pearson correlation coefficient is 0.995. The linear-logarithm plot in Fig. 6.5 (b) does not imply a exponential relationship.

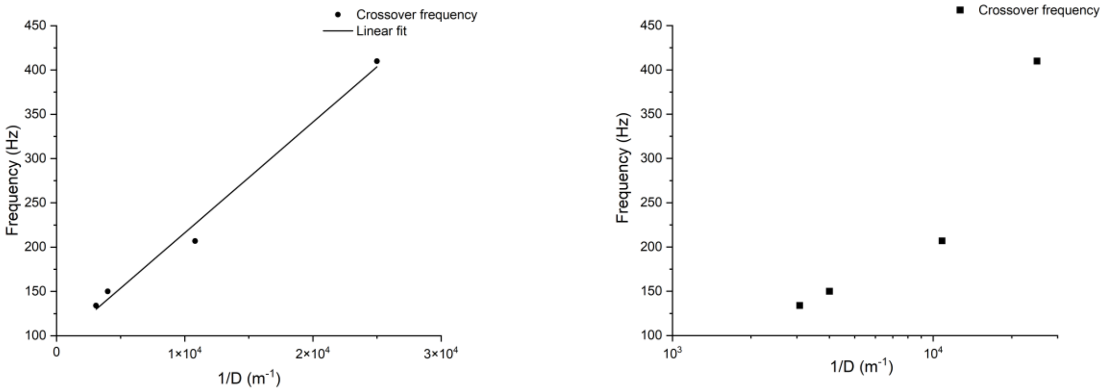

(*a*) linear-linear plot (*b*) linear-logarithm plot

Fig. 6.5 Relationship between the crossover frequency and the reciprocal of particle diameter.

The formula implies that D×(f−91.4) = 0.125. The unit of this number is velocity in terms of dimensional perspective, which could be regarded as a fixed velocity. The main forces affecting particle motion are Coulomb force, DEP, air drag force and gravitational force. The shift of frequency may be related to DEP. Assuming there is a connection between the fixed velocity (v_f = 0.125 m/s) and system parameters:

$$v_f = \zeta \frac{E_0 q_0}{\varepsilon_p \pi \eta \lambda} \tag{6.2}$$

where E_0 represents the maximum electric field, q_0 represents the average charge of particles and ζ is the empirical coefficient. ε_p is the relative permittivity of particle, η is the viscosity of air and λ is the wavelength. In the experiments, E_0 and q_0 are approximated as 4.6×10^6 V/m and 6.5×10^{-14} C. Therefore, ζ would be 0.5. The increase of electric field or charge of particles increases the fixed velocity, and therefore increases the crossover frequency for a certain size of particle group. The validity of the formula has not been confirmed, which needs to be verified through additional experimental data. And the research of the fixed velocity may be a topic for future study.

The forward and backward recovery rate lines of four groups of sizes in the plots of Fig. 6.4 are combined in Fig. 6.6. It is evident that the proportion of forward and backward motion for particles of different sizes may exhibit significant differences at the same frequencies. This suggests that it is possible to separate particles with different sizes in terms of direction of transport by selecting appropriate frequencies.

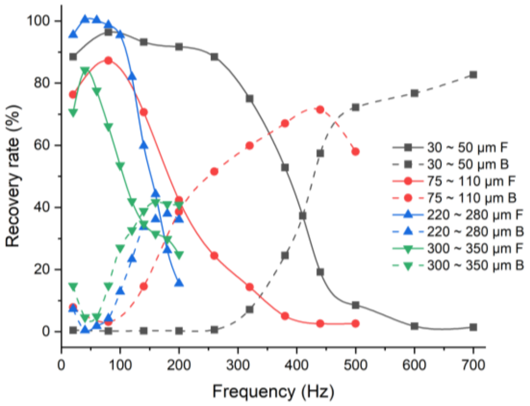

Fig. 6.6 Relationship between the transport (average recovery) and frequency for four different size groups of particles.

6.3.3 Prediction of Particle Size Separation

If a mixture of particles behaves in a manner similar to that as predicted and measured with single particle size groups, the forward and backward collection rates can be predicted. Consequently, size sorting performance can be predicted.

The particles of larger size tend to move backward at lower frequencies, at which frequency the small particles may still move forward effectively. Therefore, transporting the mixture at appropriate frequencies cause small particles to concentrate in the collection box in the forward direction, and larger particles to concentrate in the backward collection. Fig. 6.7 shows the prediction of the separation performance for the mixture of size groups of 30 to 50 μm and 75 to 110 μm with equal initial mass as a function of frequency. The data points are calculated by the mean data points of the single size class transport runs. Fig. 6.7 (*a*) depicts the relationship between the recovery rate and concentration of fine particles (30 to 50 μm) with frequency in the forward collection. Concentration of fine particles represents the proportion of collected small particles in the total collected substance. Meanwhile Fig. 6.7 (b) pertains to the coarse particles (75 to 110 μm), and in the backward direction.

In the size sorting process, both the recovery rate and concentration of fine particles are predicted to reach levels higher than 75% when the frequency range is from 240 Hz to 320 Hz. In the backward collection, the concentration of coarse particles remains very high, larger than 90%, at the frequency from 20 Hz to 320 Hz. This is because the small particles move very effectively forward at low frequencies and only coarse particles move backward. The recovery rate of coarse particles in the backward collection is also minimal at low frequencies. As the frequency increases, the recovery rate of coarse particles increases. In the frequency range of 320 to 425 Hz, the recovery rate and concentration for coarse particles in the backward collection can be larger than 60%.

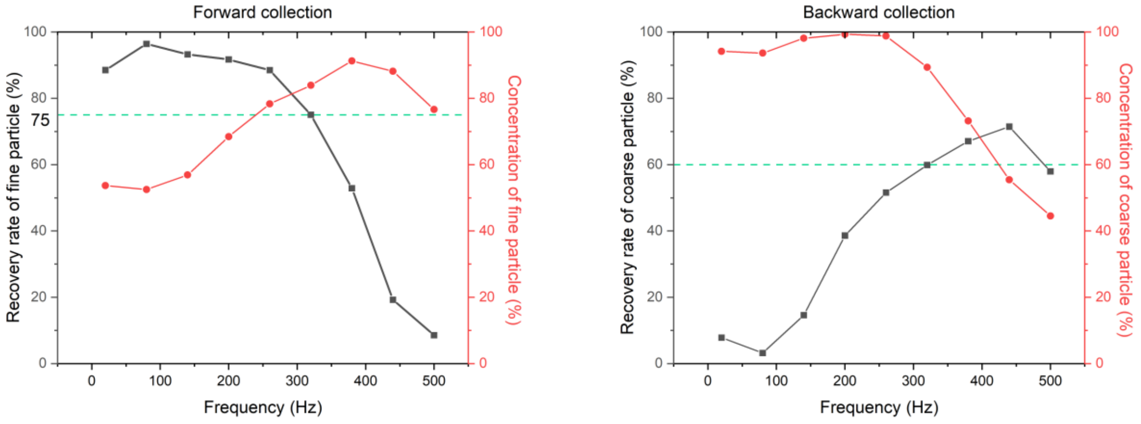

(*a*) Fine particle in the forward collection (b) Coarse particle in the backward collection

Fig. 6.7 Estimation of particle separation performance at different frequencies from single size transport experiment.

Based on the same dataset, the scatter centre plot is shown in Fig. 6.8. The region in the top right quadrant has both high recovery rate and concentration for fine and coarse particles. From this chart the appropriate frequencies for the given mixture could be evaluated.

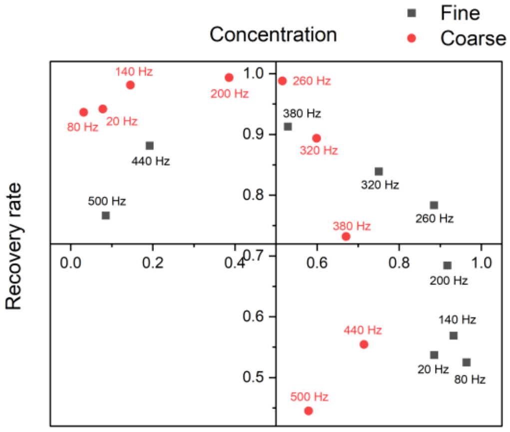

Fig. 6.8 Relationship between the separation results of the recovery rate and concentration of particles with the frequency.

6.3.4 Particle Separation Experimental Results

Based on the estimation of separation performance of Fig. 6.8 in section 6.3.3, the operating frequency from 260 to 380 Hz works well for both fine and coarse particles. An operating frequency of 350 Hz was tested. The size distribution in the forward and backward collection of the first and second run of experiments, represented by different lines (1st run and 2nd run), are compared in Fig. 6.9. Backward collection is nearly the same as coarse particle size distribution, which represent the effective separation of coarse particles from the mixture. Forward collection size distribution tends toward fine but is coarser than the initial fine sample particle size distribution. The separation of small particles is acceptable, but not as good as the coarse particles. This was because some larger particles moved into the forward collection. The close agreement of the results of different runs of experiments shows a strong reproducibility.

A 50 μm sieve was used to separate particles in the forward and backward collection trays. In Fig. 6.10, the measured mass of the fine and coarse particle are displayed. These results also show good separation performance. From Fig. 6.7, the estimation of particle separation performance of the concentrations for the size group 30 to 50 μm and 75 to 110 μm are 82% and 87%, respectively. The recovery rate for the size group 30 to 50 μm and 75 to 110 μm are 64% and 65%, respectively. The experiments results agree well with the estimations. The concentration of large particles in the experiment is a little lower than the prediction. It might originate from the inherent fluctuation errors in the experiment.

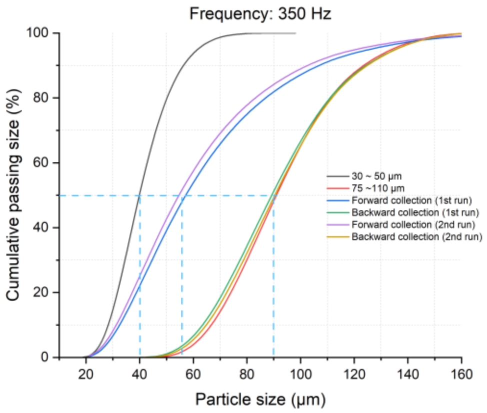

Fig. 6.9 Particle separation results at 350 Hz.

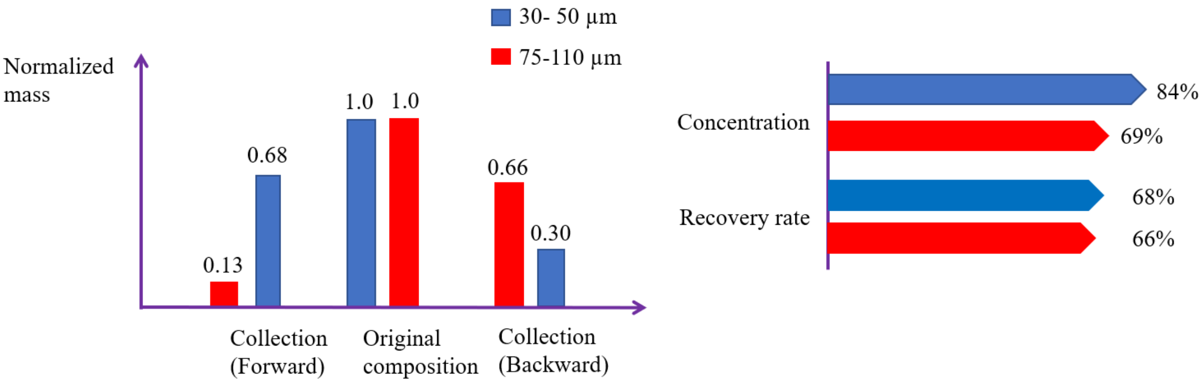

Fig. 6.10 Mass distribution of different sizes of particle in forward and backward collection.

The separation processes were also tested at of 250 Hz and 450 Hz. The results are shown in Fig. 6.11 and Fig. 6.12. At the lower frequency, forward collection was coarser than at 350 Hz suggesting more coarse particles move forward. This was because at lower frequencies, smaller particles were more likely to move forward. In this way, small size particles rarely moved backward, and the backward box could collect nearly pure large particles. However, in the forward direction, more larger particles may also be collected at lower frequency, so the separation for small size particles in the forward direction was poor.

Likewise, at higher frequencies, the forward collection could enhance recovery for smaller sizes, while the backward collection showed reduced recovery for larger sizes. Therefor, at high frequency, there were more fines in the coarse stream.

In each experiment, the total mass of the particles in the forward collection and backward collection were also measured, which was plotted in Fig. 6.13 with confidence intervals. In addition, the estimation of the mass of the total collected particles using the single narrow size group of particle transport results is shown in the red line for comparison. They show close agreement. This confirms that mixing particles with relatively large size difference does not significantly affect the inherent directional characteristics of particle motion. The transport results of four groups of particle sizes can serve as a guide for selecting the appropriate separation frequency.

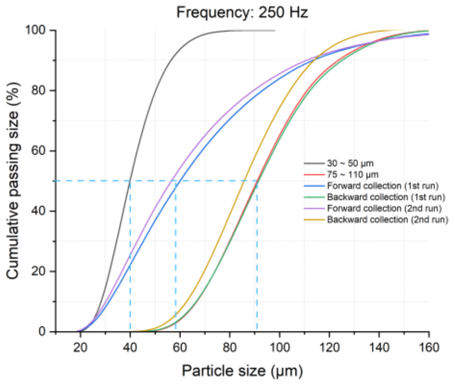

Fig. 6.11 Particle separation results at 250 Hz.

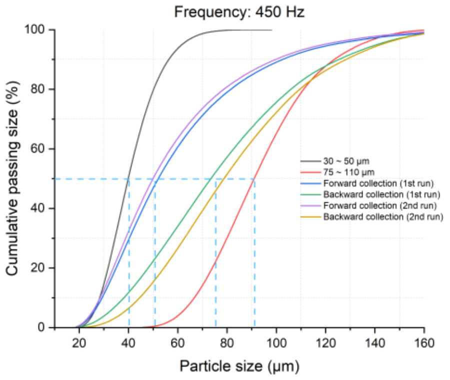

Fig. 6.12 Particle separation results at 450 Hz.

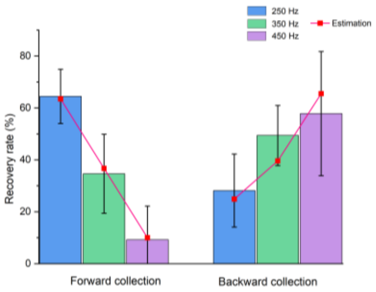

Fig. 6.13 Mass measurements for the forward and backward collection at the different frequencies and a comparison with estimates from single size group particle experimental results.

6.4 Conclusions

Theoretical analyses and simulations have been performed for the separation of particles using the ETW system. Based on the frequency effect on particle motion direction, the separation for ballotini with different sizes have been tested and show good performance. The main findings are described below.

1. The ability to transport large amounts of particles was tested across various initial quantities, from single layers to small hills. Single-layer distribution allowed for easy particle transport, while particle clusters forming hills faced obstacles due to low electric field force and pressure. Strong flowability among particles enabled effective movement. The motion initiation occurred from the outer edges, creating gaps and facilitating particle drop down close to surface and flow.

2. The mass measurement of particles transported in the forward and backward directions was conducted with four particle size groups at different frequencies: 30 to 50 μm, 75 to 110 μm, 220 to 280 μm, and 300 to 350 μm. Plots depicting the mass fraction of particles in each size group moving forward and backward revealed a frequency-dependent effect. At lower frequencies, most particles moved forward, while higher frequencies increased the fraction of particles moving backward, indicating a crossover point. The crossover frequency, where particles have an equal likelihood of moving in either direction, decreases with the increase of particle size. This parameter can be used as a baseline for adjusting frequencies to separate particles by size, optimizing the movement of fine particles forward and coarse particles backward.

3. Transporting a mixture of different size groups of particles at specific frequencies results in the concentration of small particles in the forward collection box and larger particles in the backward collection. The predicted separation performance for size groups of 30 to 50 μm and 75 to 110 μm, with equal initial mass, showed high recovery rates and fine particle concentrations exceeding 75% in the frequency range of 240 Hz to 320 Hz. In the 320 to 425 Hz range, the recovery rate and concentration for coarse particles in the backward collection could exceed 60%. Separation experiments at 350 Hz demonstrated effective separation, with backward collection consisting mainly of coarse particles. Comparison between the experimental results and estimations showed good agreement. Lower frequencies (250 Hz) increased the concentration of coarse particles in the backward collection, while higher frequencies (450 Hz) increased the concentration of finer particles in the forward collection. There is a trade-off between purifying fine and coarse particles, and adjusting the frequency can meet specific needs.

Chapter 7 Conclusions and Future Work

7.1 Research Summary

This study explores particle motion in ETW fields. The effects of particle size and charge, voltage frequency, wavelength and initial positions of particles on particle motion modes, moving velocity and levitation height were evaluated by performing single particle simulations and experiments. These analyses and conclusions provide guidance for the design and operation of an ETW system for particle transport and size separation. A suitable system was constructed, and it performed as predicted by the single size particle simulations, producing satisfactory size separations performance. This study was performed in a series of stages, each building on the previous development.

Firstly, the development of ETW equipment designs in the areas of dust mitigation, particle transport and ISRU processes, along with their performance at laboratory and industrial scales, were reviewed in detail. The different terminologies used for ETW methods in different development stages and application areas were clarified and the literatures were classified based on the types of applications. These will aid future research and searching of references.

One of the gaps identified in the literature review was that the results of experiment and simulation lack effective quantitative comparison methods, and simulations have not been adequately validated. Single particle simulations and single particle experiments can provide a means to validate each other effectively. These conclusions also provide direct and accurate information for the design of an ETW system for particle transport.

Secondly, the accurate calculation of the ETW electric field distribution is essential for the analysis of Coulomb force and DEP, and required to simulate and predict particle trajectories. The CSM and BEM were explored for the numerical solution of the electric field for an interdigitated, rectangular electrode array with a specified thickness. A low accumulated error of the CSM was achieved by properly arranging the positions and numbers of contour points and fictitious charges. The BEM can avoid the inconvenience of the charge position required in the CSM. The numerical results showed extremely close agreement between the CSM and BEM. For simplification, the method of images was introduced in the implementation of the CSM and BEM. Moreover, analytical formulas were obtained for the integral of Green's function along boundary elements. For further validation, the results were cross-checked using the FEM. It was found that discrepancies occur at the ends of the electrode array, indicating that the FEM may not be suitable for determining the electric field in systems with sharp boundaries. Finally, analyses were provided of the electric field and dielectrophoretic components with 8- and 16-electrode systems. Emphasis was given to the regions close to the electrode surfaces. This accurate evaluation of the electric field will benefit the simulation and analysis of motion of particles in ETW fields.

Thirdly, a detailed simulation model was developed to analyse the effect of various parameters on particle moving velocity and levitation height in terms of motion modes. The net force on a single particle in the simulation model was described and the formulas for the calculation of these forces were provided. The formulas for the calculation of the electric field were derived by using the Fourier expansion method including the accurate boundary conditions near the surface of the electrodes based on the numerical results using BEM. Ballotini particles were selected for simulation and experimentation. A free fall system was used to measure the charges on the ballotini particles and the results were used as reference for the particle charge in the simulations.

The analysis of the effects of different parameters on particle moving characteristics such as simulated average velocity were based on the classification of motion modes. In surfing mode, the average velocity of small particles was the same as the travelling wave. As the frequency increases, the average velocity of a particle will increase as the wave velocity increases with the frequency. And if the frequency increases further, the particle can no longer follow the wave due to the air drag force and may enter into curtain mode. Curtain mode motion is a cyclic motion due to the rotational travelling electric fields and the balance of Coulomb force with air drag force and gravitational force. In curtain mode, particles are levitated away from the electrodes and move at low velocity. In addition, the effect of particle size was explored. A 3-D representation (Fig. 4.12) for the relationships between particle size and frequency was developed. The plot reveals clearly that at lower frequencies, particle average velocity tends to increase with an increase in frequency. However, when frequency increases further, the particle velocity drops rapidly and may even move backward at certain high frequencies. In addition, larger particles tend to drop and move backward at lower frequencies. The backward motion due to the harmonic wave is only noticeable when the particle size is large or frequency is high. This backward motion related to particle size has not been explained previously in the literatures. In addition, the effect of initial positions and initial velocity on particle moving trajectories were evaluated. In hopping mode, particle trajectories may be affected by initial positions and have different moving direction, especially at high frequencies. The change of initial positions won't alter particles' stable motion modes, but the change of initial velocity may.

In the next part of the research, the motion direction of particles was specifically studied to guide the design for particle separation by size. In the simulations, 1000 random initial positions across a wavelength was selected and their relative displacements after a time of 0.5 s was recorded for the statistical analysis of motion direction. The increase of frequency or particle size will increase the fraction of particles moving backward. In addition, the simulation results of the average velocity and levitation height for particles in curtain mode were compared with the analytical results, which validated the simulation model. The analytical model allows for a variation in parameters to be performed for optimizing designs.

In order to validate the simulation model and conclusions, a comprehensive experiment methodology was established, addressing key aspects such as material selection, experiment set-up, experimental procedures, and data analysis methods.

The analysis of the single particle experimental results from the trajectories extracted from high-speed camera videos focused on three aspects: particle motion mode, motion direction and speed. Different motion directions were observed for particles in hopping mode and surfing mode. Two type of particles were tested, PMMA and ballotini particles. Large ballotini particles tended to move backward, because they were poorly charged and driven mainly by DEP. PMMA particles with high charge travel along the ETW wave and their velocities agreed well with wave velocities at different frequencies, respectively. Neutralized particle showed backward motion. An analysis of the effect of DEP was performed by comparing the maximum forces on ballotini particles with varying sizes that showed the DEP becomes more dominant as the particle size increases. Therefore, dielectrophoretic forces is one of the reasons for backward motion for particles with low charge. However, there are limitations to the single particle type experiments, the most important of which is the measurement and control of particle charge. The difficulty in controlling the charge increases the challenges of obtaining highly reproducible results in the experiment.

In the multiple particle transport experiments, the particle transport ability was initially verified by testing the transport of particles with the initial quantities of particles ranging from single layers to small piles. Particles could be transported relatively easily if they were distributed in a single layer, regardless of their quantity. However, the cluster of particles forming a pile would lead to low electric field force acting on the top particles and the pressure exerted by the top particles on those beneath them became obstacles that affected particle motion. The results showed that as long as there was strong flowability among the particles, they would move effectively regardless of the height of the piles.

Four groups of particle size were tested for the mass measurement of particle transported in forward and backward directions, 30 to 50 μm, 75 to 110 μm, 220 to 280 μm, and 300 to 350 μm. Two graphs indicating the mass fraction of particles of each size range cohort collected in forward and backward directions as a function of frequency were plotted for each size group. The results exhibited a noticeable frequency-dependent effect. At lower frequencies, a majority of particles moved forward, but as the frequency increased, the fraction of particles being transported backward increased. These forward and backward graphs have a crossover point. The frequency corresponding this point is defined as the “crossover” frequency, which means a particle has an equal chance to move forward or backward. The crossover frequency decreases as the particle size increases and can be used to select the appropriate frequencies to separate particles by size.

Transporting a mixture of different sizes of particles at appropriate frequencies cause small particles to move in the forward direction, and larger particles to move to the backward direction. The separation performance for mixtures of size groups of 30 to 50 μm and 75 to 110 μm with equal initial mass as a function of frequency was evaluated theoretically and experimentally. Both the recovery rate and concentration of fine particles were higher than 75% within the frequency range from 240 Hz to 320 Hz. In the frequency range of 320 to 425 Hz, the recovery rate and concentration for coarse particles could be larger than 60%. The separation results indicated that lower frequency increased the concentration of coarse particle in the backward collection while higher frequency increased the concentration of finer particle in the forward collection. There is a trade-off between the recovery and concentration of fine and coarse particle. The adjustment of frequency can achieve the desired result.

7.2 Main Findings and Conclusions

The main findings and conclusions of this research can be summarised as follows:

1. The literature review on ETW methods bring together the research for particle transport and separation carried out by different techniques, such as electric curtain and EDS. It helps detail the development of these equipment designs and evaluate their performance, which provides a guide for possible improvement of the effectiveness of ETW devices by outlining the limitations in simulations and experiments. It also provides insights where this research project begins on the design of system for particle transport and separation. These findings were included in chapter 2 and most of the contents are adapted from the published paper: Yu, Y., Cilliers, J., Hadler, K., Starr, S. and Wang, Y., 2022. A review of particle transport and separation by electrostatic travelling wave methods. Journal of Electrostatics, 119, 103735.

2. The CSM and BEM were implemented for the calculation of accurate electric field distribution for an interdigitated, rectangular electrode array with a specified thickness. The method of images was used to improve the calculation efficiency. In addition, analytical solutions for the integral of Green's function along the boundary elements were derived, which allows efficient implementation of the BEM and can be utilized for the general 2D BEM of electrostatic potential problems. These calculations and analyses were published in the paper: Yu, Y., Luo, Y., Cilliers, J., Hadler, K., Starr, S. and Wang, Y., 2023. Numerical solution of the electric field and dielectrophoresis force of electrostatic travelling wave system. Micromachines, 14, (7), 1347.

3. A detailed simulation model for single particle movement in an ETW field was developed. The simulation results clarified and explained the effect of various parameters on particle moving velocity and levitation height in terms of motion modes. These conclusions provide insights for the design and

optimization of ETW systems for the following experimental research, potentially improving transportation efficiency and separation performance. More details of the conclusion can be found in chapter 4 and these are published in the paper: Yu, Y., Cilliers, J., Hadler, K., Starr, S. and Wang, Y., 2023. The motion of small particles in electrostatic travelling waves for transport and separation. Powder Technology, 425, 118587.

4. Single particle experiments clearly presented three typical motion modes: curtain mode, hopping mode and surfing mode. Backward motion of large ballotini particles was observed. Subsequent experiments on neutralized and charged PMMA particles revealed the effect of DEP on backward motion. The calculation formulas for the rigorous determination of the DEP were derived. An analysis of the effect of DEP by comparing the maximum forces on ballotini particle with varying sizes was provided, which proves that the DEP becomes more dominant as the particle size increases. The content of calculation and analysis of DEP have been published in this Yu, Y., Cilliers, J., Hadler, K., Starr, S. and Wang, Y., 2024. Dry particle size separation using electrostatic travelling wave methods. Separation and Purification Technology,126275.

5. The particle transport ability of the designed ETW system was shown experimentally, at various frequencies and for different particle sizes. A crossover frequency was found and defined, at which a particle is equally likely to move forward along or backward against the travelling wave. This critical frequency decreases as the particle size increases. The successful separation of particles with different sizes has been experimentally demonstrated. The main experimental results and the conclusions about the definitions of crossover frequency have also been included in the above paper in the journal of Separation and Purification Technology.

7.3 Future Work

The simulation and experimental research explored the motion mechanisms of particle motion in ETW fields. An ETW system was developed and achieved the goal of particle transport and separation by size. Further extensions of the simulation and experimental research may benefit the understanding and utilization of ETW methods, as follows:

3D solution of the distribution of ETW fields and 3D simulation

In most simulation research, the electric field distribution of ETW systems has been simplified to a 2D problem by assuming that particles move in the centre of fields where the gradient of electric field along the length direction of electrodes is zero. In realistic situations, edge effects are unavoidable because particles will be transported to the edges. In addition, from the observation of particle transport experiments, some particles will move off the ETW board in the length directions of the electrodes under high operating frequencies. Therefore, 3D simulations of particle motion is essential for the analysis of edge effects of particle transport and beneficial for the design of ETW systems.

Field-only surface integral equations might be helpful for the 3D calculations of the electric fields [161, 162].

Multiple-particle simulation research

Multiple-particle simulation more closely represent realistic applications. Previous research has adopted either a modified hard-sphere or soft-sphere DEM simulation model including the collisions between particles to predict the transport performance of particles, such as levitation height. However, these simulation needs to be more rigorous. Many studies kept the particles' charge constant during transport. However, triboelectric charging between particles and the dielectric layer must be included. In addition, the comparison and verification of simulation models using experimental results require greater detail. The simulation set up should be more results-oriented so that it can provide more direct and accurate information in the design and application of devices.

Physical interpretation of the relationship between cross-over frequency and particle size

The relationship between crossover frequency and particle size has been experimentally determined. Nevertheless, the underlying physical significance of this relationship remains ambiguous. An assumption regarding the empirical formula for calculating fixed velocity has not been validated. Future research could concentrate on validating the formula further and enhancing our understanding of the underlying physics.

Experiment research on different types of particles and experimental conditions

Transport and separation of ballotini particles by size has been successfully demonstrated experimentally. In order to extend the separation ideas on collecting different sizes in the forward and backward directions, more types of particles with different physical properties need to be tested, such as PMMA particle and combinations of different particles. Air drag force and gravitational force have large impacts on particle motion. Experiments in low gravity and vacuum conditions would be very meaningful for exploring the practical application in space environments.

References

[1] D. Kornuta, A. Abbud-Madrid, J. Atkinson, J. Barr, G. Barnhard, D. Bienhoff, B. Blair, V. Clark, J. Cyrus, B. DeWitt, Commercial lunar propellant architecture: A collaborative study of lunar propellant production, Reach, 13 (2019) 100026.

[2] R. Ash, W. Dowler, G. Varsi, Feasibility of rocket propellant production on Mars, Acta Astronautica, 5 (1978) 705-724.

[3] S.O. Starr, A.C. Muscatello, Mars in situ resource utilization: a review, Planetary and Space Science, 182 (2020) 104824.

[4] G.B. Sanders, W.E. Larson, Progress Made in Lunar In Situ Resource Utilization under NASA's Exploration Technology and Development Program, Journal of Aerospace Engineering, 26 (2013) 5-17.

[5] M. Hecht, J. Hoffman, D. Rapp, J. McClean, J. SooHoo, R. Schaefer, A. Aboobaker, J. Mellstrom, J. Hartvigsen, F. Meyen, E. Hinterman, G. Voecks, A. Liu, M. Nasr, J. Lewis, J. Johnson, C. Guernsey, J. Swoboda, C. Eckert, C. Alcalde, M. Poirier, P. Khopkar, S. Elangovan, M. Madsen, P. Smith, C. Graves, G. Sanders, K. Araghi, M. de la Torre Juarez, D. Larsen, J. Agui, A. Burns, K. Lackner, R. Nielsen, T. Pike, B. Tata, K. Wilson, T. Brown, T. Disarro, R. Morris, R. Schaefer, R. Steinkraus, R. Surampudi, T. Werne, A. Ponce, Mars Oxygen ISRU Experiment (MOXIE), Space Science Reviews, 217 (2021) 1-76.

[6] S. Trigwell, J.G. Captain, E.E. Arens, J.W. Quinn, C.I. Calle, The use of tribocharging in the electrostatic beneficiation of lunar simulant, IEEE Transactions on Industry Applications, 45 (2009) 1060-1067.

[7] L. Taylor, D. McKay, J. Graf, A. Patchen, S. Wentworth, R. Oder, E. Jerde, Magnetic beneficiation of high-Ti mare basalts: Petrographic analyses, Abstracts of the Lunar and Planetary Science Conference, volume 23, page 1415,(1992), 1992.

[8] L. Taylor, H. Schmitt, W. Carrier, M. Nakagawa, Lunar dust problem: From liability to asset, 1st space exploration conference: continuing the voyage of discovery, 2005, pp. 2510.

[9] M. Adachi, H. Moroka, H. Kawamoto, S. Wakabayashi, T. Hoshino, Particle-size sorting system of lunar regolith using electrostatic traveling wave, Journal of Electrostatics, 89 (2017) 69-76.

[10] T. Sarver, A. Al-Qaraghuli, L.L. Kazmerski, A comprehensive review of the impact of dust on the use of solar energy: History, investigations, results, literature, and mitigation approaches, Renewable and Sustainable Energy Reviews, 22 (2013) 698-733.

[11] B. Guo, W. Javed, C. Pett, C.-Y. Wu, J.R. Scheffe, Electrodynamic dust shield performance under simulated operating conditions for solar energy applications, Solar Energy Materials and Solar Cells, 185 (2018) 80-85.

[12] M. Mazumder, R. Sharma, A.S. Biris, J. Zhang, C. Calle, M. Zahn, Self-Cleaning Transparent Dust Shields for Protecting Solar Panels and Other Devices, Particulate Science and Technology, 25 (2007) 5-20.

[13] C.I. Calle, C.R. Buhler, M.R. Johansen, M.D. Hogue, S.J. Snyder, Active dust control and mitigation technology for lunar and Martian exploration, Acta Astronautica, 69 (2011) 1082-1088.

[14] C.I. Calle, J.L. McFall, C.R. Buhler, S.J. Snyder, E.E. Arens, A. Chen, M.L. Ritz, J.S. Clements, C.R. Fortier, S. Trigwell, Dust Particle Removal by Electrostatic and Dielectrophoretic Forces with Applications to NASA Exploration Missions, Proc. ESA Annual Meeting on Electrostatics, ESA Minneapolis, MN, 2008.

[15] D. Loftus, J. Rask, C. McCrossin, E. Tranfield, The chemical reactivity of lunar dust: from toxicity to astrobiology, Earth, Moon, and Planets, 107 (2010) 95-105.

[16] M. Pohlen, D. Carroll, G.K. Prisk, A.J. Sawyer, Overview of lunar dust toxicity risk, npj Microgravity, 8 (2022) 55.

[17] D. Linnarsson, J. Carpenter, B. Fubini, P. Gerde, L.L. Karlsson, D.J. Loftus, G.K. Prisk, U. Staufer, E.M. Tranfield, W. van Westrenen, Toxicity of lunar dust, Planetary and Space Science, 74 (2012) 57-71.

[18] H.A. Pohl, The motion and precipitation of suspensoids in divergent electric fields, Journal of applied Physics, 22 (1951) 869-871.

[19] H.A. Pohl, Some effects of nonuniform fields on dielectrics, Journal of Applied Physics, 29 (1958) 1182-1188.

[20] S. Masuda, K.Fujibayashi, K.Ishida, H.Inaba, Confinement and transportation of charged aerosol clouds via electric curtain, Electrical Engineering In Japan, 92 (1972) 9-18.

[21] S. Masuda, T. Kamimura, Approximate methods for calculating a non-uniform travelling, Journal of Electrostatics, 1 (1975) 351-370.

[22] S. Masuda, Y. Matsumoto, Theoretical Characteristics of Standing-Wave Electric Curtains, Electrical Engineering In Japan, 93 (1973) 41-54.

[23] S. Masuda, M. Washizu, M. Iwadare, Separation of Small Particles Suspended in Liquid by Nonuniform Traveling Field, IEEE Transactions on Industry Applications, 23 (1987) 474-480.

[24] S. Masuda, M. Washizu, I. Kawabata, Movement of Blood Cells in Liquid by Nonuniform Traveling field, IEEE Transactions on Industry Applications, 24 (1988) 217-222.

[25] A.C. Yen, C.D. Hendricks, A planar electric curtain used as a device for the control and removal of particulate materials, Journal of Electrostatics, 4 (1978) 255-267.

[26] F.W. Schmidlin, A new nonlevitated mode of traveling wave toner transport, IEEE transactions on industry applications, 27 (1988) 480-488.

[27] F.W. Schmidlin, Modes of traveling wave particles transport and their applications, Journal of Electrostatics, 34 (1995) 225-245.

[28] W. Machowski, W. Balachandran, D. Hu, Influence of electrode geometry on transport and separation efficiency of powders using traveling wave field technique, IEEE Industry Applications Conference Thirtieth IAS Annual Meeting, 1995.

[29] J. Gu, X. Qian, Y. Liu, Q. Wang, Y. Zhang, X. Ruan, X. Deng, Y. Lu, J. Song, H. Zhang, Y. Dong, M. Wei, S. Li, W.H. Wang, Z. Zou, M. Yang, W. Yao, (2023).

[30] J.K.W. Chesnutt, J.S. Marshall, Simulation of Particle Separation on an Inclined Electric Curtain, IEEE Transactions on Industry Applications, 49 (2013) 1104-1112.

[31] G.Q. Liu, J.S. Marshall, Effect of particle adhesion and interactions on motion by traveling waves on an electric curtain, Journal of Electrostatics, 68 (2010) 179-189.

[32] A. Zouaghi, N. Zouzou, Impact of spatial harmonic waves on dielectric particles displacement in standing and traveling wave electric fields, Journal of Electrostatics, 98 (2019) 25-33.

[33] A. Zouaghi, N. Zouzou, Numerical modeling of particle motion in traveling wave solar panels cleaning device, Journal of Electrostatics, 110 (2021) 103552.

[34] A. Zouaghi, N. Zouzou, P. Braud, Study of dielectric particles motion in traveling and standing electrostatic waves using particle tracking velocimetry, Journal of Physics D: Applied Physics, 53 (2020) 385502.

[35] A. Zouaghi, N. Zouzou, L. Dascalescu, Assessment of forces acting on fine particles on a traveling-wave electric field conveyor: Application to powder manipulation, Powder Technology, 343 (2019) 375-382.

[36] M. Mazumder, C. Elinger, K. O’Connor, R. Eriksen, A. Bernard, M.N. Horenstein, J. Yellowhair, N. Joglekar, S. Garner, J. Bones, C. Morales, H. Acuña, Industrial Production and Field Evaluation of Transparent Electrodynamic Screen (EDS) Film for Water-Free Cleaning of Solar Collectors, in: IEEE (Ed.) 2019 IEEE 46th Photovoltaic Specialists Conference (PVSC), IEEE, 2019, pp. 3269-3276.

[37] M. Mazumder, M.N. Horenstein, N.R. Joglekar, A. Sayyah, J.W. Stark, A.A.R. Bernard, S.M. Garner, J.E. Yellowhair, H.Y. Lin, R.S. Eriksen, A.C. Griffin, Y. Gao, R.L. Centra, A.H. Lloyd, Mitigation of Dust Impact on Solar Collectors by Water-Free Cleaning With Transparent Electrodynamic Films: Progress and Challenges, IEEE Journal of Photovoltaics, 7 (2017) 1342-1353.

[38] A. Sayyah, R.S. Eriksen, M.N. Horenstein, M.K. Mazumder, Performance Analysis of Electrodynamic Screens Based on Residual Particle Size Distribution, IEEE Journal of Photovoltaics, 7 (2017) 221-229.

[39] J. Gu, G. Zhang, Q. Wang, C. Wang, Y. Liu, W. Yao, J. Lyu, Experimental study on particles directed transport by an alternating travelling-wave electrostatic field, Powder Technology, 397 (2022) 117107.

[40] S.J. Williams, J.D. Schneider, B.C. King, N.G. Green, Particle-Induced Electrostatic Repulsion within an Electric Curtain Operating below the Paschen Limit, Micromachines (Basel), 13 (2022) 288.

[41] B. Guo, W. Javed, Y.S. Khoo, B. Figgis, Solar PV soiling mitigation by electrodynamic dust shield in field conditions, Solar Energy, 188 (2019) 271-277.

[42] F.B. Tatom, V. Srepel, R.D. Johnson, N.A. Contaxes, J.G. Adams, H. Seaman, B.L.Cline, Lunar dust degradation effects and removal or prevention concepts, NASA Technical Report, No. TR-792-7-207A (1967) 3-06.

[43] A. Sayyah, M.N. Horenstein, M.K. Mazumder, G. Ahmadi, Electrostatic force distribution on an electrodynamic screen, Journal of Electrostatics, 81 (2016) 24-36.

[44] M. Mazumder, M.N. Horenstein, J.W. Stark, Peter Girouard, R. Sumner, B. Henderson, O. Sadder, I. Hidetaka, A.S. Biris, R. Sharma, Characterization of Electrodynamic Screen Performance for Dust Removal from Solar Panels and Solar Hydrogen Generators, IEEE Transactions on Industry Applications, 49 (2013) 1793-1800.

[45] C. Han, Q. Zhou, J. Hu, C. Liang, X. Chen, J. Ma, The charging characteristics of particle–particle contact, Journal of Electrostatics, 112 (2021) 103582.

[46] K.M. Abdelaziz, J. Chen, T.J. Hieber, Z.C. Leseman, Atomistic Field Theory for contact electrification of dielectrics, Journal of Electrostatics, 96 (2018) 10-15.

[47] A.E. Wang, P.S. Gil, M. Holonga, Z. Yavuz, H.T. Baytekin, R.M. Sankaran, D.J. Lacks, Dependence of triboelectric charging behavior on material microstructure, Physical Review Materials, 1 (2017).

[48] S. Trigwell, N. Grable, C.U. Yurteri, R. Sharma, M.K. Mazumder, Effects of surface properties on the tribocharging characteristics of polymer powder as applied to industrial processes, IEEE Transactions on Industry Applications, 39 (2003) 79-86.

[49] S. Matsusaka, H. Maruyama, T. Matsuyama, M. Ghadiri, Triboelectric charging of powders: A review, Chemical Engineering Science, 65 (2010) 5781-5807.

[50] F. Chowdhury, M. Ray, A. Sowinski, P. Mehrani, A. Passalacqua, A review on modeling approaches for the electrostatic charging of particles, Powder Technology, 389 (2021) 104-118.

[51] H. Kawamoto, K. Seki, N. Kuromiya, Mechanism of travelling-wave transport of particles, Journal of Physics D: Applied Physics, 39 (2006) 1249-1256.

[52] J.R. Melcher, E.P. Warren, R.H. Kotwal, Theory for Finite-Phase Traveling-Wave Boundary-Guided Transport of Triboelectrified Particles, IEEE transactions on industry applications, 24 (1989) 949-955.

[53] H. Kawamoto, T. Shibata, Electrostatic cleaning system for removal of sand from solar panels, Journal of Electrostatics, 73 (2015) 65-70.

[54] R.A. Sims, A.S. Biris, J.D. Wilson, C.U. Yurteri, M.K. Mazumder, C.I. Calle, C.R. Buhler, Development of a Transparent Self-Cleaning Dust Shield for Solar Panels, IEEE Joint Meet. Electrostat, 2003, pp. 814-821.

[55] P.E. Clark, C.I. Calle, S.A. Curtis, J.F. Keller, F. Minetto, J.G. Mantovani, Electrostatic Dust Control on Planetary Surfaces, AIP Conference Proceedings, American Institute of Physics, 2007, pp. 400-406.

[56] P.E. Clark, S.A. Curtis, F. Minetto, J. Marshall, J. Nuth, C. Calle, SPARCLE: Electrostatic Dust Control Tool Proof of Concept, AIP Conference Proceedings, American Institute of Physics, 2010, pp. 549-556.

[57] M. Mazumder, R. Sharma, A.S. Biris, M.N. Horenstein, J. Zhang, H. Ishihara, J.W. Stark, S. Blumenthal, O. Sadder, Electrostatic Removal of Particles and its Applications to Self-Cleaning Solar Panels and Solar Concentrators, William Andrew Publishing2011.

[58] A. Sayyah, M.N. Horenstein, M.K. Mazumder, Mitigation of Soiling Losses in Concentrating Solar Collectors, in: IEEE (Ed.) IEEE 39th Photovoltaic Specialists Conference (PVSC), IEEE, 2013, pp. 0480-0485.

[59] A. Sayyah, M.N. Horenstein, M.K. Mazumder, A comprehensive analysis of the electric field distribution in an electrodynamic screen, Journal of Electrostatics, 76 (2015) 115-126.

[60] A. Sayyah, M.N. Horenstein, M.K. Mazumder, Performance Restoration of Dusty Photovoltaic Modules Using Electrodynamic Screen, in: IEEE (Ed.) IEEE 42nd Photovoltaic Specialist Conference (PVSC), IEEE, 2015, pp. 1-3.

[61] A.A.R. Bernard, R.l. Centra, E. Argentieri, R.S. Eriksen, S. Garner, Mark.N.Horenstein, Malay.K.Mazumder, Optimization of Optical Performance and Dust Removal Efficiency of Electrodynamic Screen (EDS) Films for Improving Energy-Yield of Solar Collectors, in: IEEE (Ed.) 2018 IEEE 7th World Conference on Photovoltaic Energy Conversion (WCPEC)(A Joint Conference of 45th IEEE PVSC, 28th PVSEC & 34th EU PVSEC), IEEE, 2018, pp. 3451-3454.

[62] A. Faes, D. Petri, J. Champliaud, J. Geissbühler, N. Badel, J. Levrat, B. Roustom, A. Hessler-Wyser, N. Wyrsch, C. Ballif, G.O. Getaz, G. McKarris, M. Despeisse, Field test and electrode optimization of electrodynamic cleaning systems for solar panels, Progress in Photovoltaics: Research and Applications, 27 (2019) 1020-1033.

[63] B. Guo, B. Figgis, W. Javed, Measurement of electrodynamic dust shield efficiency in field conditions, Journal of Electrostatics, 97 (2019) 26-30.

[64] A. Sayyah, D.R. Crowell, A. Raychowdhury, M.N. Horenstein, M.K. Mazumder, An experimental study on the characterization of electric charge in electrostatic dust removal, Journal of Electrostatics, 87 (2017) 173-179.

[65] M. Mazumder, M. Horenstein, J. Stark, D. Erickson, A. Sayyah, S. Jung, F. Hao, Development of self-cleaning solar collectors for minimizing energy yield loss caused by dust deposition, Proceedings of the ASME 2013 7th International Conference on Energy Sustainability, American Society of Mechanical Engineers, Minneapolis, MN, USA, 2013.

[66] B. Guo, W. Javed, A. Al-Kuwari, Effect of Voltage Rise Time on the Efficiency of Electrodynamic Dust Shield, IEEE Journal of Photovoltaics, 9 (2019) 1086-1090.

[67] Z. Jie, Z. Chuande, Z. Fuzhong, L. Shuhua, F. Miao, T. Yike, Experimental and numerical modeling of particle levitation and movement behavior on traveling-wave electric curtain for particle removal, Particulate Science and Technology, 37 (2018) 741-749.

[68] J.K.W. Chesnutt, H. Ashkanani, B. Guo, C.-Y. Wu, Simulation of microscale particle interactions for optimization of an electrodynamic dust shield to clean desert dust from solar panels, Solar Energy, 155 (2017) 1197-1207.

[69] M.N. Horenstein, M.K. Mazumder, R.C. Sumner, J. Stark, T. Abuhamed, R. Boxman, Modeling of Trajectories in an Electrodynamic Screen for Obtaining Maximum Particle Removal Efficiency, IEEE Transactions on Industry Applications, 49 (2013) 707-713.

[70] M.N. Horenstein, M. Mazumder, R.C. Sumner, Predicting particle trajectories on an electrodynamic screen – Theory and experiment, Journal of Electrostatics, 71 (2013) 185-188.

[71] A. Sayyah, R.S. Eriksen, M.N. Horenstein, M.K. Mazumder, Analysis of Particle Size Distribution of Residual Dust in Cleaning Process Using an Electrodynamic Screen, in: IEEE (Ed.) 2016 IEEE 43rd Photovoltaic Specialists Conference (PVSC), IEEE, 2016, pp. 2058-2060.

[72] C.E. Johnson, P.K. Srirama, R. Sharma, K. Pruessner, J. Zhang, M.K. Mazumder, Effect of particle size distribution on the performance of electrodynamic screens, in: IEEE (Ed.) 40th IAS Annual Meeting, 2005, pp. 341-345.

[73] H.T. Ahmed, Z.M. Elmouloud, B. Ail, R. Ouiddir, A. Tilmatine, Experimental analysis of micronized plastic particle movement on electrodynamic screens, International Journal of Environmental Studies, 79 (2021) 72-87.

[74] W. Javed, B. Guo, Effect of relative humidity on dust removal performance of electrodynamic dust shield, Journal of Electrostatics, 105 (2020) 103434.

[75] J.N. Rasera, J.J. Cilliers, J.A. Lamamy, K. Hadler, The beneficiation of lunar regolith for space resource utilisation: A review, Planetary and Space Science, 186 (2020) 104879.

[76] H. Kawamoto, S. Kojima, Electrostatic Precipitation in the Martian Environment, Journal of Aerospace Engineering, 32 (2019) 04019006.

[77] C.I. Calle, M.K. Mazumder, C.D. Immer, C.R. Buhler, S. Clements, P. Lundeen, A. Chen, J.G. Mantovani, Electrodynamic dust shield for surface exploration activities on the Moon and Mars, 57th International Astronautical Congress, 2006, pp. A5-2.

[78] C.I. Calle, C.R. Buhler, J.G. Mantovani, S. Clements, A. Chen, M.K. Mazumder, A.S. Bins, A.W. Nowicki, Electrodynamic dust shield for solar panels on Mars, 35th Lunar and Planetary Science Conference, 2004, pp. 15-19.

[79] P. Atten, H.L. Pang, J.-L. Reboud, Study of Dust Removal by Standing-Wave Electric Curtain for Application to Solar Cells on Mars, IEEE Transactions on Industry Applications, 45 (2009) 75-86.

[80] R. Sharma, C.A. Wyatt, J. Zhang, C.I. Calle, N. Mardesich, M.K. Mazumder, Experimental Evaluation and Analysis of Electrodynamic Screen as Dust Mitigation Technology for Future Mars Missions, IEEE Transactions on Industry Applications, 45 (2009) 591-596.

[81] H. Kawamoto, M. Uchiyama, B.L. Cooper, D.S. McKay, Mitigation of lunar dust on solar panels and optical elements utilizing electrostatic traveling-wave, Journal of Electrostatics, 69 (2011) 370-379.

[82] H. Kawamoto, Improved Electrostatic Shield for Lunar Dust Entering into Mechanical Seals of Equipment Used for Long-Term Lunar Exploration, 44th International Conference on Environmental Systems, 2014.

[83] H. Kawamoto, Electrostatic and Magnetic Cleaning Systems for Removing Lunar Dust Adhering to Spacesuits, 2012.

[84] N.A. Mohajer, C.-Y. Wu, R. Moore, N. Sorloaica-Hickman, Design of an electrostatic lunar dust repeller for mitigating dust deposition and evaluation of its removal efficiency, Journal of Aerosol Science, 69 (2014) 21-31.

[85] C.I. Calle, C.R. Buhler, J.L. McFall, S.J. Snyder, Particle removal by electrostatic and dielectrophoretic forces for dust control during lunar exploration missions, Journal of Electrostatics, 67 (2009) 89-92.

[86] K.K. Manyapu, P. De Leon, L. Peltz, J.R. Gaier, D. Waters, Proof of concept demonstration of novel technologies for lunar spacesuit dust mitigation, Acta Astronautica, 137 (2017) 472-481.

[87] K.K. Manyapu, L. Peltz, P. De Leon, Self-cleaning spacesuits for future planetary missions using carbon nanotube technology, Acta Astronautica, 157 (2019) 134-144.

[88] J.R. Melcher, E.P. Warren, R.H. Kotwal, Traveling-wave delivery of single-component developer, IEEE transactions on industry applications, 25 (1989) 956-962.

[89] J.R. Melcher, E.P. Warren, R.H. Kotwal, Theory for Pure-Traveling-Wave Boundary-Guided Transport of Tribo-Electrified Particles, Particulate Science and Technology, 7 (1989) 1-21.

[90] H. Kawamoto, S. Hayashi, Fundamental investigation on electrostatic travelling-wave transport of a liquid drop, Journal of Physics D: Applied Physics, 39 (2006) 418-423.

[91] J. Gu, Q. Wang, Y. Wu, L. Feng, G. Zhang, S. Li, L. Tian, W. Yao, Numerical study of particle transport by an alternating travelling-wave electrostatic field, Acta Astronautica, 188 (2021) 505-517.

[92] H. Kawamoto, N. Hasegawa, K. Seki, Traveling Wave Transport of Particles Particle Size Classification, Proceedings of Japan Machinery Society, 69 (2003) 1216-1221.

[93] D. Hu, W. Balachandran, W. Machowski, Computer user interface and simulation for designing a travelling wave panel electrode, Proceedings of 1994 IEEE Industry Applications Society Annual Meeting, 1994, pp. 1621-1626.

[94] D. Hu, W. Balachandran, W.W. Machowski, Design of traveling-wave field panel for pharmaceutical powders based on computer simulation of particle trajectories, IEEE Transactions on Industry Applications, 33 (1997) 641-650.

[95] Y.N. Gartstein, J.G. Shaw, Many-particle effects in travelling electrostatic wave transport, Journal of Physics D: Applied Physics, 32 (1999) 2176-2180.

[96] M. Adachi, Dynamics of Electromagnetic Particles and Its Application for Mitigation and Utilization Technologies of Regolith on Moon, Mars, and Asteroids, Department of Applied Mechanics Research on Precision Engineering, Waseda University, Japan, 2017, pp. 206.

[97] M.D. Thompson, Y. Gartstein, J.T. LeStrange, Aspects of Toner Transport on a Traveling Wave Device, NIP & Digital Fabrication Conference. Society for Imaging Science and Technology, 1999, pp. 262-265.

[98] R. Kober, Traveling wave transport of conductive toner particles, NIP & Digital Fabrication Conference. Society for Imaging Science and Technology, 2000, pp. 736-739.

[99] K. Taniguchi, S. Morikuni, S. Watanabe, Y. Nakano, T. Sakai, H. Yamamoto, T. Yagi, Y. Yamanoto, Improved driving characteristics for the toner transportation system, NIP & Digital Fabrication Conference. Society for Imaging Science and Technology, 2000, pp. 740-742.

[100] R. Kober, Simulation of Traveling Wave Toner Transport, NIP & Digital Fabrication Conference. Society for Imaging Science and Technology, 2002, pp. 453-457.

[101] K. Taniguchi, H. Yamamoto, Y. Nakano, T. Sakai, S. Morikuni, S. Watanabe, A New Technique for Measuring the Distribution of Charge-to-Mass Ration for Toner Particles with On-Line Use, Journal of Imaging Science and Technology, 47 (2003) 224-228.

[102] K. Adachi, S. Yamana, T. Nakamura, Development system by toner transportation using traveling wave electric field, NIP & Digital Fabrication Conference, Society for Imaging Science and Technology, 2005, pp. 597-601.

[103] M. Maeda, K. Maekawa, M. Takeuchi, Simulation of Traveling Wave Toner Transport Considering Air Drag, Journal of Imaging Science and Technology, 51 (2007) 431-437.

[104] H. Kawamoto, K. Shirai, Electrostatic Transport of Lunar Soil for In Situ Resource Utilization, Journal of Aerospace Engineering, 25 (2012) 132-138.

[105] H. Kawamoto, K. Hata, T. Shibata, Vertical Transport of Lunar Regolith and Ice Particles Using Electrodynamic Traveling Wave, Journal of Aerospace Engineering, 34 (2021).

[106] H. Kawamoto, Sampling of Small Regolith Particles from Asteroids Utilizing an Alternative Electrostatic Field and Electrostatic Traveling Wave, Journal of Aerospace Engineering, 27 (2014) 631-635.

[107] H. Kawamoto, M. Kato, M. Adachi, Electrostatic transport of regolith particles for sample return mission from asteroids, Journal of Electrostatics, 84 (2016) 42-47.

[108] M. Adachi, H. Kawamoto, Electrostatic Sampler for Large Regolith Particles on Asteroids, Journal of Aerospace Engineering, 30 (2017) 04016098.

[109] A. Tilmatine, A. Alibida, S. Zelmat, H. Louati, Y. Bellebna, F. Miloua, On the attraction force applied on metal pieces in a traveling wave conveyor, Journal of Electrostatics, 96 (2018) 64-68.

[110] S. Louhadj, N. Hammadi, S. Touhami, H. Louati, A. Hadjali, I.-E. Kimi, A. Tilmatine, Experimental analysis of the attraction force applied on metal particles using a double-side electrical curtain, Journal of Electrostatics, 105 (2020).

[111] X. Wang, X. Wang, F.F. Becker, P.R.C. Gascoyne, A theoretical method of electrical field analysis for dielectrophoretic electrode arrays using Green's theorem, Journal of Physics D: Applied Physics, 29 (1996) 1649-1660.

[112] H. Morgan, A.G. Izquierdo, D. Bakewell, N.G. Green, A. Ramos, The dielectrophoretic and travelling wave forces generated by interdigitated electrode arrays: analytical solution using Fourier series, Journal of Physics D: Applied Physics, 34 (2001) 1553-1561.

[113] N.G. Green, A. Ramos, H. Morgan, Numerical solution of the dielectrophoretic and travelling wave forces for interdigitated electrode arrays using the finite element method, Journal of Electrostatics, 56 (2002) 235-254.

[114] R. Cicchett, A. Faraone, On the optical behavior of the electromagnetic field excited by a semi-infinite electric traveling-wave current, IEEE Transactions on Antennas and Propagation, 53 (2005) 4015-4025.

[115] T. Sun, H. Morgan, N.G. Green, Analytical solutions of ac electrokinetics in interdigitated electrode arrays: electric field, dielectrophoretic and traveling-wave dielectrophoretic forces, Phys Rev E Stat Nonlin Soft Matter Phys, 76 (2007) 046610.

[116] V. Gauthier, A. Bolopion, M. Gauthier, Analytical Formulation of the Electric Field Induced by Electrode Arrays: Towards Automated Dielectrophoretic Cell Sorting, Micromachines (Basel), 8 (2017).

[117] H. Kawamoto, Some techniques on electrostatic separation of particle size utilizing electrostatic traveling-wave field, Journal of Electrostatics, 66 (2008) 220-228.

[118] W. Machowski, W. Balachandran, Dispersion and transport of cohesive lactose powder using travelling wave field technique, Powder Technology, 99 (1998) 251-256.

[119] H. Kawamoto, S. Naoto, Traveling Wave Transport of Particles and Particle Size Classification, Journal of Imaging Science and Technology, 48 (2004) 404-411.

[120] H. Kawamoto, H. Morooka, H. Nozaki, Improved Electrodynamic Particle-Size Sorting System for Lunar Regolith, Journal of Aerospace Engineering, 35 (2022).

[121] L.C. Weiss, D.P. Thibodeaux, Separation of seed by-products by an AC electric field, Journal of the American Oil Chemists' Society, 61 (1984) 886-890.

[122] Z. Dudzicz, The path of oscillation of dust particles in the field of the electric curtain of the plane type supplied with AC voltage, Journal of Electrostatics,, 23 (1989) 207-214.

[123] Z. Dudzicz, Electrodynamics of charged dust particles and repulsion force within plane-type electric curtain, Journal of Electrostatics, 51 (2001) 111-116.

[124] Z. Dudzicz, E. Grządziel, Influence of the AC voltage frequency on the oscillation trajectory and path length of particles inside a planar–type electric curtain, Journal of Electrostatics, 77 (2015) 8-12.

[125] Z. Dudzicz, Confinement of charged dust particles by a hybrid-type electric curtain, Journal of Electrostatics, 70 (2012) 72-76.

[126] J. Gu, X. Qian, Y. Liu, Q. Wang, Y. Zhang, X. Ruan, X. Deng, Y. Lu, J. Song, H. Zhang, Charging properties and particles dynamics of Chang'E-5 lunar sample in an external electric field, (2023).

[127] S. Saeidpour, B. Khoshnevisan, Z. Boroumand, N. Ahmady, Effect of electrode design and dust particle size on electrodynamics dust shield procedure, Physics Open, 14 (2023) 100131.

[128] M.J. Schaible, K.G. Sjolund, E.A. Ryan, M.L. Shofner, J.R. Reynolds, J.S. Linsey, T.M. Orlando, Performance of chemically modified reduced graphene oxide (CMrGO) in lunar electrodynamic dust shield (EDS) applications, Acta Astronautica, 211 (2023) 674-683.

[129] M. Heo, J. Yang, B. Kim, C. Lee, H. Park, S.-K. Kim, J. Lee, S. Son, J. Cheon, J. Choi, Self-Powered Electrodynamic Dust Removal for Sustainable Solar Panels using Triboelectric Nanogenerators, Nano Energy, (2024) 109257.

[130] E. Grün, M. Horanyi, Z. Sternovsky, The lunar dust environment, Planetary and Space Science, 59 (2011) 1672-1680.

[131] M. Anand, I.A. Crawford, M. Balat-Pichelin, S. Abanades, W. van Westrenen, G. Péraudeau, R. Jaumann, W. Seboldt, A brief review of chemical and mineralogical resources on the Moon and likely initial in situ resource utilization (ISRU) applications, Planetary and Space Science, 74 (2012) 42-48.

[132] I.A. Crawford, Lunar resources: A review, Progress in Physical Geography, 39 (2015) 137-167.

[133] K. Hadler, D.J.P. Martin, J. Carpenter, J.J. Cilliers, A. Morse, S. Starr, J.N. Rasera, K. Seweryn, P. Reiss, A. Meurisse, A universal framework for Space Resource Utilisation (SRU), Planetary and Space Science, 182 (2020) 104811.

[134] H. Kawamoto, Vibration Transport of Lunar Regolith for In Situ Resource Utilization Using Piezoelectric Actuators with Displacement-Amplifying Mechanism, Journal of Aerospace Engineering, 33 (2020) 04020014.

[135] D. Qian, J.S. Marshall, J. Frolik, Control analysis for solar panel dust mitigation using an electric curtain, Renewable Energy, 41 (2012) 134-144.

[136] R. Pethig, Review article-dielectrophoresis: status of the theory, technology, and applications, Biomicrofluidics, 4 (2010).

[137] H. Kawamoto, H. Inoue, Magnetic Cleaning Device for Lunar Dust Adhering to Spacesuits, Journal of Aerospace Engineering, 25 (2012) 139-142.

[138] M. Washizu, T. Jones, Multipolar dielectrophoretic force calculation, Journal of Electrostatics, 33 (1994) 187-198.

[139] X.-B. Wang, Y. Huang, F. Becker, P. Gascoyne, A unified theory of dielectrophoresis and travelling wave dielectrophoresis, Journal of Physics D: Applied Physics, 27 (1994) 1571.

[140] X.-B. Wang, Y. Huang, J.P.H. Burt, G.H. Markx, R. Pethig, Selective dielectrophoretic confinement of bioparticles in potential energy wells, Journal of Physics D: Applied Physics, 26 (1993) 1278-1285.

[141] R.L. Hewlin, M. Edwards, C. Schultz, Design and Development of a Traveling Wave Ferro-Microfluidic Device and System Rig for Potential Magnetophoretic Cell Separation and Sorting in a Water-Based Ferrofluid, Micromachines, 14 (2023).

[142] D.J. Chappell, Boundary integral solution of potential problems arising in the modelling of electrified oil films, (2015).

[143] H. Singer, H. Steinbigler, P. Weiss, A charge simulation method for the calculation of high voltage fields, IEEE Transactions on Power Apparatus and Systems, 5 (1974) 1660-1668.

[144] T.E. Ein, Ein Gegensttick zum Ritzschen Verfahren, In: Proceedings of the 2nd in- ternational congress on applied mechanicsZürich, 1926, pp. 131-137.

[145] J.A. Kołodziej, J.K. Grabski, Many names of the Trefftz method, Engineering Analysis with Boundary Elements, 96 (2018) 169-178.

[146] A. Yializis, E. Kuffel, P. Alexander, An Optimized Charge Simulation Method for the Calculation of High Voltage Fields, IEEE Transactions on Power Apparatus and Systems, PAS-97 (1978) 2434-2440.

[147] K.F. Riley, M.P. Hobson, S.J. Bence, Mathematical methods for physics and engineering, Cambridge University Press2010.

[148] G. Fichtenholz, Calculus Tutorial, Highe Education Press, BeiJing, 2006.

[149] Y. Luo, T. Theodoulidis, X. Zhou, A. Kyrgiazoglou, Calculation of AC resistance of single-layer coils using boundary-element method, IET Electric Power Applications, 15 (2020) 1-12.

[150] N.-V. Nguyen, T.L. Manh, T.S. Nguyen, V.T. Le, N.V. Hieu, Applied electric field analysis and numerical investigations of the continuous cell separation in a dielectrophoresis-based microfluidic channel, Journal of Science: Advanced Materials and Devices, 6 (2021).

[151] R. Krupke, F. Hennrich, H.v. Lo¨hneysen, M. Kappes, Separation of Metallic from Semiconducting Single-Walled Carbon Nanotubes, Science, 301 (2003).

[152] M. Pauthenier, M. Moreau-Hanot, La charge des particules sphériques dans un champ ionisé, Journal de Physique et le Radium, 3 (1932) 590-613.

[153] M.W.T.B. Jones, Multipolar dielectrophoretic force calculation, Journal of Electrostatics, 33 (1994) 187-198.

[154] X.-B. Wang, Y. Huang, F.F. Becker, P.R.C. Gascoyne, A unified theory of dielectrophoresis and travelling wave dielectrophoresis, Journal of Physics D: Applied Physics, 7 (1994) 1571-1574.

[155] H. Tang, R. Song, Y. Dong, X. Song, Measurement of Restitution and Friction Coefficients for Granular Particles and Discrete Element Simulation for the Tests of Glass Beads, Materials (Basel), 12 (2019) 3170.

[156] Y.I. Rabinovich, J.J. Adler, M.S. Esayanur, A. Ata, R.K. Singh, B.M. Moudgil, Capillary forces between surfaces with nanoscale roughness, Advances in Colloid and Interface Science, 96 (2002) 213-230.

[157] R.D. Cruise, K. Hadler, S.O. Starr, J.J. Cilliers, The effect of particle size and relative humidity on triboelectric charge saturation, Journal of Physics D: Applied Physics, 55 (2022).

[158] N. Afshar-Mohajer, C.-Y. Wu, J.S. Curtis, J.R. Gaier, Review of dust transport and mitigation technologies in lunar and Martian atmospheres, Advances in Space Research, 56 (2015) 1222-1241.

[159] H. Kawamoto, Manipulation of single particles by utilizing electrostatic force, Journal of Electrostatics, 67 (2009) 850-861.

[160] Y. Yu, J. Cilliers, K. Hadler, S. Starr, Y. Wang, The motion of small particles in electrostatic travelling waves for transport and separation, Powder Technology, 425 (2023).

[161] Q. Sun, E. Klaseboer, A.J. Yuffa, D.Y. Chan, Field-only surface integral equations: scattering from a perfect electric conductor, JOSA A, 37 (2020) 276-283.

[162] Q. Sun, E. Klaseboer, A.J. Yuffa, D.Y. Chan, Field-only surface integral equations: scattering from a dielectric body, JOSA A, 37 (2020) 284-293.

Appendix

A: Analytical Solution for Particle Moving Velocity and Levitation Height in Curtain Mode

In this section, the analytical solution for calculating the actual moving velocity and levitation height of a particle in curtain mode with the first and second harmonic waves of the electric field is derived by using the perturbation method [23, 52]. This method divides the moving component into two terms, a slow-varying term and small fast-varying perturbation term. The image force and dielectrophoresis are only significant close to the surface. These have little effect on a particle moving in curtain mode and are omitted. The equations of motion for particles in the stable curtain mode away from electrodes is expressed as:

$$\begin{cases} m\dfrac{d^2x}{dt^2} + 6\pi\eta r\dfrac{dx}{dt} = E_x \cdot q \\ m\dfrac{d^2y}{dt^2} + 6\pi\eta r\dfrac{dy}{dt} = E_y \cdot q - mg \end{cases} \tag{8.1}$$

where E_x and E_y are from formula (16). A set of simplifications is made: $\mathrm{M} = \mathrm{m}/6\pi\eta r$; $k_1 = V_\mathrm{A} a_1 \alpha_1 / 4\pi\eta r$; $k_2 = V_\mathrm{A} a_2 \alpha_2 / 4\pi\eta r$; $a = \alpha_1 = 1/2\alpha_2$; $\mathrm{G} = \mathrm{mg}/6\pi\eta r$; $\Omega_1 = -\Omega_2 = \omega$. So (8.1) is transformed into:

$$\begin{cases} M\dfrac{d^2x}{dt^2} + \dfrac{dx}{dt} = k_1 \sin\left(ax - \Omega_1 t\right)e^{-az} + k_2 \sin\left(2ax - \Omega_2 t\right)e^{-2az} \\ M\dfrac{d^2z}{dt^2} + \dfrac{dz}{dt} = k_1 \cos\left(ax - \Omega_1 t\right)e^{-az} + k_2 \cos\left(2ax - \Omega_2 t\right)e^{-2az} - G \end{cases} \tag{8.2}$$

According to the perturbation method, the solution of $x(t)$ is assumed as the combination of constant transport $\langle u \rangle t$ and a small dynamic oscillation $x'(t)$:

$$x(t) = X_0 + \langle u \rangle t + x'(t) \tag{8.3}$$

where X_0 is the initial position in x direction. And solution of $y(t) = Y_0 + y'(t)$, where Y_0 is the levitation height and $y'(t)$ is the small dynamic oscillation.

In addition, it was set:

$$\Omega_1 = a\left(\Omega_1' + \langle u \rangle\right),\ \Omega_2 = 2a\left(\Omega_2' + \langle u \rangle\right) \tag{8.4}$$

Using the substitutions, (8.2) becomes:

$$\begin{cases} M\dfrac{d^2x'}{dt^2}+\dfrac{dx'}{dt}+\langle u\rangle = k_1\sin\left(a\left(x'+X_0-\Omega_1't\right)\right)e^{-a\left(Y_0+y'\right)}+k_2\sin\left(2a\left(x'+X_0-\Omega_2't\right)\right)e^{-2a\left(Y_0+y'\right)} \\ M\dfrac{d^2y'}{dt^2}+\dfrac{dy'}{dt}+G = k_1\cos\left(a\left(x'+X_0-\Omega_1't\right)\right)e^{-a\left(Y_0+y'\right)}+k_2\cos\left(2a\left(x'+X_0-\Omega_2't\right)\right)e^{-2a\left(Y_0+y'\right)} \end{cases} \tag{8.5}$$

Using Euler's formula, the right hand of (8.5) in the form of complex exponential is:

$$\begin{cases} M\dfrac{d^2x'}{dt^2}+\dfrac{dx'}{dt}+\langle u\rangle = k_1e^{-aY_0}\,\mathrm{Re}\left[je^{-ay'+ja\left(\Omega_1't-x'-X_0\right)}\right]+k_2e^{-2aY_0}\,\mathrm{Re}\left[je^{-2ay'+j2a\left(\Omega_2't-x'-X_0\right)}\right] \\ M\dfrac{d^2y'}{dt^2}+\dfrac{dy'}{dt}+G = k_1e^{-aY_0}\,\mathrm{Re}\left[e^{-ay'+ja\left(\Omega_1't-x'-X_0\right)}\right]+k_2e^{-2aY_0}\,\mathrm{Re}\left[e^{-2ay'+j2a\left(\Omega_2't-x'-X_0\right)}\right] \end{cases} \tag{8.6}$$

Because $x'(t)$ and $y'(t)$ are small oscillations, the higher-order terms of their Taylor series expansion can be omitted:

$$\mathrm{Re}\left[e^{-ay'}e^{-jax'}\right]\cong\mathrm{Re}\left[1-a\left(y'+jx'\right)\right] \tag{8.7}$$

In addition, the average displacement of oscillation part $x'(t)$ and $y'(t)$ are zero, which should be the response of pure harmonic component. So the motion equation in the x direction can be separated into two equations:

$$\begin{cases} M\dfrac{d^2x'}{dt^2}+\dfrac{dx'}{dt}=k_1e^{-aY_0}\,\mathrm{Re}\left[je^{ja\left(\Omega_1't-X_0\right)}\right]+k_2e^{-2aY_0}\,\mathrm{Re}\left[je^{j2a\left(\Omega_2't-X_0\right)}\right] \\ \langle u\rangle = k_1e^{-aY_0}\,\mathrm{Re}\left[je^{ja\left(\Omega_1't-X_0\right)}a\left(-y'-jx'\right)\right]+k_2e^{-2aY_0}\,\mathrm{Re}\left[je^{j2a\left(\Omega_2't-X_0\right)}2a\left(-y'-jx'\right)\right] \end{cases} \tag{8.8}$$

Similarly, it gives

$$\begin{cases} M\dfrac{d^2y'}{dt^2}+\dfrac{dy'}{dt}=k_1e^{-aY_0}\,\mathrm{Re}\left[e^{ja\left(\Omega_1't-X_0\right)}\right]+k_2e^{-2aY_0}\,\mathrm{Re}\left[e^{j2a\left(\Omega_2't-X_0\right)}\right] \\ G = k_1e^{-aY_0}\,\mathrm{Re}\left[e^{ja\left(\Omega_1't-X_0\right)}a\left(-y'-jx'\right)\right]+k_2e^{-2aY_0}\,\mathrm{Re}\left[e^{j2a\left(\Omega_2't-X_0\right)}2a\left(-y'-jx'\right)\right] \end{cases} \tag{8.9}$$

Solving the first equation of (8.8) and (8.9):

$$\begin{cases} x'(t)=\mathrm{Re}\left[\dfrac{jk_1e^{-aY_0+ja\left(-x_0+\Omega_1't\right)}}{-a^2\Omega_1'^2M+ja\Omega_1'}\right]+\mathrm{Re}\left[\dfrac{jk_2e^{-2aY_0+j2a\left(-x_0+\Omega_2't\right)}}{-4a^2\Omega_2'^2M+j2a\Omega_2'}\right] \\ y'(t)=\mathrm{Re}\left[\dfrac{k_1e^{-aY_0+ja\left(-X_0+\Omega_1't\right)}}{-\Omega_1'^2M+j\Omega_1'}\right]+\mathrm{Re}\left[\dfrac{k_2e^{-2aY_0+j2a\left(-X_0+\Omega_2't\right)}}{-\Omega_2'^2M+j\Omega_2'}\right] \end{cases} \tag{8.10}$$

After getting $x'(t)$ and $y'(t)$, the second equation of (8.8) and (8.9) can be solved:

$$\langle u\rangle=\frac{e^{-2aY_0}k_1^{\,2}}{\Omega_1'\left(a^2\Omega_1'^2M^2+1\right)}+\frac{e^{-4aY_0}k_2^{\,2}}{\Omega_2'\left(4a^2\Omega_2'^2M^2+1\right)}+ ae^{-3aY_0}k_1k_2\left[\begin{array}{l}\dfrac{2a\Omega_2'M\sin\left(\left(2a\Omega_2'-a\Omega_1'\right)t-aX_0\right)+\cos\left(\left(2a\Omega_2'-a\Omega_1'\right)t-aX_0\right)}{2\Omega_2'\left(4a^2\Omega_2'^2M^2+1\right)}\\ +\dfrac{2a\Omega_1'M\sin\left(\left(a\Omega_1'-2a\Omega_2'\right)t-aX_0\right)+2\cos\left(\left(a\Omega_1'-2a\Omega_2'\right)t-aX_0\right)}{\Omega_1'\left(a^2\Omega_1'^2M^2+1\right)}\end{array}\right] \tag{8.11}$$

$$G=\frac{ae^{-2aY_0}k_1^{\,2}\Omega_1'M}{\Omega_1'\left(a^2\Omega_1'^2M^2+1\right)}+\frac{2ae^{-4aY_0}k_2^{\,2}\Omega_2'M}{\Omega_2'\left(4a^2\Omega_2'^2M^2+1\right)}+ ae^{-3aY_0}k_1k_2\left[\begin{array}{l}\dfrac{2\sin\left(\left(a\Omega_1'-2a\Omega_2'\right)t+aX_0\right)+2\Omega_1'M\cos\left(\left(a\Omega_1'-2a\Omega_2'\right)t+aX_0\right)}{\Omega_2'\left(\Omega_2'^2M^2+1\right)}+\\ \dfrac{\sin\left(\left(2a\Omega_2'-a\Omega_1'\right)t+aX_0\right)+\Omega_2'M\cos\left(\left(2a\Omega_2'-a\Omega_1'\right)t+aX_0\right)}{\Omega_1'\left(\Omega_1'^2M^2+1\right)}\end{array}\right] \tag{8.12}$$

In equation (8.11) and (8.12), the solutions of $\langle u\rangle$ and G are the combination of a constant and a harmonic component. The frequency of the harmonic components are the same: $a\Omega_1'-2a\Omega_2'=a\langle u\rangle$. Integrating both sides of the equation (8.13):

$$\int_0^{\frac{\lambda}{\langle u\rangle}}\langle u\rangle dt=\int_0^{\frac{\lambda}{\langle u\rangle}}\left\{\begin{array}{l}\dfrac{e^{-2aY_0}k_1^{\,2}}{\Omega_1'\left(a^2\Omega_1'^2M^2+1\right)}+\dfrac{e^{-4aY_0}k_2^{\,2}}{\Omega_2'\left(4a^2\Omega_2'^2M^2+1\right)}+\\ ae^{-3aY_0}k_1k_2\left[\begin{array}{l}\dfrac{2a\Omega_2'M\sin\left(\left(2a\Omega_2'-a\Omega_1'\right)t-aX_0\right)+\cos\left(\left(2a\Omega_2'-a\Omega_1'\right)t-aX_0\right)}{2\Omega_2'\left(4a^2\Omega_2'^2M^2+1\right)}\\ +\dfrac{2a\Omega_1'M\sin\left(\left(a\Omega_1'-2a\Omega_2'\right)t-aX_0\right)+2\cos\left(\left(a\Omega_1'-2a\Omega_2'\right)t-aX_0\right)}{\Omega_1'\left(a^2\Omega_1'^2M^2+1\right)}\end{array}\right]\end{array}\right\}dt \tag{8.13}$$

From that, directly follows:

$$\langle u\rangle=\frac{e^{-2aY_0}k_1^{\,2}}{\Omega_1'\left(a^2\Omega_1'^2M^2+1\right)}+\frac{e^{-4aY_0}k_2^{\,2}}{\Omega_2'\left(4a^2\Omega_2'^2M^2+1\right)} \tag{8.14}$$

Similarly:

$$G=\frac{ae^{-2aY_0}k_1^{\,2}M}{\left(a^2\Omega_1'^2M^2+1\right)}+\frac{2ae^{-4aY_0}k_2^{\,2}M}{\left(4a^2\Omega_2'^2M^2+1\right)} \tag{8.15}$$

Because the average velocity is very slow compared with wave velocity, we can assume:

$$\left(\frac{\Omega_1}{a}-\langle u\rangle\right)\approx\frac{\Omega_1}{a}\ ,\quad\left(\frac{\Omega_2}{2a}-\langle u\rangle\right)\approx\frac{\Omega_2}{2a} \tag{8.16}$$

Hence,

$$\langle u\rangle = \frac{ae^{-2aY_0}k_1^{\,2}}{\Omega_1\left(\Omega_1^{\,2}M^2+1\right)} + \frac{2ae^{-4aY_0}k_2^{\,2}}{\Omega_2\left(\Omega_2^{\,2}M^2+1\right)} = \frac{ae^{-2aY_0}\left(k_1^{\,2}-2k_2^{\,2}e^{-2aY_0}\right)}{\Omega_1\left(\Omega_1^{\,2}M^2+1\right)} \tag{8.17}$$

$$G = \frac{ae^{-2aY_0}k_1^{\,2}M}{\left(\Omega_1^{\,2}M^2+1\right)} + \frac{2ae^{-4aY_0}k_2^{\,2}M}{\left(\Omega_2^{\,2}M^2+1\right)} = \frac{ae^{-2aY_0}M\left(k_1^{\,2}+2k_2^{\,2}e^{-2aY_0}\right)}{\left(\Omega_1^{\,2}M^2+1\right)} \tag{8.18}$$

Set:

$$H = \frac{G\left(\Omega_1^{\,2}M^2+1\right)}{aM} \tag{8.19}$$

The average levitation height and velocity can be obtained:

$$Y_0 = -\frac{1}{2a}\ln\left(\frac{-k_1^{\,2}+\sqrt{k_1^{\,4}+8Hk_2^{\,2}}}{4k_2^{\,2}}\right) \tag{8.20}$$

$$\langle u\rangle = \frac{a\left(-k_1^{\,2}+\sqrt{k_1^{\,4}+8Hk_2^{\,2}}\right)\left(3k_1^{\,2}-\sqrt{k_1^{\,4}+8Hk_2^{\,2}}\right)}{8k_2^{\,2}\Omega_1\left(\Omega_1^{\,2}M^2+1\right)} \tag{8.21}$$

B: Code for Boundary Element Methods

The code for the analysis of the electric field of a parallel electrode array using the BEM is uploaded to the Notebook Archive in Wolfram Notebook, which is not only be immediately visible but also evaluable in the Wolfram Cloud. The link is:

https://notebookarchive.org/2022-12-3piktmq.

C: Supplements for Experiment

C.1 PCBWAY Company

PCBWAY Company is a specialized PCB manufacture and has factories in Shenzhen. The one-stop online self quote-order system can be accessed from https://www.pcbway.com/.

C.2 Ballotini and PMMA Particle

The details of the Ballotini product can be found here:

https://www.sili.eu/en/products/glass-beads/micro-glass-beads-silibeads-solid/

The main of PMMA properties is shown in the below Table 8-1. More detail can be found at:

https://microspheres.us/technical-characteristics-pmma-microspheres/

Table 8-1 Technical Properties of PMMA Microspheres

Density (g/cm^3)	1.19
Water absorption – over 24 hours (%)	0.2
Dielectric constant @1MHz	2.6
Surface resistivity (Ω /sq)	10^{14}
Volume resistivity (Ω·cm)	2 to14 ×10^{15}

C.3 Verification of Function of Power Supply System

The waveform, amplitude, frequency and phase difference of the output of the function generator were confirmed, which is shown in Fig. 8.1.

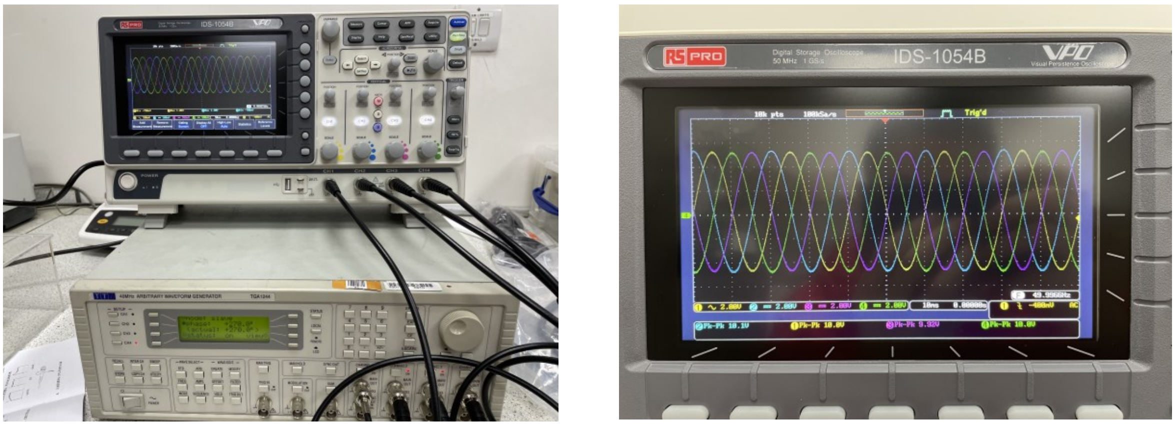

(*a*) connection of the four output of function generator to an oscilloscope

(b) information of the four output wave, including wave form, amplitude, frequency and phase difference

Fig. 8.1 Function verification of function generator and demonstration of the details of waves.

The measurement and test of the sinusoidal wave output of high voltage is shown in Fig. 8.2, which confirms the accuracy of the high voltage output.

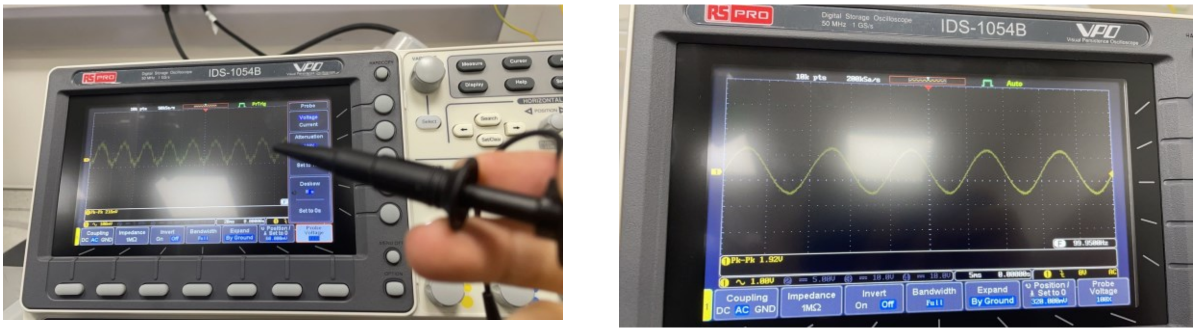

(*a*) The use of high voltage probe

(b) The measurement of sinusoidal wave output

Fig. 8.2 Accuracy verification of high voltage amplifier.

C.4 Experiment Procedure

The preparation of experiment procedures are listed as follows:

1. Prepare all samples to be transported in advance; note starting weights, size fraction and sample type.
2. Note the ambient temperature.
3. Place amplifier and function generator in the table of experimental area stably.
4. Connect the safety ground of amplifier to the grounding point of the setup.
5. Connect the output of amplifier with the connecting pin of PCB and check if the connection is tight and safe. Notice: output connectors may only be touched when the device is disconnected from the power supply!
6. Connect the function generator and amplifier using BNC and check if the connection is proper.
7. Connect the power leads of function generator and amplifier to the power source.
8. Check all the connections again and make sure they are connected safely.

The basic running of the experiment procedures are as follows:

1. Put sample on the PCB and cover the lid of the box.
2. Set the parameters of the function generator.
3. Turn on the power of function generator.
4. Turn on the power of amplifier.
5. Once the particles have been transported into collection box, turn off the power of amplifier.
6. Turn off the power of function generator.
7. Grounding the PCB.
8. Collect the particles and reset the experiment.

C.5 Track Software Operational Manual

The particle in the frames can be identified based on the pixel features of each point and its surroundings automatically. If the image is not clear, the point can also be manually identified. The marked positions are recorded on each frames, shown as purple circles in Fig. 8.3, and therefore, the variation of position with time is obtained. The result was recorded in the sheets shown in the right columns of Fig. 8.3.

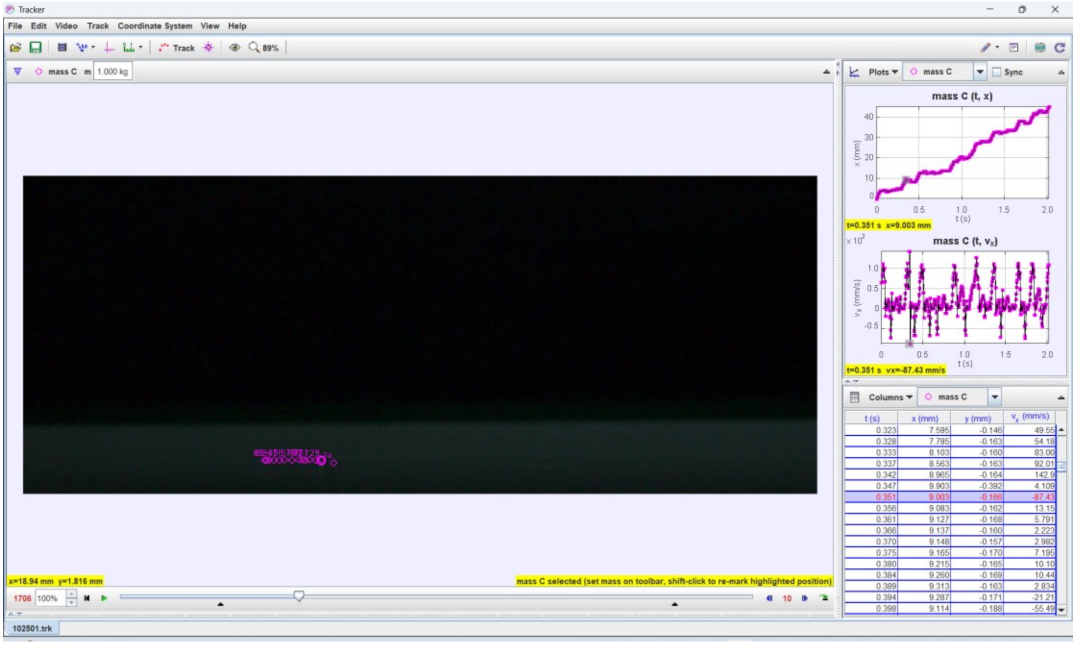

t=0.351 s x=9.003 mm

t=0.351 s vx=-87.43 mm/s

x=18.94 mm y=1.816 mm

mass C selected (set mass on toolbar, shift-click to re-mark highlighted position)

t (s)	x (mm)	y (mm)	v_x (mm/s)
0.323	7.595	-0.146	49.55
0.328	7.785	-0.163	54.18
0.333	8.103	-0.160	83.00
0.337	8.563	-0.163	92.01
0.342	8.965	-0.164	142.9
0.347	9.903	-0.392	4.109
0.351	9.003	-0.166	-87.43
0.356	9.083	-0.162	13.15
0.361	9.127	-0.168	5.791
0.366	9.137	-0.160	2.223
0.370	9.148	-0.157	2.982
0.375	9.165	-0.170	7.195
0.380	9.215	-0.165	10.10
0.384	9.260	-0.169	10.44
0.389	9.313	-0.163	2.834
0.394	9.287	-0.171	-21.21
0.398	9.114	-0.188	-55.49

Fig. 8.3 Software User Interface: the top row is the software's functionality area to open and save file. The second top row involves the scale calibration and particle tracking function.